Aus dem Institut für Radiologie und Nuklearmedizin
der Medizinischen Fakultät Charité – Universitätsmedizin Berlin

DISSERTATION

Metal-based Contrast Agents for Magnetic Resonance Imaging: Distribution in Atherosclerotic Plaques Analyzed by Elemental Microscopy

Metallbasierte Kontrastmittel für die Magnetresonanztomographie: Untersuchungen zur deren Verteilung in atherosklerotischen Plaques mittels Elementmikroskopie

zur Erlangung des akademischen Grades
Doctor of Philosophy (PhD)

vorgelegt der Medizinischen Fakultät
Charité – Universitätsmedizin Berlin

von

Yavuz Oguz Uca
aus Istanbul, Türkei

Datum der Promotion: 25.11.2022

Inhaltsverzeichnis (Table of Contents)

1. List of Abbreviations

AHA	American Health Association
Anti-RAM-11	Anti-Rabbit Macrophage
Anti-SMA	Anti-Smooth Muscle Actin
ATP	Adenosine Triphosphate
Ca	Calcium
CA	Contrast Agent
CAM	Cell Adhesion Molecule
CCS	Color-Coded Sonography
CPS	Counts per Second
CS	Chondroitin Sulfate
CT	Computed Tomography
CTA	Computed Tomography Angiography
CVD	Cardiovascular Disease
BLISS	Beamline Instrumentation Software Support
DS	Dermatan Sulfate
EC	Endothelial Cell
ESRF	European Synchrotron Radiation Facility
Eu	Europium
Fe	Iron
g	Gram
GAG	Glycosaminoglycan
GBCA	Gadolinium-based Contrast Agent
Gd	Gadolinium
Gd-BOPTA	Gadobenate Dimeglumine
GF	Growth Factor
HA	Hyaluronic Acid (hyaluronan)
HS	Heparan Sulfate
IHC	Immunohistochemistry
IL	Interleukin
IONP	Iron Oxide Nanoparticle
IV	Intravenous
IVUS	Intravascular Ultrasound
keV	Kilo-Electron Volts

kg	Kilogram
KM	Kontrastmitteln
LAGeSo	Landesamt für Gesundheit und Soziales
LA-ICP-MS	Laser Ablation Inductively Coupled Mass Spectrometry
LDL	Low Density Lipoprotein
LGE	Late Gadolinium Enhancement
LOD	Limit of Detection
LP	Lipoprotein
M	Molar
mA	Milliampere
MMP	Matrix Metalloproteinase
MR	Magnetic Resonance
MRA	Magnetic Resonance Angiography
MRI	Magnetic Resonance Imaging
ms	milliseconds
µM	Micromolar
µm	Micrometer
NIRF	Near Infra-Red Fluorescence
NIRS	Near Infra-Red Spectroscopy
nm	Nanometer
nmol	nanomol
NSF	Nephrogenic Systemic Fibrosis
NZW	New Zealand White
OCT	Optical Coherence Tomography
P	Phosphorus
PAMP	Pathogen-Associated Molecular Pattern
PET	Positron Emission Tomography
PG	Proteoglycan
PyMCA	Python Multichannel Analyzer
RGB	Red Green Blue
ROI	Region of Interest
ROS	Reactive Oxygen Species
S	Sulfur
SMC	Smooth Muscle Cell

SPECT	Single-Photon Emission Tomography
SR-µXRF	Synchrotron Radiation micro X-Ray Fluorescence
VCAM	Vascular Cell Adhesion Molecule
VH-IVUS	Virtual Histology Intravascular Ultrasound
VSOP	Very Small Superparamagnetic Iron Oxide Nanoparticle
ZeBanC	Zentrale Biomaterialbank der Charité

2. Abstrakt

2.1. Abstrakt (Deutsch)

Ziel: Die Möglichkeiten einer Charakterisierung atherosklerotischer Plaques mittels Magnetresonanztomographie (MRT) unter Einsatz von i.v. applizierten unspezifischen Eisenoxid-Nanopartikel (IONP)-basierten und Gadolinium (Gd)-haltigen Kontrastmitteln (KM) sind Gegenstand der Forschung. Um ein besseres Verständnis zu erhalten, welche pathologischen Veränderungen in der Gefäßwand durch die KM markiert werden, wurde in der vorliegenden experimentellen Arbeit für je einen Vertreter dieser beiden KM-Typen die Mikroverteilung in atherosklerotischen Plaques an histologischen Präparaten mittels Elementmikroskopie untersucht.

Methoden: Die vorliegende Arbeit wurde als Post-hoc-Analyse von archivierten Gewebeproben durchgeführt, die im Rahmen einer früheren In-vivo-MRT-Studie an einem Kaninchenmodell der Atherosklerose zur Untersuchung der Signaländerungen in der Gefäßwand nach i.v. Injektion sehr kleiner IONP (VSOP) und Gd-BOPTA gewonnen wurden. Zur Unterscheidung von endogenem Fe wurde Europium-dotiertes VSOP (Eu-VSOP) verwendet. Serienschnitte (5 µm) von Formalin-fixierten Gefäßwandpräparaten wurden mittels IHC (Movat-Pentachrom, von Kossa und Alcian), IHC (anti-smooth muscle cell actin (Anti-SMA) und Anti-Kaninchen-Makrophagen (Anti-RAM 11)) gefärbt und mittels Elementmikroskopie (Laserablation mit induktiv gekoppelter Plasma-Massenspektrometrie (LA-ICP-MS) und Synchrotronstrahlungs-basierter Mikro-Röntgen-Fluoreszenz (SR-µXRF) Spektroskopie untersucht und hieraus Elementverteilungskarten von Fe, Eu, Gd, Schwefel (S), Phosphor (P) und Calcium (Ca) erzeugt. HC, IHC und Elementverteilungen wurden verglichen.

Ergebnisse: Mittels IHC konnte die Pathomorphologie atherosklerotischer Plaques charakterisiert werden. Die Elementarmikroskopie zeigte, dass die S-Verteilung dem anatomischen Aufbau der arteriellen Gefäßwandschichten folgt, während die P-Verteilung zellreiche Areale anzeigt. LA-ICP-MS hatte eine Nachweisgrenze von ~ 0,1 nmol/g für Gd sowie von ~ 100 nmol/g für Fe. Das Eu-positive Signal identifizierte das Vorhandensein von VSOP in der Gefäßwand und ermöglichte die Abgrenzung von Eu-VSOP gegenüber der Verteilung von endogenem Fe. ECM-Material korrelierte mit dem Eu-Signal, der Fe-Konzentration und der maximalen Gd-Konzentration. Eu-VSOP war in frühen Läsionen auf das Endothel beschränkt, während es in fortgeschrittenen Plaques mit zellreichen Arealen

korrelierte. Die Gd-Verteilung war in gesunden Arterien homogen, in frühen und fortgeschrittenen Plaques jedoch inhomogen. SR-μXRF-Scans mit einer Auflösung von 0,5 μm zeigten Gd-Hotspots mit zusätzlich erhöhten P- und Ca-Konzentrationen am intimomedialen Übergang und Durchmessern im Bereich von einigen Mikrometern bis zu Submikrometern.

Schlussfolgerungen: Eu-VSOP und Gd weisen unterschiedliche räumliche Verteilungen in atherosklerotischen Plaques auf. Während die Verteilung von Eu-VSOP stärker zellassoziiert ist und zur Überwachung des Fortschreitens von atherosklerotischen Plaques verwendet werden kann, weist die Gd-Verteilung auf eine arterielle Verkalkung hin und kann bei der Charakterisierung der Plaque-Vulnerabilität hilfreich sein.

2.2. Abstract (English)

Purpose: The value of contrast-enhanced magnetic resonance imaging (MRI) with IV administration of nonspecific contrast agents (CAs) based on iron oxide nanoparticles (IONPs) and gadolinium (Gd) is currently being investigated in characterizing atherosclerotic plaques.. In this experimental dissertation study, we investigated the microdistribution of one CA representative of each of these two CA types in atherosclerotic plaques by elemental microscopy of histological sections in order to further better-understand which pathologies of the arterial wall are targeted by these CAs.

Methods: This dissertation study was performed on archived tissue specimens from a previous MRI study, which examined MRI signal changes in the vessel wall induced by very small IONPs (VSOPs) and Gd-BOPTA following IV injection in a rabbit model. Analytical discrimination of VSOPs from endogenous Fe was achieved by europium (Eu) doping of the particles, resulting in Eu-VSOPs. 5 μm serial sections of formalin-fixed arterial specimens were subjected to immunohistochemistry (IHC; Movat's pentachrome, von Kossa, Alcian blue, anti-smooth muscle cell actin (anti-SMA), and anti-rabbit macrophage (anti-RAM-11)), and elemental microscopy with laser ablation inductively coupled plasma mass spectrometry (LA-ICP-MS) and synchrotron radiation μX-ray fluorescence (SR-μXRF) spectroscopy. Elemental distribution maps of Fe, Eu, Gd, sulfur (S), phosphorus (P) and calcium (Ca) were analyzed.

Results: IHC revealed pathomorphology of the atherosclerotic plaques. S distribution matched the anatomy of arterial vessel wall layers, and P distribution revealed cellular areas. LA-ICP-MS detected Gd and Fe with a limit of detection of ~0.1 nmol/g and ~100 nmol/g, respectively. VSOPs were identified through Eu-positive signal, which also differentiated Eu-VSOP distribution from that of endogenous Fe. ECM material correlated with Eu signal intensity, Fe concentration, and maximum Gd concentration. In early lesions, Eu-VSOPs were confined to endothelium, whereas they accumulated in cellular areas in advanced plaques. Gd distribution was homogeneous in healthy arteries and inhomogeneous in early and advanced plaques. SR-μXRF revealed Gd hotspots with increased P and Ca concentrations majorly at the intimomedial interface and diameters ranging from a few micrometers to submicrometers.

Conclusions: Spatial distributions Eu-VSOPs and Gd in atherosclerotic plaques are different. Eu-VSOP distribution is more cell-associated, suggesting their use in monitoring atherosclerotic plaque progression. Gd distribution indicates arterial calcification, which might help in characterizing plaque vulnerability.

3. Manteltext

3.1. Introduction

Parts of the text passages presented in this publication-based dissertation study, mainly in the Abstract, the Materials and Methods and in the Results sections, are similar to the corresponding text passages in my original publication. Complete citation list, original publication, 'Declaration of Own Contribution to the Top-Journal Publication' with the detailed description of own contribution and proof of top-journal list are provided within following sections.

Cardiovascular disease (CVD) including ischemic heart disease, arterial disease, myocardial or cerebral infarction, stroke, heart failure and sudden cardiac death has emerged as a predominant healthcare concern [1, 2]. With growing cases of obesity, diabetes, hypercholesterolemia or metabolic syndromes in addition to the risk factors such as genetic background, age, sex, lack of exercise or smoking, CVD also holds an economic burden accounting for 17% of national health expenditures in the US in 2011 [3]. Less than a decade later, in 2017, CVD was found responsible for 17.8 million deaths worldwide with invaluable loss of lives and productivity, and other massive economic burden arising from disability [4]. Unless risk factor stratification and prevention are improved with the guidance of advanced prediction models, sizable increase in the CVD incidence is forecasted over the next decades especially in aging western populations [4,5]. An important body of evidence derived from post-mortem investigations and epidemiological studies has identified atherosclerosis as the underlying cause, based on which investigators propose three central goals of research: early detection of atherosclerotic plaque development, elucidation of underlying mechanisms of plaque progression, and discrimination of stable and vulnerable plaques [6,7].

Intact arterial structure is a poroelastic, shear-flow modulated environment with vascular endothelium playing a pivotal role in vasodilation and inhibition of rolling and tethering of circulating monocytes or platelets [8]. Among the theories on the origin of atherogenesis, response to injury was proposed by Ross and Glomset, which declares that injury to the endothelium is the foremost initiating event that primarily takes place by the accumulation of low-density lipoproteins (LDLs) on the endothelial lineage [9, 10]. This alters blood flow, increases turbulence, and creates early signs of vessel wall inflammation (Fig. 1a) [10, 11]. Another theory calls biologically active lipids as the initiators rather than the accumulation of the LDLs on the endothelial lineage [12]. Oxidative stress theory proposes that oxidative

modifications on the LDLs are induced by small lipoperoxide transfer seeding onto the LDL core by reactive oxygen species (ROS) released from natural cellular activities such as proliferation of smooth muscle cells (SMCs) and activated monocytes [13, 14]. These biologically active lipids participate in further lipid peroxidation, activation of the cell surface receptors on the endothelium and leukocyte recruitment subsequently affecting downstream signaling cascades causing inflammation in the vessel wall [14]. Lipoproteins (LPs) that are bound to other components within the tissue extracellular matrix (ECM) such as proteoglycans (PGs) and glycosaminoglycans (GAGs) are known to be more sensitive to such modifications and enzymatic hydrolysis that increase atherogenicity [15].

Currently, atherosclerosis is accepted as a spatially and temporally heterogeneous process with an interplay of complicated pathological and molecular mechanisms taking place upon interactions of atherogenic entities on the endothelium, and subentothelial retention of such molecules by the ECM molecules (Fig. 1) [16, 17]. Known as the response-to-retention theory, low-grade inflammation within the vessel wall activates endothelial cells (ECs), vascular SMCs, monocytes, macrophages, T-cells, B-cells, dendritic cells and fibroblasts in the subendothelial space [18]. Cell adhesion molecules (CAMs) on the endothelium interact with circulating blood leukocytes, enabling them to extravasate into the subendothelial space, and differentiate into mature macrophages, which than engulf lipids and give rise to foam cells (Fig. 1a) [19]. Immune activities release cytokines, also known as interleukins (ILs), growth factors (GFs) and of ROS, subsequently leading to subendothelial retention and modifications of the LPs, eventually resulting in endothelial dysfunction [20-21].

Lesion formation in atherosclerosis may persist with growing lesion size and inflammatory pathology if unabated. Meanwhile, outward arterial remodeling compensates for compromised blood flow and partially relieves ischemia through formation of neovessels originating from the vasa vasorum and extending into the intima (Fig. 1b, 1c) [22]. Medial SMCs undergo phenotypic change from the contractile to the synthetic phenotype and migrate into intimal regions, where they synthesize extracellular matrix (ECM) that enriched in proteoglycans (PG) and glycosaminoglycans (GAG) to cover enlarging foam cells. Similar to scar formation, this activity gives rise to a thick collagenous fibrous cap (Fig. 1b) [23]. The most important determinant of acute symptoms result from erosion or uneven thinning of the fibrous cap by

matrix metalloproteinase (MMP) activity, which degrades the ECM and leads to fissure formation or plaque rupture (Fig. 1c) [7].

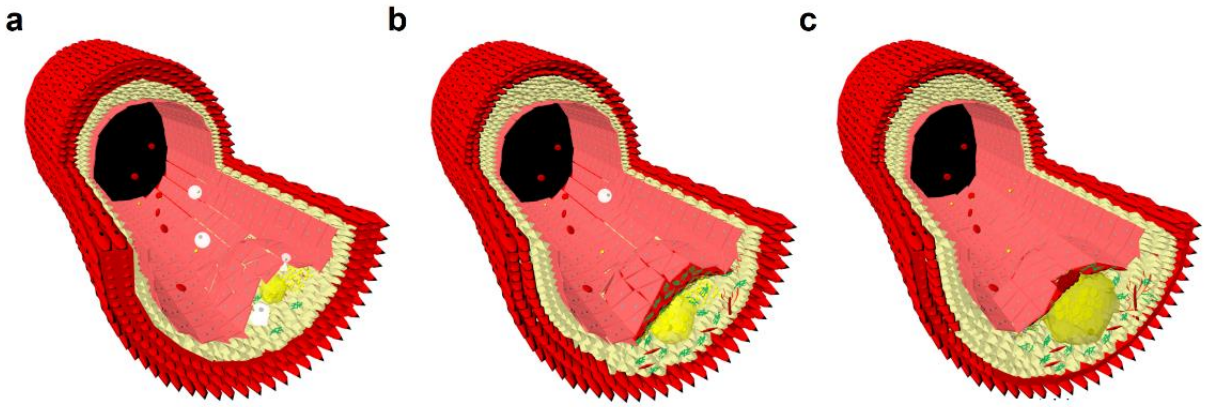

Figure 1: Schematic illustration of atherosclerotic plaque progression. **a** Intact arterial structure allows vasodilation and prevents rolling and tethering of blood components. Atherosclerosis is initiated by accumulation of low-density lipoproteins (LDLs) on the endothelium. Blood leukocytes extravasate into the subendothelial space, and differentiate into mature macrophages, thereby giving rise to foam cells. **b** Medial SMCs undergo phenotypic changes and migrate into the growing intima, where they synthesize extracellular matrix (ECM) as part of outward remodeling. This gives rise to a thick collagenous fibrous cap [23]. **C** Matrix metalloproteinase (MMP) activity degrades the ECM that results in thinning of the fibrous cap, subsequently leading to fissure formation or plaque rupture. Adapted with permission from [24].

In clinical practice, atherosclerosis is typically diagnosed by catheter-based X-ray angiography, a luminographic procedure that detects arterial stenosis or occlusion but cannot reliably discriminate between stable and vulnerable plaque. X-ray angiography and other imaging modalities including color-coded sonography (CCS), computed tomography angiography (CTA), and magnetic resonance angiography (MRA) can be used to evaluate compromised blood flow and grade luminal narrowing morphologically [25]. However, these methods have limitations because they may only show non-significant arterial narrowing resulting in failed detection of especially earlier stages of the plaque formation due to expansive remodeling [26]. Because of such diagnostic limitations, sudden clinical events are often observed in patients with angiographically mild luminal narrowing and are due to thrombotic occlusion related to plaque fissures or erosions. Further developments of diagnostic tests focus on detecting mechanisms of inflammation, in which molecular imaging has emerged as a promising approach [27].

Currently, various imaging modalities are being reviewed for their value in vulnerable plaque characterization [28-32]. Catheter-based approaches involving near infrared fluorescence / spectroscopy (NIRF/NIRS), optical coherence tomography (OCT) or intravascular ultrasound (IVUS), despite their strength such as real-time imaging, high spatial resolution and multimodal capabilities, are disadvantageous due to their invasive nature or operator dependency [28, 29]. CT is promising in imaging coronary plaque calcification and predicting major cardiovascular events. Its advantages include short acquisition time, anatomical imaging capability, high penetration depth and resolution, while it gives out poor soft tissue contrast and involves radiation [30]. Radionuclide imaging approaches including positron emission tomography (PET) and single-photon emission tomography (SPECT) have excellent intrinsic sensitivity with unlimited penetration depth, and yield cellular or molecular information, e.g. glucose metabolism, MMP activity or apoptosis [31, 32]. However, the requirement of cyclotrons for the generation of imaging tracers, low spatial resolution, and radioactivity are major drawbacks of radionuclide-based imaging approaches.

The ideal method for clinical imaging of atherosclerosis is noninvasive and combines angiographic examination and assessment of pathological changes on the plaque composition with quantitative analysis and predictive value at the molecular level. The major pathological processes of atherosclerotic plaque progression are: lipid accumulation, fibrous cap formation and thinning, ECM accumulation and degradation, apoptosis and vascular calcification, erosion, intraplaque hemorrhage and thrombosis [33]. MRI has the distinguished feature of providing unique soft tissue contrast with submillimeter spatial resolution, and its sensitivity is improved by contrast agent (CA) administration that allows anatomic and physiologic examination [34]. Following intravenous (IV) injection of metal-based CA, either paramagnetic gadolinium (Gd)-based chelates (GBCAs) in the clinical setting or superparamagnetic iron oxide nanoparticles (IONPs) in experimental studies, dynamic MRI allows quantitative characterization of arterial stenosis as well as identification of features associated with plaque progression [35].

MRI depends on longitudinal (T1) and transverse (T2) relaxation times of bulk water protons, which create contrast in biological tissues by alterations upon interactions of CAs with tissue composition. Shortening of the T1 relaxation time of a tissue results in positive contrast in T1-weighted images, while shortening of T2 (T2*) relaxation time results in negative contrast in T2- (T2*-) weighted images [34]. GBCAs are T1 imaging agents known to distribute within

the intravascular and extravascular/extracellular space nonspecifically after IV administration and to be cleared via rapid renal excretion [36]. GBCAs predominantly shorten T1 relaxation times of neoplastic lesions with increased perfusion, vascularity or vascular permeability. Sensitivity of GBCAs has been improved in order to detect molecular targets during atherosclerotic plaque progression, which subsequently resulted in the development of targeted GBCAs at specific plaque components such as fibrin or elastin [37–39]. Importantly, in a recent study that serves as the basis to this dissertation research work, we investigated correlations between vessel wall late gadolinium enhancement (LGE) in T1-weighted MRI and histologic markers of atherosclerotic plaque progression over a time course of 60 min [40]. We observed a steady increase from moderate to strong correlation with ECM material or calcifications, and low correlation with macrophages (Fig. 2).

Tissue deposition of Gd is a well-known phenomenon in patients who are administered GBCAs in their MRI examinations. Gd tissue deposition has been linked to nephrogenic systemic fibrosis (NSF), and studies have reported biodistribution of Gd around vascularized areas of skin, kidney, liver and brain after IV administration [41-43]. Observations of non-uniformly distributing insoluble Gd colocalizing with phosphorus (P) and calcium (Ca) indicate Gd dissociation and transchelation by physiological anions that can possible result in reactive immune cell response [44-48]. Gd deposition in the heart and aorta has also been published, while quantitative data on Gd deposition in atherosclerotic plaques are still lacking [49].

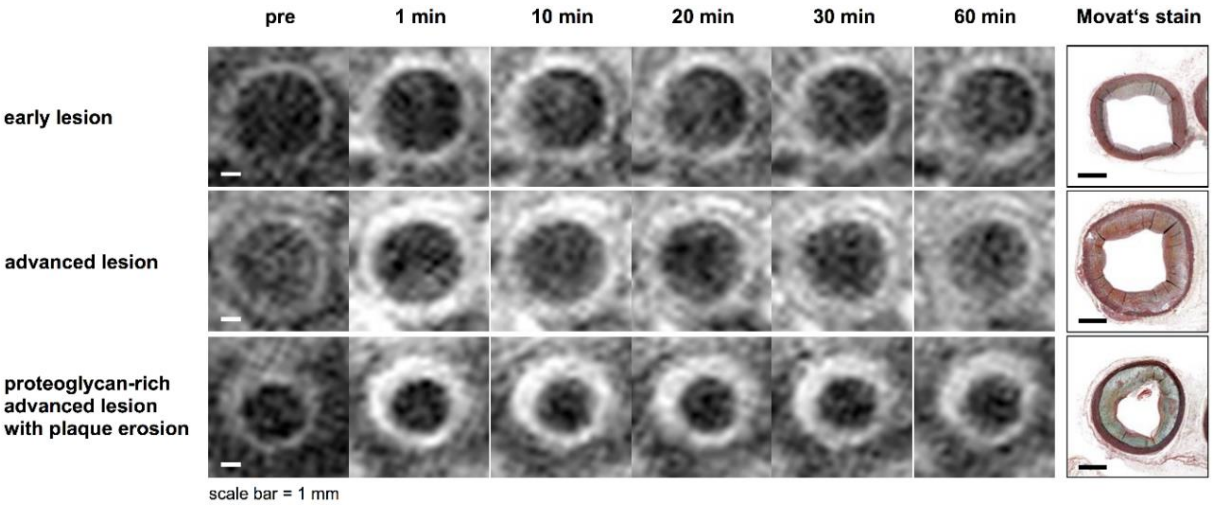

Figure 2: Late gadolinium (Gd) enhancement (LGE) in arterial vessel wall (T1-weighted MRI) and correlation with ECM material over time. There is a steady increase from moderate to strong correlation with proteoglycan (PG)- and glycosaminoglycan (GAG)-rich ECM material or calcifications. Correlation is lowest with macrophages and remains stable over a time course of 60 min. Adapted with permission from [40].

IONPs are known T2 imaging probes with a pronounced T2-shortening effect in areas of focal accumulation of these probes [49]. IONPs are cleared by the reticuloendothelial system after IV application, a mechanism which has been extensively studied as a promising imaging strategy as these nanoparticles are concentrated in macrophages upon phagocyctosis that results in decreased signal intensity [50, 51]. IONPs can also be conjugated to peptides or antibodies, examples of which are frequently used to visualize endothelial dysfunction, proteolysis or apoptosis. Well-known molecular targets include CAMs such as αvβ3-integrin or vascular adhesion molecule-1 (VCAM-1), annexin-V, and MMP-2 or MMP-9 [52–57]. Majority of studies investigating IONPs reported intraplaque distribution of nanoparticles 24 h after IV injection, and typically applied polymer-coated IONPs. Importantly, the use of citrate-coated very small superparamagnetic iron oxide nanoparticles (VSOPs) with a hydrodynamic size of 7 nm, faster vascular distribution and longer blood half-life displayed earlier plaque uptake (<2 h) that correlated with the accumulation of ECM material [58, 59]. IONPs have also been used for imaging atherosclerotic plaque inflammation in humans in clinical trials, not only to assess the progression but also patient selection with high risk [50].

Until the last years, studies utilizing contrast-enhanced MRI for imaging atherosclerotic plaque progression had focused on the cellular mediators of the inflammation, thus leaving ECM mostly ignored. However, in the last years, MR imaging of the ECM has been attracting attention, primarily because ECM is the most abundant component of the vascular ultrastructure, the coordinate synthesis and turnover of the ECM are fundamental features of plaque instability, and the biologically active nature of the ECM highlights potential novel probe-target interactions [60, 61]. In other words, alterations in the ECM composition offer a large pool of molecules, functions or relative distributions of which might grant crucial information for the characterization and monitoring.

ECM is a highly organized and complex biochemical meshwork of intervened structural composition in biological tissues with intrinsic poroelactic interactions and electroviscous effects (Fig. 3) [62]. Mainly two different units of structural entities form its composition: fibril-forming molecules and non-fibril forming molecules. These molecules are collagen, elastin and fibrin, comprising fibril-forming units, and PGs and GAGs comprising non-fibril forming units. There are also other types of interfibrillar molecules such as laminin, tenascin and fibronectin, which play valuable roles in supporting the interactions between structural ECM molecules by assisting contact formations, and bridging the ECM to the cells and to other

forms of soluble molecules such as GFs, cytokines and signalling molecules within the ECM [63-65]. Collagen, elastin and fibrin are the major entities, which provide tensile strength and elasticity to the arterial tissue, whereas PGs and GAGs are known to serve as gel-like ground filling medium with significant viscoelastic properties as well as regulatory units that govern intermolecular communication within the arterial tissue composition [61, 64].

Collagen is the most abundant fibrillar protein family in the ECM with nearly 30 different types and more than 40 different genetically variable subtypes with distinct polypeptide chains (Fig. 3) [66]. In the arterial ECM, collagen type I, III, IV, V, VI and VIII are known to be expressed with collagen type I being the most dominant among others [61, 67]. Structurally, collagen is a triple helix composed of 3 α-polypeptide chains, forming the basic motif, also known as procollagen, which can subsequently form higher complexity of fibrillary networks in the form of homodimers or heterodimers [66]. Expression, aggregation or degradation of collagen are key characteristic events during atherosclerotic plaque progression. Collagen accumulation peaks during the transformation of early stage atherosclerotic plaque formation, in which the ECM is a still a provisional loose matrix, composition of which is similar to wound healing, which mainly consists of gel-like ground filling non-fibril forming molecules [24]. In the fibrous plaque, collagen comprises majority of the ECM composition, because of which collagenous plaque is accepted to be the stable form as collagen provides the arterial tissue with the tensile strength, granting the ability to stretch despite that the lumen becomes more occluded due to enlarging intima. In fact, another pathological process of atherosclerotic plaque progression, typically known as thinning of the fibrous cap, refers to degradation of strong collagen fibril network by the enzymatic activities of the MMPs increased due to persisting inflammation [68].

Elastin is another component of the fibrillary network in humans, primarily found in the ECM of the arterial tissues, lungs and skin (Fig. 3). Notably, elastin forms an important fraction of the dry weight (more than 50%) in the large arteries [69]. In healthy arteries, it is mainly found in the medial layers of the arterial wall, expressed as the precursor tropoelastin molecules by the SMCs, which subsequently becomes mature elastin by cross-linkages, thus supporting the physical integrity, sustaining mechanical stress and vascular pressure [64]. During the course of atherosclerotic plaque progression, elastin prevents LDL infiltration by forming elastic lamellas in the growing neointima, however, similar to collagen, it is gradually degraded by the MMP-activity in advancing plaques [24, 70].

The last component of the fibrillary network is fibrin, which is originally not a major part of healthy arteries, but becomes increasingly expressed in the course of atherosclerotic plaque progression. This is mainly due to persisting inflammatory activities, which enhance endothelial permeability with the influx of blood-derived components causing the collagen-rich stable plaque to become unstable [71]. At this stage, degradation of the ECM composition might lead to tear or rupture formations within the enlarging plaque, activities that involve fibrin-associated coagulation cascades that eventually form thrombi [61]. Coagulant activity of fibrin and its modular interactions make it a useful target for the characterization of the high-risk atherosclerotic plaques with subacute and acute indications [72, 73].

As the non-fibril forming entities of the ECM, GAGs were historically only accepted for their space filling properties that was thought to be necessary for the organization and orientation of the ECM, however, currently**,** they are considered as key players in the regulatory network of the cell [74]. Their active involvements in governing the cellular communication have been acknowledged since their functional characteristics have been characterized through studies on their PG components [75-81]. GAGs constitute sugar-based elements of the ECM that are composed of dissacharides mostly covalently attached to a protein core, synthesis of which are regulated transcriptionally and post transcriptionally (Fig. 3) [24]. GAGs are distributed among different tissues or within a tissue highly heterogeneously, where they also are involved in diverse functions, all owing to their combinatorial biosynthesis that maximizes the amount of information that carry, thus resulting in their ability to participate in enriched types of interactions [77, 82]. Hyaluronic acid, also known as hyaluronan (HA), heparin, heparan sulfate (HS), chondroitin sulfate (CS) and dermatan sulfate (DS) are the major types of GAGs, all of which can be found in the arterial tissue composition with different distribution patterns. GAG types, distributions and proportions vary greatly during atherosclerotic plaque formation and progression. In genenal, immunohistochemical studies revealed their low presence in the healthy arterial wall but upregulation during progression with a general increase in the CS/DS content, and decrease in the HS content [83-85]. Owing to their highly negatively charged nature that brings about their ability to form electrostatic bridges between nearby molecules, GAGs are the basic components of dynamic supramolecular organization of the ECM, where they assist or regulate interactions with fibril-forming components such as collagen, fibrin or laminin by contributing to the tertiary complex formations and creating hydrated viscoelastic environments [63, 71]. They initiate and control signaling cascades, which become more prominent under inflammatory pathological conditions, during which they guide chemokines

to the cell surface, support cell migration and proliferation or retention of inflammatory elements or cells or pathogen-associated molecular patterns (PAMPs) [71, 81, 86]. In early atherogenesis, endothelial activation, thereby permeability of the basement membrane is altered through actions of integrins by EC-bound chemokines, leading to transmigration of blood monocytes. HA, DS and HS have been suggested to take roles in this process [87].

Contrast-enhanced MRI with the use of GBCAs at the clinical level and IONPs in experimental studies have helped understand atherosclerotic plaque progression, though the focus has been more on the cellular mediators of the inflammation, thus leaving ECM ignored, which has only recently started to attract more attention in scientific research [61]. It is highly reasonable that metal-based CAs might disseminate within atherosclerotic plaques through mechanisms involving metal dissociation and complexation upon interactions with endogenous molecules and anionic components of the plaque ECM. Distributions of metals and non-metals as well as trace elements in biological tissues, cells, subcellular compartments, even in single organelles are key determinants of physiological interactions. Changes in single elemental concentrations can alter downstream signalling cascades, which may result in changes in gene and protein expression [88]. Moreover, molecular interactions between the ECM components are highly abundant during arterial remodelling, which might be useful in discriminating the mechanisms responsible for the transition of stable to vulnerable plaques (Fig. 3) [24].

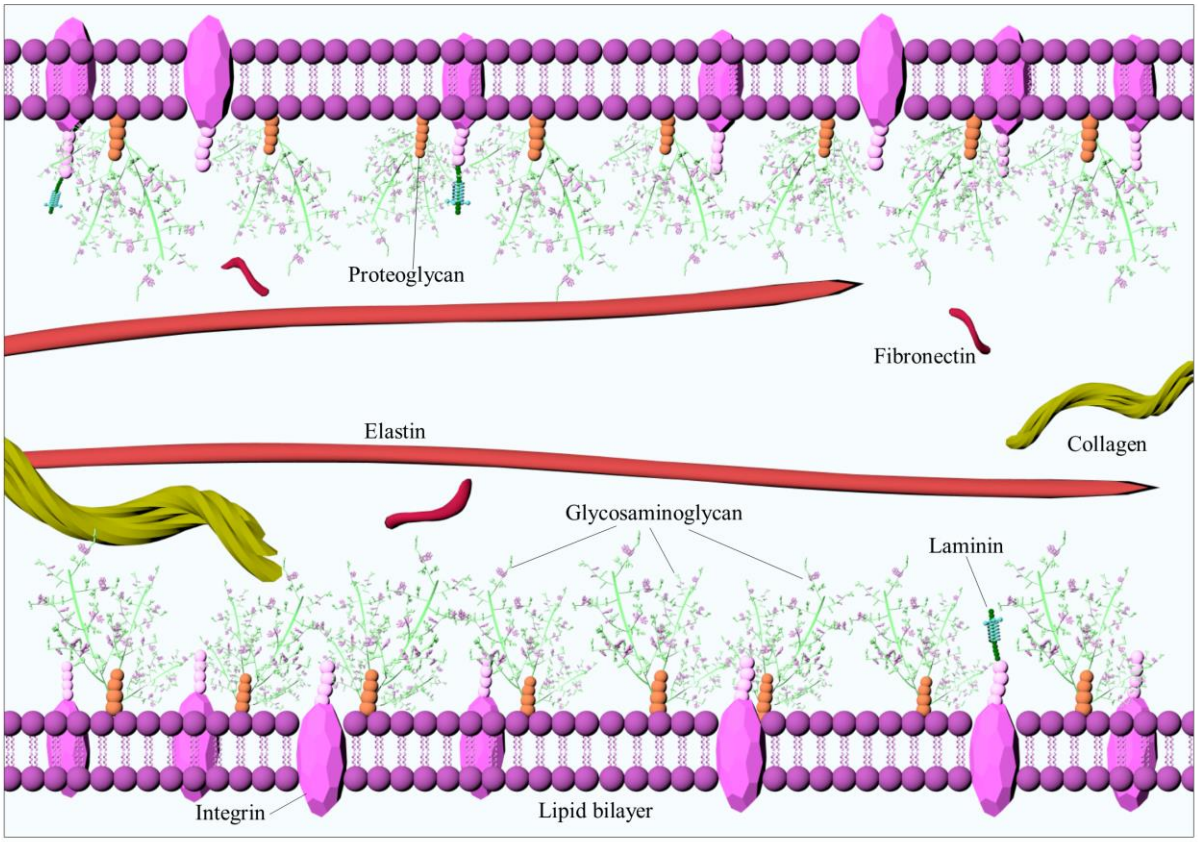

Figure 3: Schematic illustration of the ECM composition. ECM is an organized complex biochemical meshwork, which is mainly composed of two different units of structural entities form its composition: fibril-forming molecules and non-fibril forming molecules. These molecules are collagen, elastin and fibrin comprising fibril-forming units, and PGs and GAGs comprising non-fibril forming units. Adapted with permission from [24].

A milestone toward the goal of MR imaging-based atherosclerotic plaque characterization lies in better-understanding interactions of metal-based CAs with the ECM composition by improved detection of CA metals. In this regard, elemental analysis has emerged as an advanced analytical approach, which provides great sensitivity and spatial resolution in detection of elements in situ. Among such approaches, mass spectrometry (MS) and synchrotron radiation μXRF (SR-μXRF) spectroscopy are two cutting-edge techniques offering the lowest limit of detection (LOD) and highest spatial resolution, respectively [42, 89]. MS is superior in measuring isotope ratios with high sensitivity owing to specific mass-to-charge ratios (m/z) of elements [89]. Matrix-assisted laser desorption ionization MS (MALDI-MS) is the most extensively used method for mapping of elements and small biomolecules, or for protein identification and characterization on histological specimen [90]. However, matrix-related interferences present a challenge for quantification. Inductively coupled plasma (ICP) coupled

to the MS helps overcome this challenge due to effective medium for vaporizing, atomizing and matrix-independent ionizing the specimen composition for subsequent detection [91]. Laser ablation (LA) was introduced as an imaging MS technique by coupling it to the ICP-MS, which enabled direct and fast measurements and spatial mapping of elements on ex vivo tissue sections [92]. On the other hand, SR-μXRF analysis is gold standard in imaging and detecting elements in biological systems at low and submicrometer spatial resolution [93]. Hard X-ray's large penetration depth and absence of bremsstrahlung enable non-destructive investigation on cellular and even subcellular level, which makes SR-μXRF capable of quantitative imaging of whole cells [93-95].

In this dissertation study, we aimed at better-understanding microdistribution of CA metals from experimentally available IONPs (Eu-VSOPs) and clinically used GBCAs (Gd-BOPTA, gadobenate dimeglumine) in arterial tissue sections at different stages of atherosclerotic plaque progression. We utilized IHC and correlative elemental microscopy by LA-ICP-MS and SR-μXRF.

3.2. Materials and Methods

This thesis study was performed on archived arterial tissue specimens obtained from a previous MRI study on the New Zealand White (NZW) rabbit model of atherosclerosis, which examined signal changes in the vessel wall induced by very small IONPs (VSOPs) and Gd-BOPTA following IV injection. The study was conducted in accordance with the requirements of directive 2010/63/EU and the German Animal Protection Act and approved by the local animal protection committee of the Landesamt für Gesundheit und Soziales (LAGeSo, Berlin State Office for Health and Social Affairs, Germany). Experimental conditions were constant at all times and have been explained in detail elsewhere [96].

Twelve male NZW rabbits (Charles River Laboratories Germany GmbH, Sulzfeld, Germany) with initial body weights of 1.5 – 2.0 kg were kept individually in conventional cages with access to water and hay briquettes ad libitum. For induction of atherosclerosis, they were fed pelleted complete diet supplemented by 0.2% cholesterol (Altromin Spezialfutter GmbH & Co. KG, Lage, Germany) ad libitum for a total of 26 weeks. At 4 and 8 weeks after the start of the diet, the rabbits were subcutaneously injected with heat shock protein (65 kD HSP from Mycobacterium bovis BCG, fragment 180-188, Sigma-Aldrich Chemie GmbH, Steinheim, Germany). At 8 weeks after the start of the diet, vascular endothelial growth factor (recombinant human VEGF, Sigma-Aldrich Chemie GmbH, Steinheim, Germany) was intravenously (IV) injected (see also *electronic supplementary material* for induction of atherosclerosis and the animal model) [96].

The rabbits were IV injected with VSOPs at a dose of 0.05 mmol Fe/kg body weight. VSOPs were synthesized at the Radiology Department of Charité – Universitätsmedizin Berlin according to the following properties: 0.5 M Fe concentration with 13% citric acid (weight/weight total Fe), 3 g/l sodium glycerophosphate, 2 g/l N-methylglucamine, and 60 g/l mannitol [97]. Analytical discrimination of VSOPs from endogenous Fe was obtained by europium (Eu) doping of the particles, resulting in Eu-VSOPs. This resulted in no alterations in the magnetic properties of the particles [96]. At 1 h after Eu-VSOP injection, 10 rabbits were IV injected with Gd-BOPTA at a dose of 0.1 mmol/kg. 2 h after the initial CA administration, the rabbits were sacrificed. The vascular system was perfused with electrolyte solution, the aortic arch was removed and processed at 4°C overnight by formalin fixation and embedded in paraffin. Marcus Makowski kindly provided atherosclerosis-free control

specimens (Eu-VSOP-negative and Gd-positive controls were from rabbits examined with administration of Vasovist and elastin-specific CA (BMS753951) at a dose of 0.2 mmol/kg) were. These were processed under the same conditions.

IHC analysis were performed on the 5 μm serial sections of formalin-fixed arterial specimens. Adjacent sections were subjected to Movat's pentachrome, von Kossa, and Alcian blue (pH 1.0) histologic staining, anti-SMC actin (anti-SMA), and anti-rabbit macrophage (anti-RAM-11) immunostaining. Score-based semiquantitative assessment of plaque pathomorphology was done according to the pathologic features defined by the American Heart Association (AHA) (Table 1). Digital high-resolution scans of the histologic specimens were obtained at the Zentrale Biomaterialbank der Charité (ZeBanC).

Table 1: Pathologic features of atherosclerotic plaque progression and AHA classification. Adapted with permission from [96].

Lesion type	**Pathomorphologic characteristics**
Early (types I-III)	➢ Low level of ECM accumulation with fatty streaks, no or minimal level of macrophages. ➢ Intact and thick media with contractile SMC phenotype. ➢ Prone to progression. (Type III=**preatheroma**).
Advanced (types IV-V)	➢ Increasing lipid and ECM accumulation. ➢ Increasing macrophage content in the intima, foam cell formation, apoptosis. Lipid cores are detectable, covered by the fibrous cap. ➢ Medial thinning, synthetic SMC migration into the intima. ➢ Fibrous atheroma, calcified atheroma or fibrotic atheroma.
Advanced (types VI-VIII)	➢ Increased ECM degradation and remodelling. ➢ Enlarging lipid cores, necrotic core formation. ➢ Matrix-metalloproteinase activity results in thinning of fibrous cap. ➢ Atheroma types transform into vulnerable plaque. ➢ Hematoma/haemorrhage and/or thrombotic deposit.

Elemental imaging of arterial specimens by LA-ICP-MS was performed in collaboration with Bayer AG, MR & CT Contrast Media Research, Berlin, Germany. For that, an ICP-MS was

coupled to a laser ablation system. Sections were deparaffinized prior to the analysis. Laser ablation was performed in continuous-line ablation mode with a circular laser spot size of 20 μm at a scanning speed of 100 μms^{-1} and 200 ms acquisition time with daily-optimized output energies of 1.5 Jcm^{-1}. Ablated tissue was transported into the ICP-MS imager with helium gas at a flow of 0.9 L/min. Matrix-matched laboratory standards of well-defined element concentrations were spiked onto gelatine and scanned to quantify arterial vessel wall (media, intima and endothelium) Gd and Fe concentrations (Fig. 4). Eu signal was only recorded in terms of counts per second (CPS) due to unavailability of standards. Generation of 2D distribution maps, image processing and data evaluation were performed using MassImager, a free software developed by Robin Schmidt. LA-ICP-MS analysis, image processing and data analysis have been explained elsewhere [96]. Accordingly, an image was generated using a set of predefined analysis parameters such as. The 'freehand' detection tool was used to distinguish the arterial vessel area. Regions of interest (ROIs) were drawn to calculate relative signal intensity in CPS. Mean signal intensity values were extracted and transferred to Microsoft Office Excel, and a regression formula was calculated. This formula was inserted back into the respective panel in the MassImager software, and histogram analysis was performed to determine data distribution, standard deviation, minima, and maxima. To reduce the background noise signal for iron (Fe), europium (Eu), and gadolinium (Gd), minima were set to 99.0 nmol/g, 49.5 (CPS), and 0.5 nmol/g, respectively, and maxima were set to 2%, 1%, and 1%, respectively. Concentrations and standard deviations were transferred back to Microsoft Office Excel, where they were categorized under the respective lesion type (control, early lesion. and advanced plaque). Mean concentrations and their respective standard deviations were calculated, concentration graphs were drawn, and error bars were generated.

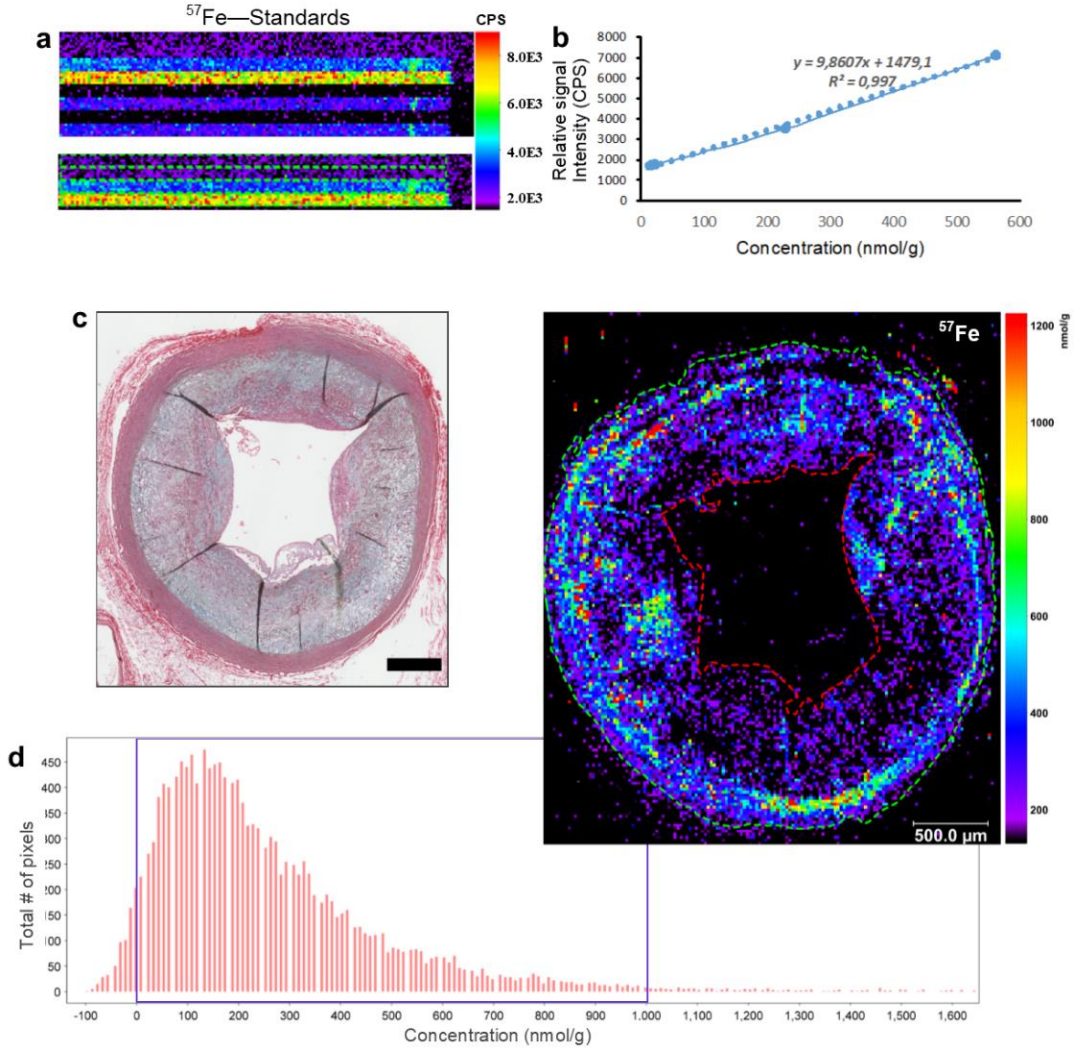

Figure 4: Matrix-matched calibration and iron (Fe) quantification by laser ablation inductively coupled plasma mass spectrometry (LA-ICP-MS). **a** Control specimens with defined concentrations of Fe were scanned. Measurement results were obtained in terms of relative signal intensity recorded in counts per second (CPS), which were further calculated to define elemental concentrations in defined region of interest (ROI). **b** Quantification of elements in the arterial vessel wall (media, intima and endothelium) was done by applying regression formula. **c** Plaque boundaries were defined by Movat's-staining. Vessel wall area (green dotted line) was separated from the lumen (red dotted line) by 'freehand' detection tool **d** Data distribution, standard deviation, minima and maxima were calculated by histogram analysis. Scale bars: 500 µm. Adapted with permission from [96].

Elemental imaging of arterial specimens by SR-µXRF was performed following LA-ICP-MS analysis. Experiments were done at the ID21 beamline at the European Synchrotron Radiation Facility in Grenoble, France, using the routine procedures developed and implemented by the Beamline Instrumentation Software Support (BLISS) group. Experiments were performed using the in-vacuum scanning X-ray spectroscopy setup, in which X-rays were generated by undulators with a gap size optimized for 7.3 keV. The X-ray beam was focused down to ~0.6 X 0.8 µm2 (vertical X horizontal) using a fixed-curvature Kirkpatrick-Baez mirror system. Flux was ~5 X 10^{10} photons/s (~180 mA SR current in multibunch mode). Acquisition time per pixel

was 100 ms. Pixel size for generating the XRF maps was set to 30 μm, 10 μm, 1-2 μm, or 0.5 μm depending on the ROI size. Scans were acquired in continuous mode. Distribution maps of Fe, Gd, sulfur (S), P, and Ca were generated. XRF spectroscopy normalization, spectral deconvolution, generation of 2D elemental distribution maps, and quantification were done using PyMCA (Python multichannel analyser) software according to the routine applications developed and implemented by the ESRF Beamline Instrumentation Software Support (BLISS) group (Fig. 5). SR-μXRF analysis, image processing and data analysis have been explained elsewhere [96]. PyMCA implements most of the procedures needed for XRF spectroscopy and extracts elemental concentrations in terms of mass fractions or molar concentrations based on assumptions about matrix composition. We used published data on the matrix composition of arterial tissue specimens [98]. Only predefined ROIs based on IHC findings were quantified by SR-XRF analysis. For that, the 'freehand' detection tool was used to distinguish the ROI area. Molar concentrations of Gd, Fe, P, and Ca at spatial resolutions of 10 μm, 1-2 μm, or 0.5 μm, depending on the size of the ROI and the measured XRF spectrum in each point of the image were extracted. These values were transferred to Microsoft Office Excel, where they were categorized under the respective lesion type (control, early lesion and advanced plaque). Mean molar concentrations were calculated, and concentration graphs were generated. Cellular uptake of Gd was investigated by analysing P distribution as a marker of cell membrane, ATP, and nucleic acids. XRF spectra of advanced plaque sections at 0.5 μm resolution were analysed using a 25% threshold. Areas with fluorescence below and above the threshold were revaluated, and concentrations were compared. Size distribution analysis of Gd hotspots was done using ImageJ software.

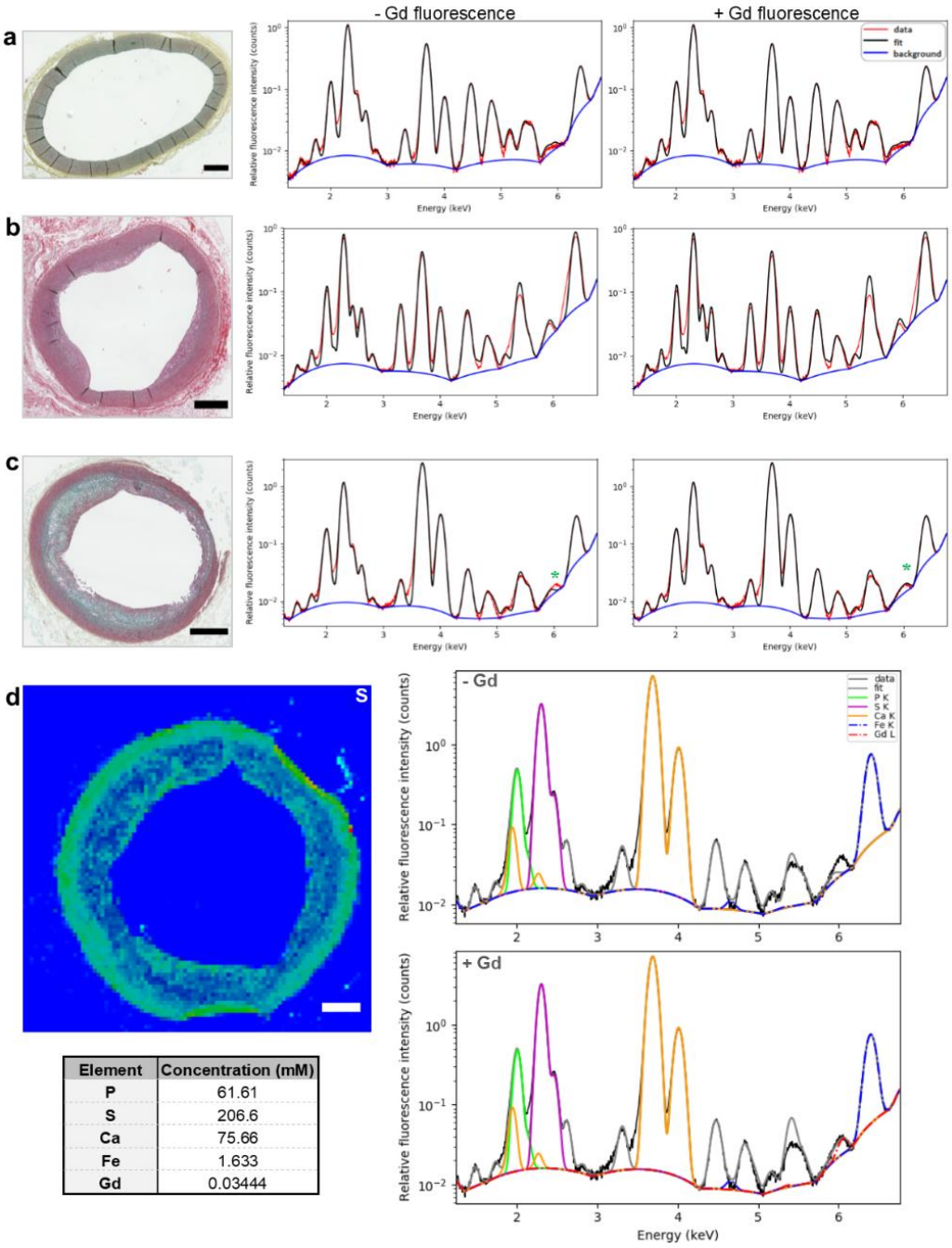

Element	Concentration (mM)
P	61.61
S	206.6
Ca	75.66
Fe	1.633
Gd	0.03444

Figure 5: Quantification of arterial element concentrations by synchrotron radiation µX-ray fluorescence (SR-µXRF) spectroscopy. **a-c** In the absence (*left*) versus presence (*right*) of characteristic Gd L-line fluorescence, data and fit overlay were displayed by spectral deconvolution: **a** healthy artery (control)**, b** early lesion**, c** advanced plaque**.** Movat's staining provided comparison. When the respective element content is beyond the limit of detection, the fit in the absence versus presence of Gd fluorescence remains unchanged. Change in the fit confirms Gd detection (asterisk). **d** Sulfur (S) distribution maps were used to define the arterial boundary on the Gd-detected sections, after which XRF spectra are obtained and analysed to determine colocalizing elements. Scale bar: 500 µm. Adapted with permission from [96].

3.3. Results

IHC analysis of the arterial specimens obtained from 14 rabbits revealed atherosclerotic plaques at different stages of development, which were categorized into early lesions and advanced plaques using the pathologic plaque features defined by the AHA (Fig. 6, Table 1, control: n=2, early lesion: n=3, advanced plaque: n=9). Movat's staining revealed medial and endothelial regions of the arterial vessel wall as the major cellular areas, which were confirmed by SMA and RAM-11 immunostaining**.** Medial or intimal SMCs were distinguishable by their spindle-like and circular shapes, respectively. Non-staining circular, cleft- or vacuole-like areas revealed lipid pools majorly at the intimomedial interface with increased macrophage colocalization, which were surrounded by light blue-stained GAG networks. Yellow/green-stained collagen fibrils and synthetic SMCs were seen surrounding the lipid pools. Arterial calcifications were identified by von Kossa staining at higher magnification through local increase in the darker brown colour especially along the intimomedial interface of advanced plaques.

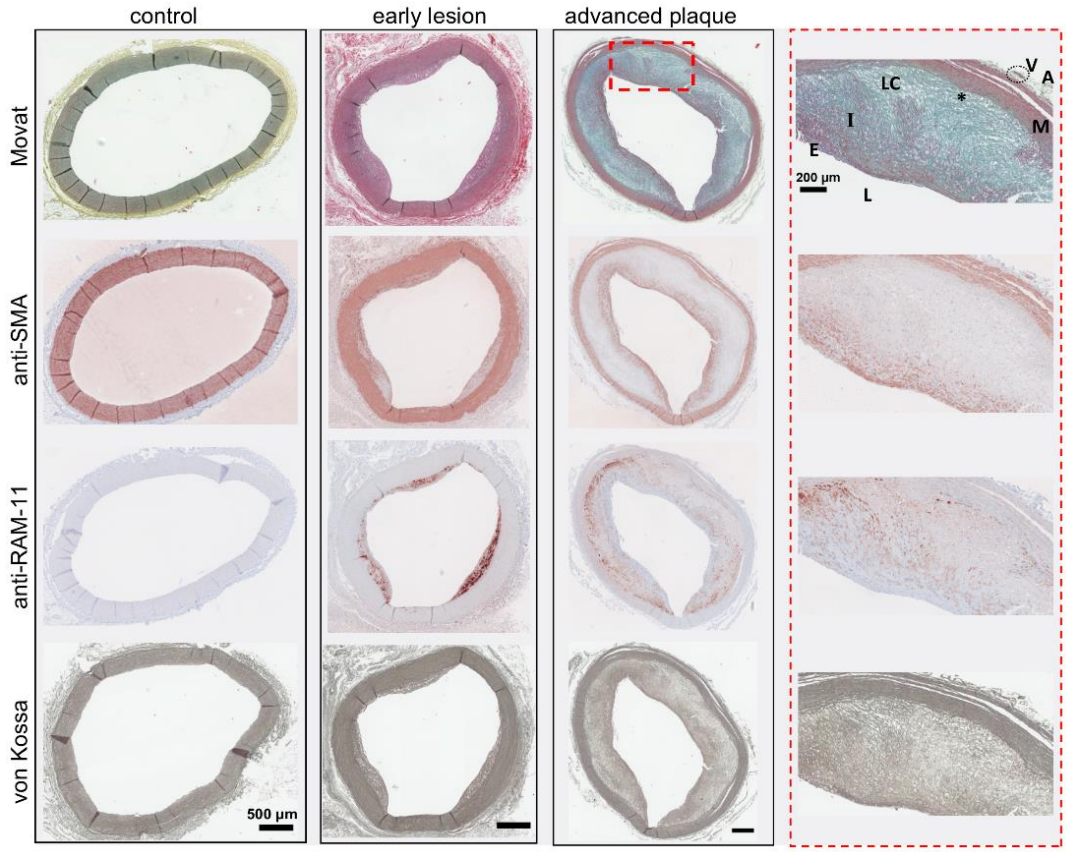

Figure 6: Immunohistochemical (IHC) characterization of atherosclerotic plaques. Advanced plaque ROI (× 10 magnification) is provided for comparison. Movat's staining (red) reveals cells. Immunostaining against smooth

muscle cells (SMCs / anti-SMA) and macrophages (anti-RAM-11) revealed SMCs and macrophages, respectively. Unstained lipid pools are circular, cleft- or vacuole-like shapes at the intimomedial areas indicating foam cell or lipid cores, with increased macrophage colocalization. These are surrounded by GAGs (light blue). Von Kossa staining depicts calcifications in the intima, especially along the intimomedial interface of advanced plaques. Scale bars, 500 µm; ROI, 200 µm; L, lumen; E, endothelium; I, intima; LC, lipid core; asterisk, intimomedial interface; M, media; A, adventitia; V, vasa vasorum. Adapted with permission from [96].

Elemental microscopy results matched IHC characterization. S distribution matched the anatomy of arterial vessel wall layers and P distribution revealed cellular areas (Fig. 9, Fig. 11). LA-ICP-MS detected Gd and Fe with a limit of detection of ~0.1 nmol/g and ~100 nmol/g, respectively a (20 µm resolution, x-y direction). VSOPs were identified through Eu-positive signal, which differentiated nanoparticle distribution from that of endogenous Fe. No Eu signal was detected in controls (Fig. 7). Weaker Eu signal was detected in the media and intima of early lesions. Eu signal intensity and Fe concentrations were higher in advancing plaques. High Eu signal was confined to endothelium or the intimomedial interface. Fe concentrations were 146.17 nmol/g (±52.58 nmol/g) in healthy arteries, 264.89 nmol/g (±79.23 nmol/g) in early lesions, and 583.20 nmol/g (±122.46 nmol/g) in advanced plaques.

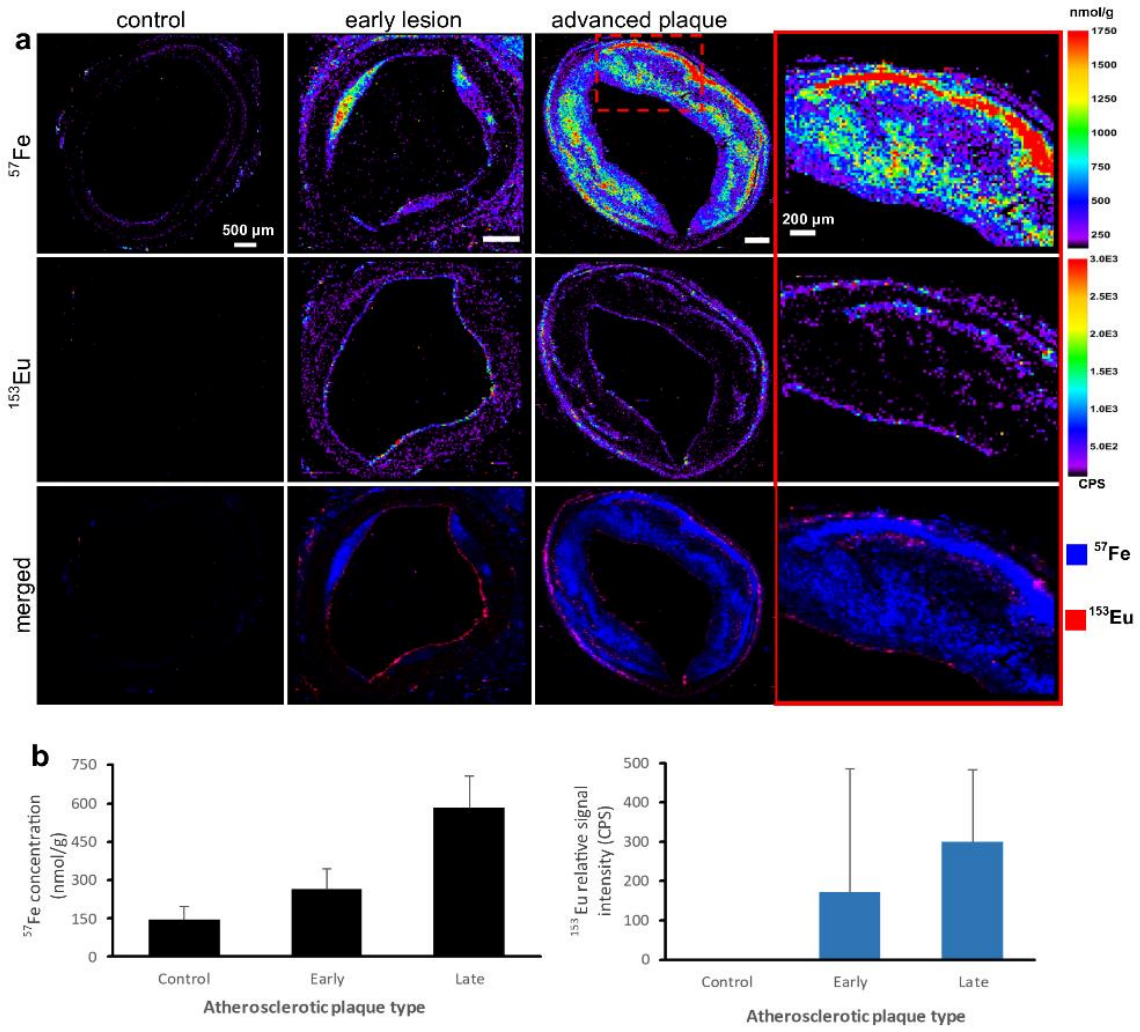

Figure 7: Atherosclerotic plaque microdistribution of Europium (Eu)-doped very small superparamagnetic Fe oxide nanoparticle (Eu-VSOPs) analysed by LA-ICP-MS. **a** $^{57}Fe^{1+}$ and $^{153}Eu^{1+}$ distribution maps. Advanced plaque ROI is provided for comparison. Nanoparticle distribution from that of endogenous Fe was detected indirectly through Eu-positive signal intensity (CPS). No Eu signal is detected in controls; weaker Eu signal is detected in the media and the intima of early lesions. Advanced plaques are characterized by increasing Eu signal intensity and Fe concentrations. High Eu signal is confined to endothelium or to the intimomedial interface. Scale bars: 500 µm, ROI: 200 µm. **b** Fe concentration and Eu signal intensity graphs confirm correlations of Fe concentration and Eu signal intensity with plaque progression. Adapted with permission from [96].

In the control group (Eu-VSOP-negative, Gd-positive), Gd was detected (Fig. 8). Gd distribution was homogeneous in healthy arteries and inhomogeneous in early and advanced plaques with increasing concentrations in the subendothelial space. Advanced plaques were characterized by high focal Gd content at the intimomedial interface. Gd concentrations were 2.22 nmol/g (±0.14 nmol/g), 1.63 nmol/g (±1.19 nmol/g), and 9.23 nmol/g (±4.64 nmol/g), with maximum concentrations of 5.30 nmol/g, 22.85 nmol/g, and 113.66 nmol/g in healthy arteries, early lesions, and advanced plaques, respectively.

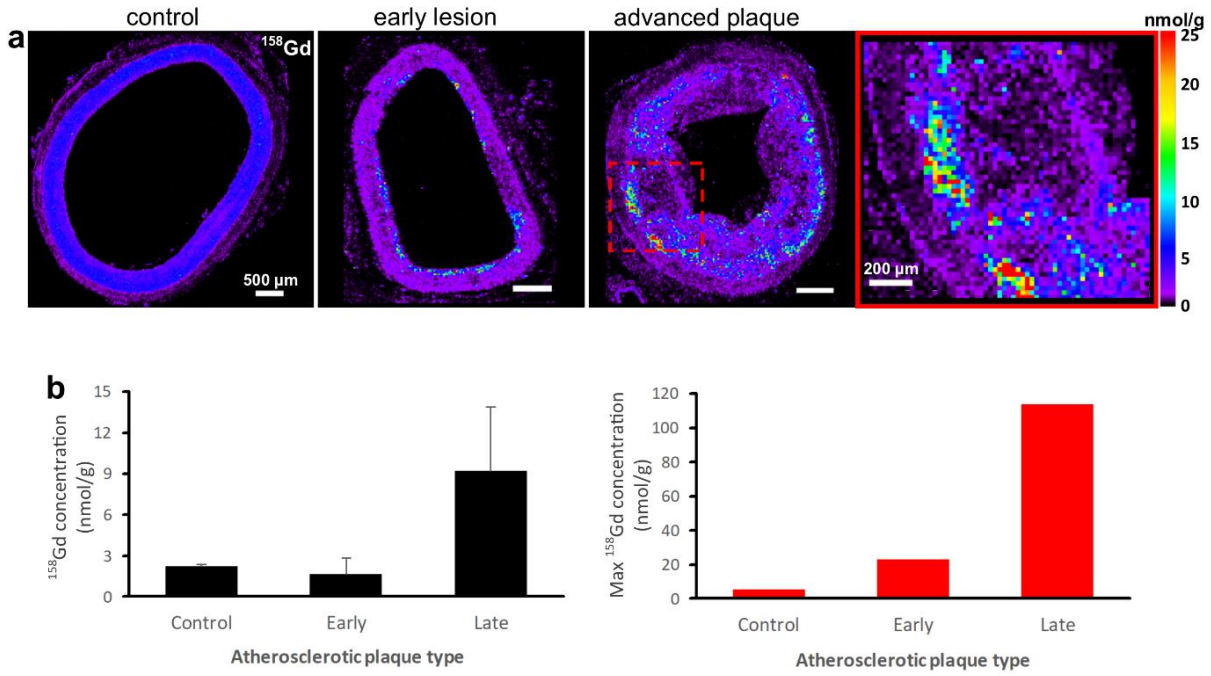

Figure 8: Atherosclerotic plaque microdistribution of Gd analysed by LA-ICP-MS. **a** ^{158}Gd distribution maps. Advanced plaque ROI is provided for comparison. In the control group, Gd is detected (Eu-VSOP negative, Gd-positive). In healthy arteries, Gd distribution is homogenous and global. Gd concentrations are higher in the subendothelial space in early lesions. High focal Gd content at the intimomedial interface were detected in advanced plaques. Scale bars: 500 µm, ROI: 200 µm. **b** Gd and maximum Gd concentration graphs in atherosclerotic plaques revealed no Gd correlation with plaque progression but with max Gd concentration, which confirm Gd-hotspots. Adapted with permission from [96].

SR-µXRF analysis at 30 µm step width detected Gd in 4 samples – one early lesion and 3 advanced plaques. Predefined ROIs within these specimens were further investigated for their Gd content at higher resolutions down to 0.5 µm, which resulted in increasing Gd concentrations (Fig. 9). Higher-resolution scans revealed higher local Gd, P, and Ca concentrations in advanced plaques (Fig. 9-10).

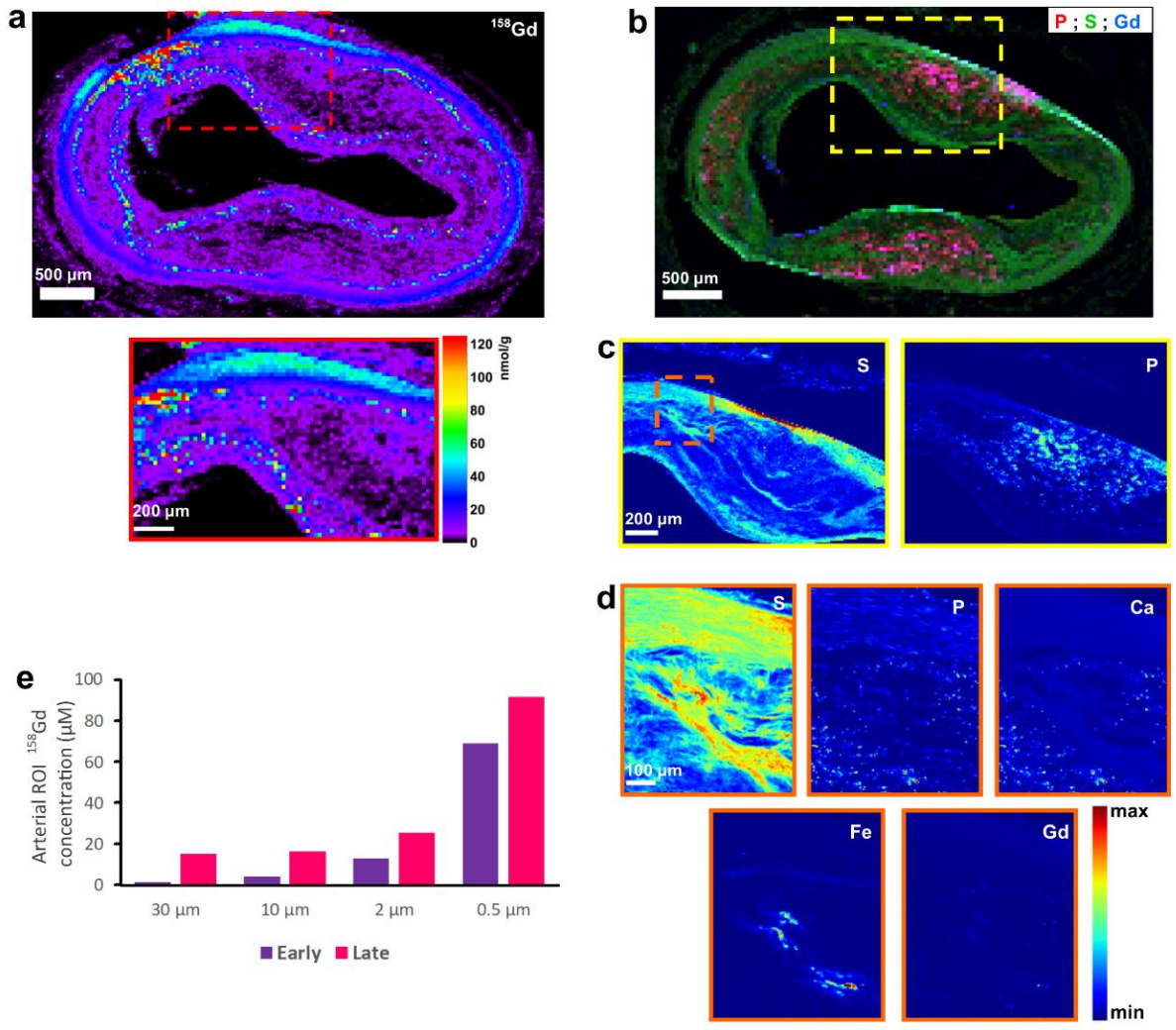

Figure 9: Gd hotspots and spatially resolved Gd microdistribution. **a** ^{158}Gd distribution maps analysed by LA-ICP-MS. Advanced plaque ROI is provided for comparison. Scale bars: 500 µm, ROI: 200 µm, **b** RGB overlay of P, S, and Gd distribution maps at 30 µm resolution analysed by SR-µXRF. **c** Vessel wall anatomy and cellular zones of ROIs were characterized by S and P distribution maps, respectively, at 10 µm resolution; **d** S, P, calcium (Ca), Fe, and Gd distribution maps at 2 µm resolution. Scale bars: b1: 500 µm, b2: 200 µm, b3: 50 µm. **e** Increasing Gd concentrations in ROI with respect to increasing spatial resolution were detected both in early lesions and advanced plaques. Adapted with permission from [96].

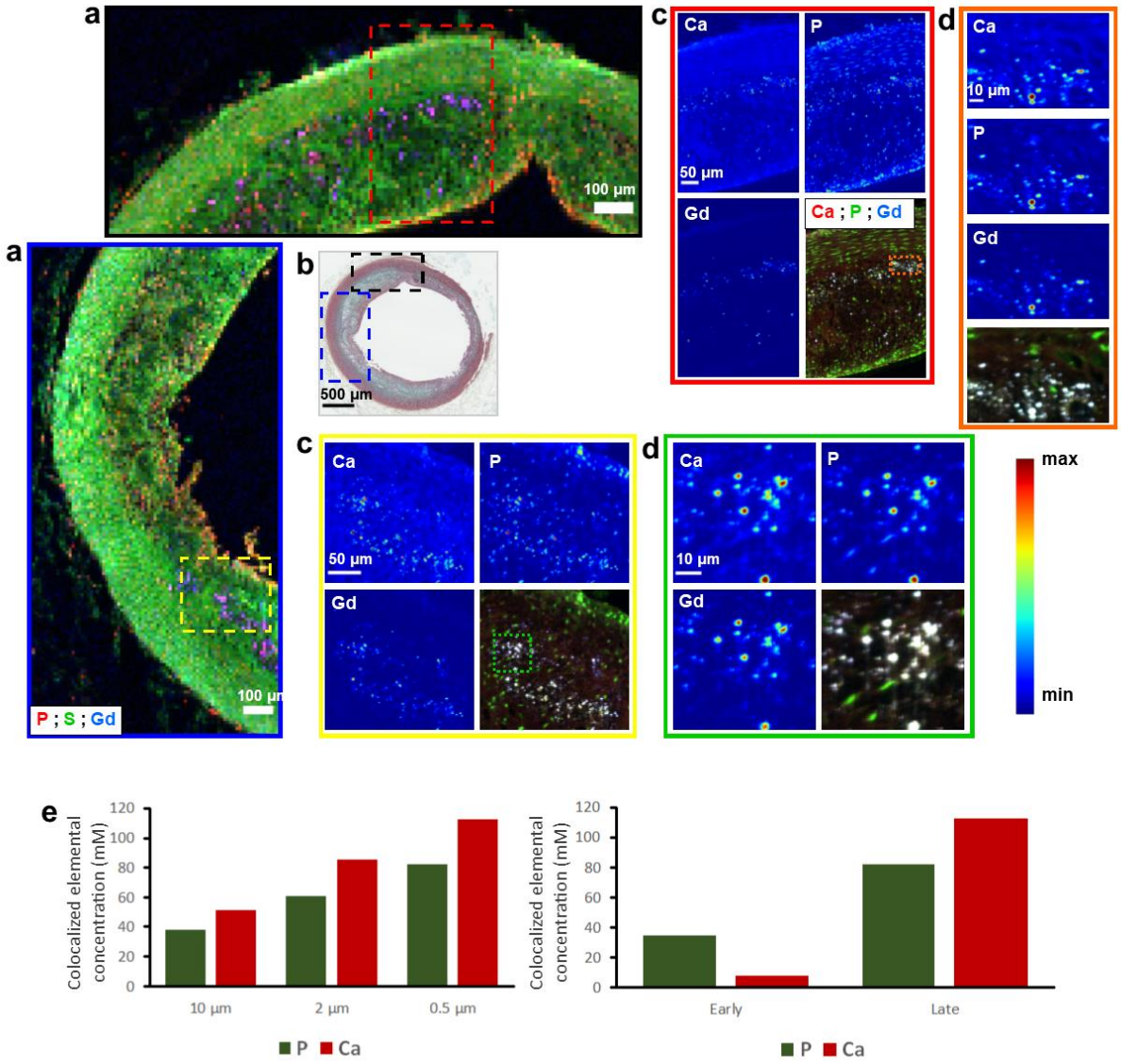

Figure 10: Gd-hotpots, P and Ca colocalization in atherosclerotic plaques analysed by SR-µXRF. 2 ROIs in an advanced plaque are provided for comparison. **a** RGB overlay of P, S, and Gd distribution maps at 10 µm resolution. Scale bars: 100 µm. **b** Overview of the plaque specimen by Movat's staining. **c** Distribution maps and RGB overlay of Ca, P, and Gd at 2 µm resolution. Scale bars: 50 µm. **d** Distribution maps and RGB overlay of Ca, P, and Gd at 0.5 µm resolution. Scale bars: 10 µm. **e** In advanced plaques (*right*), Gd hotspots were detected to contain higher P and Ca concentrations with respect to increasing spatial resolution (*left*). Adapted with permission from [96].

SR-µXRF analysis at 10 µm and 2 µm step width and RGB overlay of P, S, and Fe maps demonstrated Fe distribution around cell- or collagen-rich areas in the intima (Fig. 11). RGB overlay of Gd, S, and Fe maps showed higher Gd concentrations along the intimomedial interface or within the deeper subendothelial space, distinguishing Gd distribution from that of Eu-VSOPs. Analysis of possible cellular uptake of Gd yielded Gd, P, and Ca concentrations of 0.12 mM, 62.03 mM, and 87.66 mM, respectively, in areas below

the threshold (Fig. 12). In areas above the threshold, which indicates elemental hotspots, these concentrations were 2.57 mM, 779.85 mM, and 789.85 mM, respectively. Size distribution analysis revealed Gd-rich hotspots ranging from a few micrometers to submicrometers in size. Such hotspots localized at higher density in spot-like darker brown/black areas depicted by von Kossa staining that could be better seen at higher magnification especially along the intimomedial interface.

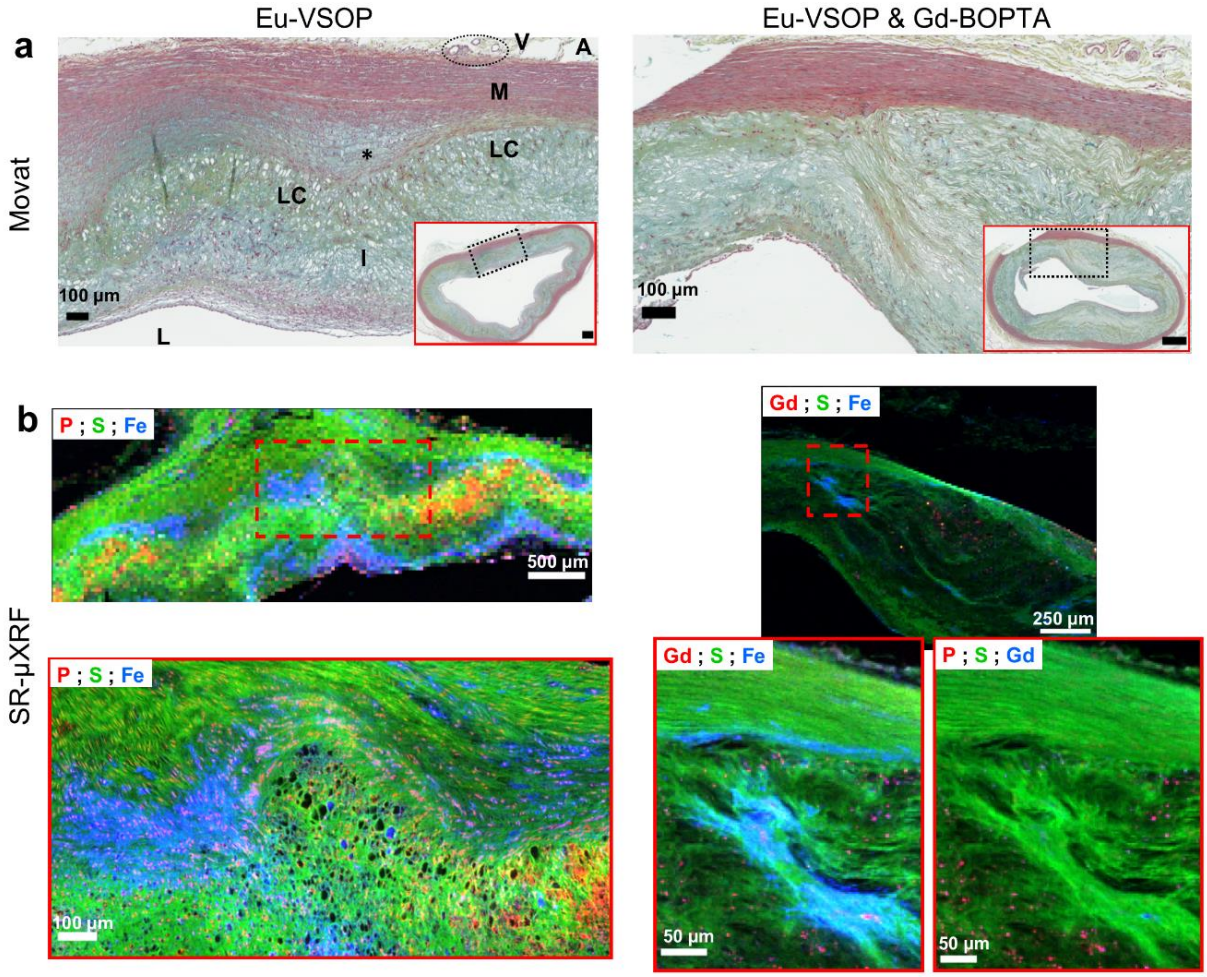

Figure 11: Atherosclerotic plaque microdistribution of Fe and Gd. Rabbits were IV injected with either Eu-VSOP alone (*left*) or Eu-VSOP and Gd-BOPTA (*right*). **a** Movat's stained histochemical characterization of an advanced plaque pathomorphology. (ROIs - 10X magnification). Synthetic SMCs (red) and dense stretches of collagen (yellow/green) fibril mesh are seen in the subendothelial space, intima and intimomedial interface covering lipid pools. Scale bars: 500 µm, ROI: 100 µm. **b** SR-µXRF analysis at 10 µm and 2 µm resolution (ROIs are indicated by red dashed lines). RGB overlays of P, S, and Fe distribution maps demonstrate Fe distribution in cell- or collagen-rich areas in the intima (*left*, scale bars: 500 µm, ROI: 100 µm). Intimomedial interface or deeper subendothelial space were characterized to contain higher Gd concentrations, which can be seen by the RGB overlays of Gd, S, and distribution Fe maps, also distinguishing Gd microdistribution from that of Eu-VSOP. (*right*, scale bars: 250 µm, ROI: 50 µm). L: lumen, I: intima, LC: lipid core, asterisk: intimomedial interface, M: media, A: adventitia, V: vasa vasorum. Adapted with permission from [96].

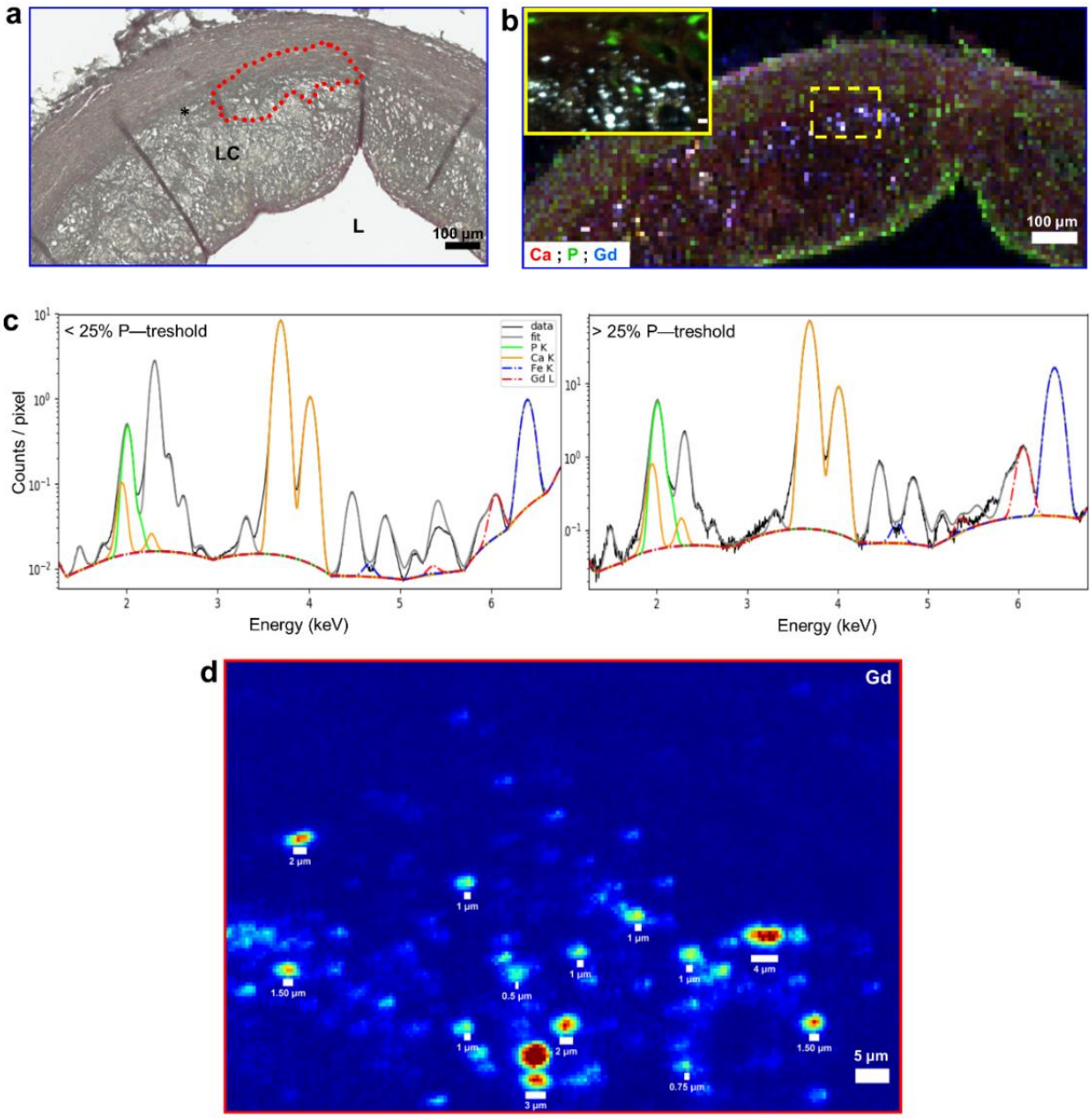

Figure 12: Gd impact on arterial calcification. **a** Arterial calcifications (dashed red lines or asterisk) are revealed by von Kossa-staining, which are more pronounced at the intimomedial interface (Advanced plaque ROI – 15X magnification). Scale bar: 100 µm; L, lumen; LC, lipid core. **b** RGB overlays of Ca, P, and Gd distribution maps analyzed by SR-µXRF at 10-µm and 0.5-µm resolution (yellow dashed lines mark ROIs). Scale bars, 100 µm; ROI, 5 µm. **c** P distribution maps were analyzed to investigate Gd uptake by cells, in that P distribution marks cell membranes, ATP, and nucleic acids. 0.5-µm resolution maps are segmented into two compartments by applying a 25% threshold on the maximum of the P K-line fluorescence signal and comparing elemental concentrations in P-poor (<25% P-threshold) or P-rich (>25% P-threshold) areas. In contrast to P-poor areas with < 1 mM, 62 mM, and 87mM of Gd, P and Ca, respectively, P-rich areas contained > 2 mM, 779 mM, and 789mM of Gd, P and Ca, respectively, which indicate a potential cellular response to Gd, presumably by those cells that undergo calcified apoptosis. **d** Gd-rich hotspots ranged in sizes between a few micrometers to submicrometers, which indicates Gd impact on arterial calcification. Adapted with permission from [96].

3.4. Discussion

Growing concerns of CVD manifestations due to obesity, diabetes or metabolic syndromes as well as risk factors such as genetic background, age, sex, lack of exercise or smoking necessitate improvements in the existing diagnostic approaches, placing development of early diagnostic tools as a central goal in medical research [1, 2]. Although identified as the underlying cause of CVD, routine clinical diagnosis of atherosclerosis still relies on the evaluation of compromised blood flow and the degree of luminal stenosis, but cannot reliably discriminate stable and vulnerable atherosclerotic plaques [7]. Underestimation of atherosclerotic plaques with angiographically mild arterial narrowing but still existing high risk state due to fissures reaching down to the deeper layers of the intima or persisting inflammation often happens, unless patients are administered to the hospital at the emergency due to stroke or myocardial infarction, which is already the end stage of the disease [26, 34]. For this reason, imaging for subclinical atherosclerosis and screening of asymptomatic patients at intermediate or lower risk are vital for prevention of improved CVD risk prediction and disease management [99].

In that regard, in vivo molecular imaging has become the core interest for new approaches of diagnostic research with rapid translations into the clinical practice to extend our understanding of fundamental disease mechanisms in humans and treatment of these diseases [100]. Molecular imaging brings different scientific fields including physics, medicine, chemistry, molecular biology and biochemistry, pharmacology and bioinformatics together into a new, highly interdisciplinary imaging field [101]. It covers a range of modalities, which aim at spatial-temporal sensing and assessment of molecular targets, characterizing cellular processes and monitoring cell or tissue phenotypes in biological systems under disease-associated pathological conditions [102]. In the focus of CVD, although earlier imaging studies mostly used radioisotope-derivatized monoclonal antibodies, efforts in the last two decades have set non-invasive imaging approaches to the center of medical diagnostic research, and resulted in growth in imaging reporters, among which GBCAs and IONPs have emerged as the most promising clinical and preclinical imaging agents [103, 104].

Contrast-enhanced MRI after IV injection of metal-based CAs is the first non-invasive technique that allowed identification of key inflammatory processes of atherosclerotic plaque progression [33]. It allows angiographic examination and assessment of local plaque composition as well as quantification of arterial plaque burden, which collectively make it the

ideal imaging modality for in vivo imaging and for the early diagnosis of atherosclerosis [35, 105, 106]. Potential MRI-based atherosclerotic plaque characterization relies on elucidating interactions of metal-based CAs within the tissue composition during plaque progression by improved detection of CA metals. ECM accumulation and degradation have been recognized as a major pathological process, raising attention towards MR imaging of the ECM [61, 64]. It is likely that metal-based CAs might distribute within atherosclerotic plaques through mechanisms involving metal dissociation and complexation with endogenous molecules and anionic components of the plaque ECM, especially GAGs [24, 48].

In a previous study that serves as the basis to this dissertation research work, we investigated correlations between vessel wall late gadolinium enhancement (LGE) in T1-weighted MRI and histologic markers of atherosclerotic plaque progression over a time course of 60 min [40]. We detected a steady increase from moderate to strong correlation between the LGE and the ECM material or calcifications (Fig. 2). This suggests that, despite macrophages being the most well-known markers of atherosclerotic plaque progression, arterial remodeling plays a central role in the atherosclerotic plaque formation and progression by altering the molecular make-up of the plaque ECM mostly because of unresolved inflammation [61, 107]. Both the plaque burden in terms of increasing ECM synthesis and specific types of pathological activities, e.g. calcifications, are useful factors to consider in contrast-enhanced MRI approaches.

This dissertation work aimed at better understanding the microdistribution of CA metals from IONPs (Eu-VSOP) and GBCAs (Gd-BOPTA) in arterial tissue sections at different stages of atherosclerotic plaque progression. However, it is essential to note why there would be different stages of atherosclerotic plaque formation among the animals, while only a single time-point experimental approach was performed. Certainly, it would be more important to perform a largely extended investigation also involving different time points, which would require the obligation of performing exactly matching experimental procedures on different animals. However, it is extremely difficult to fix such experimental procedures that involve a complicated series of steps including animal care, feeding, disease development, imaging, obtaining aortic specimens and further elemental microscopy. Furthermore, as much as temporally, atherosclerotic plaque progression is also a spatially heterogeneous process, which leads to not only different pathologies among the animals, but also even intra-organismal differences. This translates into different levels of plaque formation in different depths of the aortic system within one individual organism, thus it is likely that almost all AHA-defined

stages could be observed within the same animal. In this study, utilizing the same time-point experimental procedure was a simplified, yet a great strategy to eliminate significant deviations or errors that might result from the investigations on multiple time-points. Additionally, the work presented here focused on a sophisticated experimental approach that combines usual IHC workflow with cutting-edge analytical instrumental analysis in order to reach highest level of sensitivity and spatial resolution for quantification. We utilized correlative elemental microscopy by LA-ICP-MS and SR-μXRF spectroscopy, and achieved improved detection of CA metals in arterial tissue specimen (LOD ~ 0.1 nmol/g for Gd, spatial resolution of 0.5 μm). In summary, this study serves as an important basis for subsequent experimental MRI studies aiming at advanced characterization of atherosclerotic plaques, illuminating transition from stable to vulnerable plaque, and ultimately early diagnosis of atherosclerosis.

Early uptake of VSOPs (<2 h) into atherosclerotic plaques is currently being investigated for their potential in MR imaging of experimental atherosclerosis [58, 59]. Eu-doping of VSOPs allowed us to detect nanoparticles and discriminate their distribution from that of endogenous Fe by LA-ICP-MS [108]. In general, our results presented correlations of ECM material accumulation with Eu signal intensity, Fe concentration and maximal Gd concentration.We observed focal Eu-VSOP distribution mostly at the boundaries of the adventitia, media, and intima, along the endothelium and superficially in the subendothelial space (Fig. 7, Fig. 11). These findings are consistent with earlier studies, which suggest endocytosis and macrophage uptake of VSOPs [109, 109]. RGB overlay of P, S, and Fe maps exposed Fe distribution in cell- or collagen-rich areas (Fig. 11). Increased vasa vasorum activity leads to formation of neovessels that might enhance nanoparticle uptake into the plaque ECM, during which they might interact with Fe transport, Fe-S clustering or storage proteins, and highly sulfated GAGs (*electronic supplemental material* Fig. S2) [111].

A notable finding here was that the Gd concentration in the arterial vessel wall did not show correlation with the ECM material accumulation. However, maximum Gd concentrations were higher in early lesions compared to healthy arteries, which further increased in advanced plaques, indicating focal Gd hotspots. The hotspots were most prominent at the intimomedial interface of advanced plaques with high P and Ca colocalization (Fig. 8-10). SR-μXRF analysis of these at higher spatial resolution revealed Gd content exceeding mM concentrations. Gd uptake into atherosclerotic plaques may result in insoluble complex formation at the areas with high P and Ca colocalization (Fig. 10), [47, 48]. This might be triggered, if not initiated, by

partial breakdown of Gd-chelates at the endothelium or vasa vasorum or through complexation with serum albumin and interactions with collagen, proteoglycans, and tenascin [107]. Collagen network integrity in cartilage has been shown to be a determinant of gadopentate dimeglumine accumulation [112]. Remarkably, we observed dense stretches of collagen fibrils surrounding lipid-rich zones. This might lead to selective Gd deposition, possibly around the lipid pools enriched at the intimomedial interface, or by formations of Gd concentration gradients upon interactions with GAGs (Fig. 11, *electronic supplementary material* Fig. S1). GAGs are potent candidates for ligand competition reactions, especially with abundant divalent or trivalent cations nearby [24, 113]. Gd-BOPTA is negatively charged, nevertheless it is highly probable that Gd might partially dissociate from its chelate compound especially in metabolically active inflammatory parts of the atherosclerotic ECM. Interestingly, after incubation of GBCAs including Gd-BOPTA in heparin, which is a highly sulfated GAG type, MRI signal-enhancement was reported to increase significantly [48].

Inhibition of phagocytosis and macrophage apoptosis upon Gd exposure have been reported, although GBCAs are known to distribute extracellularly after IV administration [114, 115]. We speculated that, since high P distribution marks cell membrane, ATP and nucleic acids, SR-μXRF spectra obtained for P distribution at 0.5 μm resolution could corroborate a cellular response. As expected, after applying a threshold analysis on the P fluorescence spectra, higher Gd, P and Ca concentrations were detected in areas above the threshold, once again confirming Gd hotspots and providing further support to insoluble complex formation. Size distributions of these hotspots from a few micrometers to submicrometers indicates Gd impact on arterial calcification, presumably taking place by extracellular mineralization or calcified apoptosis. (Fig. 12, *electronic supplementary material* Fig. S5) [116]. Whether Gd joins the calcification process by concentration-dependent means, or it might possess a causal role were not investigated, though it is of high importance for further investigations.

Known as a highly regulated process of atherogenesis, arterial calcification is similar to bone formation, occurs simultaneous to lipid accumulation in the enlarging neointima, and becomes a key characteristic of advanced plaques [117]. The earliest calcification in atherosclerotic lesions occur in apoptotic SMCs, which form membrane bound vesicles that actively calcify in different forms consisting of speckles, fragmented or diffuse calcifications [7]. In human atherosclerotic lesions, unesterified cholesterol and hydroxyapatite have been detected in close association, in which lipid molecules like cholesterol tend to crystallize upon hydroxyapatite

seeds [118]. Calcifications are often detected by histological methods involving von Kossa staining or Alizarin red S staining. Von Kossa staining is based on the binding of silver ions to the anions (phosphates, sulphates, or carbonates) of calcium salts, and the reduction of silver salts to form dark brown or black staining [119]. Although histological detection stand-alone is a weak, ill-posed approach, and remains insufficient in obtaining conclusive results as staining protocols are mostly non-specific due to chemical treatments and washing steps (e.g. ethanol washing, washing with water, washing with chemical dyes, etc.), they can still be detectable as spot-like local increase in the darker brown/black colour. In this study, at higher magnification visualization, such areas were detected locally especially at the intimomedial interface of advanced atherosclerotic plaques, which also correspond to areas with enriched Gd, P and Ca content (Fig. 6, Fig. 10, Fig. 12, *electronic supplementary material* Fig. S1, Fig. S5). These findings are in line with studies reporting calcified deposit formation in the form of microzones predominantly in the muscoelastic layer of the thickening intima, where they lead to destruction of elastin fibers [120, 121].

In another study aiming at investigating changes in the biophysical properties of cells and tissues after administration of clinical GBCAs, we reported important results that support the findings presented here in this dissertation research work [122]. In that study, we performed real-time deformability cytometry to human blood samples from 6 donors, which were treated with 3 different GBCAs and Gd trichloride at the conditions that mimic clinical doses and exposure times. Lymphocytes, monocytes and neutrophils are subtypes of blood leukocytes, which were measured and characterized with respect to their physical properties including size and brightness, were all found to become significantly stiffer (3% - 13%, $P < 0.01$) independent of the steric structure or charge or stability of the GBCA. These findings confirm the findings that GBCAs are indeed likely to encounter cellular response starting with blood cells and vascular endothelial cells after IV administration [123, 124]. Thus, in enlarging atherosclerotic plaques, where the endothelium becomes dyfunctional leading to increased permeability, it is possible that quantities of GBCAs, whether intact or partially dechelated, or as free Gd^{3+} ions, can enter cells after or during penetration into the growing intima, especially when they are in the close vicinity of those cells that participate in extracellular mineralization or that undergo calcific apoptosis [47, 48].

There are several limitations of this dissertation study comprising small sample size, and histological processing of the archived aortic material. Although useful from the statistical standpoint, examination of a larger sample set would have not been feasible for elemental microscopy during our granted beam-time at the European Synchrotron Radiation Facility. Additionally, tissue fixation, paraffin embedding, and washing steps are standard applications in IHC. However, histological detection stand-alone is an ill-posed approach, and remains insufficient in obtaining conclusive results as washing steps in staining protocols (e.g. ethanol washing, washing with water, washing with chemical dyes, etc.) might have altered the elemental concentrations, particularly for elements involved in transient interactions. Taking this into account, none of the results of this study was presented relying solely on histological staining, but these were rather used to provide the basic level of data interpretation, upon which or taken together with the other applied cutting-edge analytical methods, further corroborations and much stronger interpretations were obtained. Finally, the images provided in the dissertation had to be processed to lower image qualities. Ultimately, atherosclerotic plaque characterization should be done on higher-resolution images at higher magnification, which also constituted the basis of the characterization approach for the original publication.

3.5. Conclusion

This dissertation work aimed at better understanding the microdistribution of CA metals from IONPs (Eu-VSOPs) and GBCAs (Gd-BOPTA) in arterial tissue sections at different stages of atherosclerotic plaque progression. We utilized IHC and elemental microscopy by LA-ICP-MS and SR-μXRF. Our findings showed distinct atherosclerotic plaque tissue distributions of Eu-VSOPs and Gd, which are determined by the ECM composition. Eu signal intensity and Fe concentration in the arterial wall correlated with plaque progression, suggesting the feasibility of Eu-VSOPs in monitoring plaque progression in experimental MRI studies. Importantly, our results suggest that the intimomedial interface is a crucial microenvironment hosting elemental hotspots containing high concentrations of Ca and P, indicating calcifications. These areas are also the hotspots of Gd distribution, which range in size from a few micrometers to submicrometers. This indicates Gd impact on arterial calcification, further investigations of which are crucial for understanding underlying pathological changes leading to vulnerability.

Cells and tissues constantly react to their surroundings by swift adaptations that often take place through dynamic feedback loops within their ECM. In diseases, ECM is altered qualitatively and quantitatively in the form of changes in the biochemical composition, supramolecular organization and intrinsic physicochemical characteristics. These changes are rapidly initiated by transient interactions such as reorganization or neutralization of the charge nature around the molecules, which alter nearby architecture and give rise to hierarchical and stronger interactions, all of which exist at the highly abundant level within the ECM composition. Therefore, it is highly important for further studies to investigate possible mechanisms involving metal dissociation and complexation or influences of the ECM composition on the biodistribution of metal-based CAs in different disease models.

As the first study that compares the microdistribution of iron oxide- and Gd-based MR contrast agents in atherosclerotic plaques, the experimental workflow presented here focused on improving atherosclerotic plaque characterization by providing quantitative findings at high sensitivity and spatial resolution. Thus, this dissertation study serves as an important basis for subsequent MRI studies aiming at advanced characterization of atherosclerotic plaques, depicting changes leading to vulnerable plaques, and ultimately early diagnosis of the disease.

3.6. References

1. Libby Peter, Bornfeldt Karin E, Tall Alan R (2016) Atherosclerosis. Circ Res 118:531–534.
2. Nichols Melanie, Townsend Nick, Scarborough Peter, Rayner Mike (2014) Cardiovascular disease in Europe 2014: epidemiological update. Eur Heart J 35:2950–2959.
3. Heidenreich Paul A, Trogdon Justin G, Khavjou Olga A, Butler Javed, Dracup Kathleen, Ezekowitz Michal D, Finkelstein Eric A, Hong Yuling, Johnston S Claiborne, Khera Amit, Lloyd Jones-Donald M, Nelson Sue A, Nichol Graham, Orenstein Diane, Wilson Peter WF, Woo Y Joseph (2011) Forecasting the Future of Cardiovascular Disease in the United States. Circulation 123:933–944.
4. Mensah George A, Roth Gregory A, Fuster Valentin (2019) The Global Burden of Cardiovascular Diseases and Risk Factors. Journal of the American College of Cardiology 74:2529–2532.
5. Yusuf Salim, Reddy Srinath, Ôunpuu Stephanie, Anand Sonia (2001) Global Burden of Cardiovascular Diseases. Circulation 104:2746–2753.
6. Herrington William, Lacey Ben, Sherliker Paul, Armitage Jane, Lewington Sarah (2016) Epidemiology of Atherosclerosis and the Potential to Reduce the Global Burden of Atherothrombotic Disease. Circ Res 118:535–546.
7. Virmani Renu, Burke Alan P, Farb Andrew, Kolodgie Frank D (2006) Pathology of the Vulnerable Plaque. J Am Coll Cardiol 47:C13–C18.
8. Anderson Todd J, Gerhard Marie D, Meredith Ian T, Charbonneaue Francois, Delagrange Danielle, Creager Mark A, Selwyn Andrew P, Ganz Peter (1995) Systemic nature of endothelial dysfunction in atherosclerosis. The American Journal of Cardiology 75:71B-74B.
9. Ross Russell, Glomset John A (1973) Atherosclerosis and the Arterial Smooth Muscle Cell. Science 180:1332–1339.

10. Ross Russell, Glomset John A (1976) The Pathogenesis of Atherosclerosis: (First of Two Parts). N Engl J Med 295:369–377.
11. Chatzizisis Yiannis S, Jonas Michael, Coskun Ahmet U, Beigel Roy, Stone Benjamin V, Maynard Charles, Gerrity Ross G, Daley William, Rogers Campell, Edelman Elazer R, Feldman Charles L, Stone Peter H (2008) Prediction of the Localization of High-Risk Coronary Atherosclerotic Plaques on the Basis of Low Endothelial Shear Stress: An Intravascular Ultrasound and Histopathology Natural History Study. Circulation 117:993–1002.
12. Vogiatzi Georgia, Tousoulis Dimitris, Stefanadis Christodoulos (2009) The role of oxidative stress in atherosclerosis. Hellenic J Cardiol. 2009 Sep-Oct;50(5):402-9.
13. Lakshmi SV Vijaya, Padmaja G, Kuppusamy Periannan, Kutala Vijay Kumar (2009) Oxidative Stress in Cardiovascular Disease. IJBB Vol46(6) [December 2009]
14. Rader Daniel J, Daugherty Alan (2008) Translating molecular discoveries into new therapies for atherosclerosis. Nature 451:904–913.
15. Wight Thomas N, Merrilees Mervyn J (2004) Proteoglycans in Atherosclerosis and Restenosis: Key Roles for Versican. Circulation Research 94:1158–1167.
16. Ballinger ML, Nigro J, Frontanilla KV, Dart AM, Little PJ (2004) Regulation of glycosaminoglycan structure and atherogenesis. Cellular and Molecular Life Sciences (CMLS) 61:1296–1306.
17. Bobik Alex, Agrotis Alex, Kanellakis Peter, Dilley Rodney, Krushinsky Anatoly, Smirnov Vladimir, Tararak Eduard, Condron Melanie, Kostolias Gina (1999) Distinct Patterns of Transforming Growth Factor-β Isoform and Receptor Expression in Human Atherosclerotic Lesions. Circulation 99:2883–2891.
18. Tabas Ira, García-Cardeña Guillermo, Owens Gary K (2015) Recent insights into the cellular biology of atherosclerosis. J Cell Biol 209:13–22.

19. Gerhardt Teresa, Ley Klaus (2015) Monocyte trafficking across the vessel wall. Cardiovasc Res 107:321–330.
20. Gimbrone Michael A., García-Cardeña Guillermo (2016) Endothelial Cell Dysfunction and the Pathobiology of Atherosclerosis. Circ Res 118:620–636.
21. Ross Russel (1999) Atherosclerosis—an inflammatory disease. New England journal of medicine 340:115–126
22. Sakakura Kenichi, Nakano Masataka, Otsuka Fumiyuki, Ladich Elena, Kolodgie Frank D, Virmani Renu (2013) Pathophysiology of Atherosclerosis Plaque Progression. Heart Lung Circ 22:399–411.
23. Libby Peter (2008) The molecular mechanisms of the thrombotic complications of atherosclerosis. J Intern Med 263:517–527.
24. Uca Yavuz Oguz, Taupitz Matthias (2020) Glycosaminoglycans as Novel Targets for in vivo Contrast- Enhanced Magnetic Resonance Imaging of Atherosclerosis. J Cardiol Cardiovasc Med 5:9
25. Lairez Oliver, Fayad Zahi A (2013) Imaging of atherosclerosis: Can molecular imaging do more? Arch Cardiovasc Dis 106:551–553.
26. Tarkin Jason M., Dweck Marc R, Evans Nicholas R, Richard Takx AP, Brown Adam J, Tawakol Ahmed, Fayad Zahi A, Rudd James HF (2016) Imaging Atherosclerosis. Circ Res 118:750–769.
27. Stone Gregg W, Maehara Akiko, Lansky Alexandra J, de Bruyne Bernard, Cristea Ecaterina, Mintz Gary S, Mehran Roxana, McPherson John, Farhat Naim, Marso Steven P, Parise Helen, Templin Barry, White Roseann, Zhang Zhen, Serruys Patrick W (2011) A Prospective Natural-History Study of Coronary Atherosclerosis. N Engl J Med 364:226–235.
28. Tearney Guillermo J, Regar Evelyn, Akasaka Takashi, Adriaenssens Tom, Barlis Peter, Berezza Hiram G, Bouma Brett, Bruining Nico, Cho Jin-man, Chowdhary Saqib, Costa

Marco A, de Silva Ranil, Dijkstra Jouke, Di Mario Carlo, Dudeck Darius, Falk Erlin, Feldman Marc D, Fitzgerald Peter, Garcia Hector, Gonzalo Nieves, Granada Juan F, Guagliumi Giulio, Holm Niels R, Honda Yasuhiro, Ikeno Fumiaki, Kawasaki Masaroni, Kochman Janusz, Koltowski Lukasz, Kubo Takashi, Kume Teruyoshi, Kyono Hiroyuki, Lam Cheung Chi Simon, Lamouche Guy, Lee David P, Leon Martin B, Maehara Akiko, Manfrini Olivia, Mintz Gary S, Mizuno Kyiouchi, Morel Marie-angele, Nadkarni Seemantini, Okura Hiroyuki, Otake Hiromasa, Pietrasik Arkadiusz, Prati Francesco, Raeber Lorenz, Radu Maria D, Rieber Johannes, Riga Maria, Rollins Andrew, Rosenberg Mireille, Sirbu Vasile, Serruys Patrick WJC, Shimada Kanei, Shinke Toshiro, Shite Junya, Siegel Eliot, Sonada Shinjo, Sute Melissa, Takarada Shigeho, Tanaka Atsushi, Terashima Mitsuyasu, Troels Tim, Uemura Shiro, Ughi Giovanni J, van Beusekom Heleen MM, van der Steen Antonius FW, van Es Gerrit-Ann, van Soest Gijs, Virmani Renu, Waxman Sergio, Weissman Neil J, Weisz Giora (2012) Consensus Standards for Acquisition, Measurement, and Reporting of Intravascular Optical Coherence Tomography Studies: A Report From the International Working Group for Intravascular Optical Coherence Tomography Standardization and Validation. J Am Coll Cardiol 59:1058–1072.

29. Kilic Ismail Dogu, Caiazzo Gianluca, Fabris Enrico, Serdoz Roberta, Abou-Sherif Sara, Madden Sean, Moreno Pedro R, Goldstein James, Di Mario Carlo (2015) Near-infrared spectroscopy-intravascular ultrasound: scientific basis and clinical applications. Eur Heart J - Cardiovasc Imaging 16:1299–1306.
30. Voros Szilard, Rinehart Sarah, Qian Zhen, Joshi Parag, Vaquez Gustavo, Fischer Collin, Belur Pallavi, Hulten Edward, Villines Todd C (2011) Coronary Atherosclerosis Imaging by Coronary CT Angiography: Current Status, Correlation With Intravascular Interrogation and Meta-Analysis. JACC Cardiovasc Imaging 4:537–548.
31. Skagen Karolina, Johnsrud Kjersti, Evensen Kristin, Scott Helge, Krohg-Sorensen Kirsten, Reier-Nielsen Frode, Revheim Mona-Elisabeth, Fjeld Gunnar Jan, Skjelland Mona, Russel

David (2015) Carotid Plaque Inflammation Assessed with ^{18} F-FDG PET/CT is Higher in Symptomatic Compared with Asymptomatic Patients. Int J Stroke 10:730–736.

32. Winkel Leah CJ, Groen Harald C, van Thiel Bibi S, Mueller Cristina, van der Steen Antonius FW, Wentzel Jolanda J, de Jong Marion, van der Heiden Kim (2014) Folate Receptor–Targeted Single-Photon Emission Computed Tomography/Computed Tomography to Detect Activated Macrophages in Atherosclerosis: Can It Distinguish Vulnerable from Stable Atherosclerotic Plaques? Mol Imaging 13:7290.2013.00061.
33. Libby Peter, Ridker Paul M, Hansson Goeran K (2011) Progress and challenges in translating the biology of atherosclerosis. Nature 473:317–325.
34. Bender Yvonne Y, Pfeifer Andreas, Ebersberger Hans U, Diederichs Gerd, Hoppe Peter, Hamm Bernd, Botnar Rene M, Makowski Marcus (2016) Molecular Cardiovascular Magnetic Resonance: Current Status and Future Prospects. Curr Cardiol Rep 18:47.
35. Corti Roberto, Fuster Valentin (2011) Imaging of atherosclerosis: magnetic resonance imaging. Eur Heart J 32:1709–1719.
36. Caravan Peter, Ellison Jeffrey J, McMurry Thomas J, Lauffer Randall B (1999) Gadolinium(III) Chelates as MRI Contrast Agents: Structure, Dynamics, and Applications. Chem Rev 99:2293–2352.
37. Caravan P (2006) Strategies for increasing the sensitivity of gadolinium based MRI contrast agents. Chem Soc Rev 35:512.
38. Spuentrup Elmar, Botnar Rene M, Wiethoff Andrea J, Ibrahim Tareq, Kelle Sebastian, Katoh Marcus, Ozgun Murat, Nael Eike, Vymazal Josef, Graham Phil B, Gunther Rolf W, Maintz David (2008) MR imaging of thrombi using EP-2104R, a fibrin-specific contrast agent: initial results in patients. Eur Radiol 18:1995–2005.
39. Makowski Marcus R, Wiethoff Andrea J, Blume Ulrike, Cuello Friederike, Warley Alice, Jansen Christian HP, Nagel Eike, Razavi Reza, Onthank David C, Cesati Richard R, Marber Michael S, Schaeffter Tobias, Smith Alberto, Robinson Simon P, Botnar Rene M (2011)

Assessment of atherosclerotic plaque burden with an elastin-specific magnetic resonance contrast agent. Nat Med 17:383–388.

40. Stolzenburg Nicola, Breinl Janni, Wagner Susanne, Uca Yavuz Oguz, Taupitz Matthias, Hamm Bernd, Schnorr Joerg (2020) Contrast-enhanced MR Imaging of Experimental Atherosclerosis: Interrelationship between Late Gadolinium Enhancement and Histologic Markers of Atherosclerotic Plaque Progression in Rabbits. Atherosclerosis, (*in preparation)*
41. Grobner Thomas (2006) Gadolinium – a specific trigger for the development of nephrogenic fibrosing dermopathy and nephrogenic systemic fibrosis? Nephrol Dial Transplant 21:1104–1108.
42. Ortega Richard, Devès Guillaume, Carmona Asuncion (2009) Bio-metals imaging and speciation in cells using proton and synchrotron radiation X-ray microspectroscopy. J R Soc Interface 6:S649–S658.
43. Fingerhut Stefanie, Niehoff Ann-Christin, Sperling Michael, Jeibmann Astrid, Paulus Werner, Niederstadt Thomas, Allkemper Thomas, Heindel Walter, Holling Markus, Karst Uwe (2018) Spatially resolved quantification of gadolinium deposited in the brain of a patient treated with gadolinium-based contrast agents. J Trace Elem Med Biol 45:125–130.
44. McDonald Robert J, McDonald Jennifer S, Kallmes David F, Jentoft Mark, Murray David, Thielen Kent, Williamson Eric, Eckel Laurence (2015) Intracranial Gadolinium Deposition after Contrast-enhanced MR Imaging. Radiology 275:772–782.
45. Kanda Tomonori, Ishii Kazunari, Kawaguchi Hiroki, Kitajima Kazuhiro, Takenaka Daisuke (2014) High Signal Intensity in the Dentate Nucleus and Globus Pallidus on Unenhanced T1-weighted MR Images: Relationship with Increasing Cumulative Dose of a Gadolinium-based Contrast Material. Radiology 270:834–841.
46. Errante Yuri, Cirimele Vincenzo, Mallio Carlo Augusto, Di Lazzaro Vincenzo, Zobel Bruno Beomonte, Quattrochi Carlo Cosimo (2014) Progressive Increase of T1 Signal Intensity of the Dentate Nucleus on Unenhanced Magnetic Resonance Images Is Associated

With Cumulative Doses of Intravenously Administered Gadodiamide in Patients With Normal Renal Function, Suggesting Dechelation: Investigative Radiology 49:685–690.

47. Laurent S, Vander Elst L, Henoumont C, Muller RN (2010) How to measure the transmetallation of a gadolinium complex. Contrast Media Mol Imaging 5:305–308.
48. Taupitz Matthias, Stolzenburg Nicola, Ebert Monika, Schnorr Joerg, Hauptmann Ralf, Kratz Harald, Hamm Bernd, Wagner Susanne (2013) Gadolinium-containing magnetic resonance contrast media: investigation on the possible transchelation of Gd 3+ to the glycosaminoglycan heparin: GdCM, Glycosaminoglycans and Transchelation. Contrast Media Mol Imaging 8:108–116.
49. Becker J Sabine, Breuer Uwe, Hsieh Hui-Feng, Osterholt Tobias, Kumtabtim Usarat, Wu Bei, Matusch Andreas, Caruso Joseph A, Qin Zhenyu (2010) Bioimaging of Metals and Biomolecules in Mouse Heart by Laser Ablation Inductively Coupled Plasma Mass Spectrometry and Secondary Ion Mass Spectrometry. Anal Chem 82:9528–9533.
50. Tang Tjun Y, Muller Karin H, Graves Martin J, Li Zhi Y, Walsh Stewart R, Young Victoria, Sadat Omar, Howarth Simon PS, Gillard JH (2009) Iron Oxide Particles for Atheroma Imaging. Arterioscler Thromb Vasc Biol 29:1001–1008.
51. Trivedi Rikin A, Mallawarachi Chinthake, U-King-Im Jean-Marie, Graves Martin J, Brown Andrew, Wang Liqun, Kirkpatrick Peter J, Brown John, Gillard Jonathan H (2006) Identifying Inflamed Carotid Plaques Using In Vivo USPIO-Enhanced MR Imaging to Label Plaque Macrophages. Arterioscler Thromb Vasc Biol 26:1601–1606.
52. Sadat Umar, Usman Ammara, Gillard Jonathan H (2017) Imaging pathobiology of carotid atherosclerosis with ultrasmall superparamagnetic particles of iron oxide: an update. Curr Opin Cardiol 32:437–440.
53. Kooi ME, Cappendijk VC, Cleutjens KBJM, Kitslaar PJHEM, Borgers M, Frederik PM, Daemen MJAP, van Engelshoven JMA (2003) Accumulation of Ultrasmall

Superparamagnetic Particles of Iron Oxide in Human Atherosclerotic Plaques Can Be Detected by In Vivo Magnetic Resonance Imaging. Circulation 107:2453–2458.

54. Nahrendorf Matthias, Jaffer Fraouc A, Kelly Kimberley A, Sosnovik D E, Aikawa Elena, Libby Peter, Weissleder Ralph (2006) Noninvasive Vascular Cell Adhesion Molecule-1 Imaging Identifies Inflammatory Activation of Cells in Atherosclerosis. Circulation 114:1504–1511.
55. Michalska Marta, Machtoub Lina, Manthey Helga D, Bauer Elisabeth, Herold Volker, Krohne Georg, Lykowsky Gunthard, Hildenbrand Markus, Kampf Thomas, Jakob Peter, Zernecke Alma, Bauer Wolfgang R (2012) Visualization of Vascular Inflammation in the Atherosclerotic Mouse by Ultrasmall Superparamagnetic Iron Oxide Vascular Cell Adhesion Molecule-1–Specific Nanoparticles. Arterioscler Thromb Vasc Biol 32:2350–2357.
56. Hyafil Fabien, Vucic Esad, Cornily Jean-Cristophe, Sharma Raul, Amirbekian Vardan, Blackwell Francis, Lancelot Eric, Carot Claire, Fuster Valentin, Galis Zorina S, Feldman Laurent J, Fayad Zahi A (2011) Monitoring of arterial wall remodelling in atherosclerotic rabbits with a magnetic resonance imaging contrast agent binding to matrix metalloproteinases. Eur Heart J 32:1561–1571.
57. Kolodgie Frank D, Petrov Artio,, Virmani Renu, Narula, Navneet, Verjans Johan W, Weber Deena K, Hartung Dagmar, Steinmetz Neil, Vanderheyden Jean Luc, Vannan Mani A, Gold Herman K, Reutelingsperger Chris PM, Hofstra Leo, Narula Jagat (2003) Targeting of Apoptotic Macrophages and Experimental Atheroma With Radiolabeled Annexin V: A Technique With Potential for Noninvasive Imaging of Vulnerable Plaque. Circulation 108:3134–3139.
58. Ludwig Antje, Poller Wolfram C, Westphal Kera, Minkwitz Susann, Laettig-Tuenneman Gisela, Metzkow Susanne, Stangl Karl, Baumann Gert, Taupitz Matthias, Wagner Susanne, Schnorr Joerg, Stangl Verena (2013) Rapid binding of electrostatically stabilized iron oxide

nanoparticles to THP-1 monocytic cells via interaction with glycosaminoglycans. Basic Res Cardiol 108:328.

59. Wagner Susanne, Schnorr Joerg, Ludwig Antje, Stangl Verena, Ebert Monika, Hamm Bernd, Taupitz Matthias (2013) Contrast-enhanced MR imaging of atherosclerosis using citrate-coated superparamagnetic iron oxide nanoparticles: calcifying microvesicles as imaging target for plaque characterization. Int J Nanomedicine 8:767–779.
60. Narula Jagat, Virmani Renu, Iskandrian AE (1999) Strategic targeting of atherosclerotic lesions. Journal of Nuclear Cardiology 6:81–90
61. Reimann Carolin, Brangsch Julia, Colletini Federico, Walter Thula, Hamm Bernd, Botnar Rene M, Makowski Marcus R (2017) Molecular imaging of the extracellular matrix in the context of atherosclerosis. Advanced Drug Delivery Reviews 113:49–60.
62. Vakonakis Ionannis, Campbell Iain D (2007) Extracellular matrix: from atomic resolution to ultrastructure. Current Opinion in Cell Biology 19:578–583.
63. Wight Thomas N (1995) The extracellular matrix and atherosclerosis. Current Opinion in Lipidology 6:326
64. Katsuda Shogo, Kaji Toshiyuki (2003) Atherosclerosis and Extracellular Matrix. Journal of Atherosclerosis and Thrombosis 10:267–274.
65. Frantz C, Stewart KM, Weaver Valerie M (2010) The extracellular matrix at a glance. Journal of Cell Science 123:4195–4200.
66. Mouw JK, Ou Guanqing, Weaver Valerie M (2014) Extracellular matrix assembly: a multiscale deconstruction. Nat Rev Mol Cell Biol 15:771–785.
67. Ricard-Blum S, Ruggiero Florence (2005) The collagen superfamily: from the extracellular matrix to the cell membrane. Pathologie Biologie 53:430–442.
68. Galis Zorina S, Khatri Jaikirschan J (2002) Matrix Metalloproteinases in Vascular Remodeling and Atherogenesis. Circulation Research 90:251–262.

69. Rosenbloom Joel, Abrams William R, Mecham Robert (1993) Extracellular matrix 4: The elastic fiber. The FASEB Journal 7:1208–1218.
70. Karnik Satyajit K, Brooke Benjamin S, Bayes-Genis Antonio, Sorensen Lise, Wythe Joshua D, Schwartz Robert S, Keating Mark T, Li Dean Y (2003) A critical role for elastin signalling in vascular morphogenesis and disease. Development 130:411–423.
71. Fuster Valentin, Stein B, Ambrose JA, Badimon L, Badimon JJ, Chesebro JH (1990) Atherosclerotic plaque rupture and thrombosis. Evolving concepts. Circulation 82:II47-59
72. Tavora Fabio, Cresswell Nathaniel, Li Ling, Ripple Mary, Burke Allen (2010) Immunolocalisation of fibrin in coronary atherosclerosis: implications for necrotic core development. Pathology 42:15–22.
73. La Corte Amy L Cilia, Philippou Helen, Ariëns Robert AS (2011) Role of Fibrin Structure in Thrombosis and Vascular Disease. Advances in Protein Chemistry and Structural Biology 83:75–127.
74. Taylor Kristen R, Gallo Richard L (2006) Glycosaminoglycans and their proteoglycans: host-associated molecular patterns for initiation and modulation of inflammation. The FASEB Journal 20:9–22.
75. Carey DJ, Rafferty CM, Todd MS (1987) Effects of inhibition of proteoglycan synthesis on the differentiation of cultured rat Schwann cells. The Journal of Cell Biology 105:1013–1021.
76. Cherchi GM, Coinu R, Demuro P, Formato M, Sanna G, Tidore M, Tira ME, De Luca G (1990) Structural and Functional Modifications of Human Aorta Proteoglycans in Atherosclerosis. Matrix 10:362–372.
77. Kjellén Lena, Lindahl U (1991) Proteoglycans: Structures and Interactions. Annual Review of Biochemistry 60:443–475.

78. Lidholt K, Lindahl Ulf (1992) Biosynthesis of heparin. The D-glucuronosyl- and N-acetyl-D-glucosaminyltransferase reactions and their relation to polymer modification. Biochem J 287:21–29
79. Iozzo Renato V, Murdoch Alan D (1996) Proteoglycans of the extracellular environment: clues from the gene and protein side offer novel perspectives in molecular diversity and function. The FASEB Journal 10:598–614
80. Lander Arthur D (1998) Proteoglycans: master regulators of molecular encounter? Matrix Biology 17:465–472
81. E Karangelis D, Kanakis I, P Asimakopoulou A, Karousou, Passi A, D Theocharis A, Triposkiadi, B Tsilimingas N, K Karamanos Nikos (2010) Glycosaminoglycans as key molecules in atherosclerosis: the role of versican and hyaluronan. Current medicinal chemistry 17:4018–4026
82. Radhakrishnamurthy B, Srinivasan SR, Vijayagopal P, Berenson GS (1990) Arterial wall proteoglycans—biological properties related to pathogenesis of atherosclerosis. European heart journal 11:148–157
83. Cardoso LE, Mourão PA (1994) Glycosaminoglycan fractions from human arteries presenting diverse susceptibilities to atherosclerosis have different binding affinities to plasma LDL. Arteriosclerosis, Thrombosis, and Vascular Biology 14:115–124.
84. Evanko SP, Raines EW, Ross R, Gold LI, Wight TN (1998) Proteoglycan distribution in lesions of atherosclerosis depends on lesion severity, structural characteristics, and the proximity of platelet-derived growth factor and transforming growth factor-beta. Am J Pathol 152:533–546
85. Stephens Elizabeth H, Saltarrelli Jerome G, Baggett L Scott, Nandi Indrajit, Kuo Joyce J, Davis Alan R, Olmsted-Davis Elizabeth A, Reardon Michael J, Grande-Allen Kathryn Jane (2011) Differential proteoglycan and hyaluronan distribution in calcified aortic valves. Cardiovascular Pathology 20:334–342.

86. Parish Christopher R (2006) The role of heparan sulphate in inflammation. Nature Reviews Immunology 6:633–643.
87. Middleton Jim, Patterson Angela M, Gardner Lucy, Schmutz Caroline, Ashton Brian A (2002) Leukocyte extravasation: chemokine transport and presentation by the endothelium. Blood 100:3853–3860.
88. Wagner Dirk, Maser Jörg, Lai Barry, Cai Zhonghou, Barry Clifton E, Höner zu Bentrup Kerstin, Russel David G, Bermudez Luiz E (2005) Elemental Analysis of *Mycobacterium avium* -, *Mycobacterium tuberculosis* -, and *Mycobacterium smegmatis* -Containing Phagosomes Indicates Pathogen-Induced Microenvironments within the Host Cell's Endosomal System. J Immunol 174:1491–1500.
89. Becker J Sabine, Matusch Andreas, Wu Bei (2014) Bioimaging mass spectrometry of trace elements – recent advance and applications of LA-ICP-MS: A review. Anal Chim Acta 835:1–18.
90. Acquadro Elena, Cabella Claudia, Ghiani Simona, Miragoli Luigi, Bucci Enrico M, Corpillo Davide (2009) Matrix-Assisted Laser Desorption Ionization Imaging Mass Spectrometry Detection of a Magnetic Resonance Imaging Contrast Agent in Mouse Liver. Anal Chem 81:2779–2784.
91. Cruz-Alonso Maria, Lores-Padín Ana, Valencia Eva, Gonzales-Iglesias Hektor, Fernandez Beatriz, Pereiro Rosario (2019) Quantitative mapping of specific proteins in biological tissues by laser ablation–ICP-MS using exogenous labels: aspects to be considered. Anal Bioanal Chem 411:549–558.
92. Pugh JAT, Cox AG, McLeod CW, Bunch J, Writer MJ, Hart SL, Bienemann A, White E, Bell J (2012) Elemental imaging of MRI contrast agents: benchmarking of LA-ICP-MS to MRI. Anal Bioanal Chem 403:1641–1649.

93. Paunesku Tatjana, Vogt Stefan, Maser Jörg, Lai Barry, Woloschak Gayle (2006) X-ray fluorescence microprobe imaging in biology and medicine. Journal of Cellular Biochemistry 99:1489–1502.
94. Thakral Charu, Abraham Jerrold L (2007) Automated Scanning Electron Microscopy and X-Ray Microanalysis for in situ Quantification of Gadolinium Deposits in Skin. J Electron Microsc (Tokyo) 56:181–187.
95. Gramaccioni Chiara, Yang Yang, Procopio Alessandra, Pacureanu Alexandra, Bohic Sylvain, Malucelli Emil, Lotti Stefano, Farruggia Giovanna, Bukreeva Inna, Notargiacomo Andrea, Fratini Michaela, Valenti Piera, Rosa Luigi, Berlutti Francesca, Cloetens Peter, Lagomarsino Stefano (2018) Nanoscale quantification of intracellular element concentration by X-ray fluorescence microscopy combined with X-ray phase contrast nanotomography. Appl Phys Lett 112:053701.
96. Uca Yavuz Oguz, Hallmann David, Hesse Bernhard, Seim Christian, StolzenburgNicola, Pietsch Hubertus, Schnorr Joerg, Taupitz Matthias (2020) Microdistribution of Magnetic Resonance Imaging Contrast Agents in Atherosclerotic Plaques Determined by LA-ICP-MS and SR-µXRF Imaging. Mol Imaging Biol, 1860-2002
97. de Schellenberger Angela Ariza, Hauptmann Ralf, Millward Jason M, Schellenberger Eyk, Kobayashi Yuske, Taupitz Matthias, Infante-Duarte Carmen, Schnorr Joerg, Wagner Susanne (2017) Synthesis of europium-doped VSOP, customized enhancer solution and improved microscopy fluorescence methodology for unambiguous histological detection. J Nanobiotechnology 15:71.
98. Veronesi G, Deniaud A, Gallon T, Jouneau PH, Villanova J, Delangle P. Carriere M, Kieffer I, Charbonnier P, Michaud=Soret I (2016) Visualization, quantification and coordination of Ag + ions released from silver nanoparticles in hepatocytes. Nanoscale 8:17012–17021.

99. Peters Sanne AE, Ruijter Hester M den, Bots Michiel L, Moons Karel GM (2012) Improvements in risk stratification for the occurrence of cardiovascular disease by imaging subclinical atherosclerosis: a systematic review. Heart 98:177–184.

100. Shaw Stanley Y (2009) Molecular imaging in cardiovascular disease: targets and opportunities. Nat Rev Cardiol 6:569–579.

101. Wu Joseph C, Bengel Frank M, Gambhir Sanjiv S (2007) Cardiovascular Molecular Imaging. Radiology 244:337–355.

102. Lindner Jonathan R (2009) Molecular imaging of cardiovascular disease with contrast-enhanced ultrasonography. Nat Rev Cardiol 6:475–481.

103. Jaffer Farouc A, Libby Peter, Weissleder Ralf (2007) Molecular Imaging of Cardiovascular Disease. Circulation 116:1052–1061

104. Jaffer Farouc A, Libby Peter, Weissleder Ralf (2006) Molecular and Cellular Imaging of Atherosclerosis: Emerging Applications. Journal of the American College of Cardiology 47:1328–1338.

105. Phinikaridou Alkystis, Andia Marcelo E, Protti Andrea, Indermuehle Andreas, Shah Ajay, Smith Alberto, Warley Alice, Botnar Rene M (2012) Noninvasive Magnetic Resonance Imaging Evaluation of Endothelial Permeability in Murine Atherosclerosis Using an Albumin-Binding Contrast Agent. Circulation 126:707–719.

106. Yuan Chun, Mitsumori Lee M, Ferguson Marina S, Polissar Nayak L, Echelard Denise, Ortiz Geraldo, Small Randy, Davies Joseph W, Kerwin William S, Hatsukami Thomas S (2001) In Vivo Accuracy of Multispectral Magnetic Resonance Imaging for Identifying Lipid-Rich Necrotic Cores and Intraplaque Hemorrhage in Advanced Human Carotid Plaques. Circulation 104:2051–2056.

107. Meding Joerg, Urich Matthias, Licha Kai, Reinhardt Michael, Misselwitz Bernd, Fayad Zahi A, Winmann Hanns-Joachim (2007) Magnetic resonance imaging of atherosclerosis

by targeting extracellular matrix deposition with Gadofluorine M. Contrast Media & Molecular Imaging 2:120–129.

108. Kobayashi Yuske, Hauptmann Ralf, Kratz Harald, Ebert Monika, Wagner Susanne, Taupitz Matthias (2017) Europium doping of superparamagnetic iron oxide nanoparticles enables their detection by fluorescence microscopy and for quantitative analytics. Technol Health Care 25:457–470.

109. Poller Wolfram C, Pieber Melanie, Boehm-Sturm Philipp, Ramberger Evelyn, Karampelas, Vasileios, Moeller Konstantin, Schleicher Moritz, Wiekhorst Frank, Loewa Norbert, Wagner Susanne, Schnorr Jörg, Taupitz Matthias, Stangl Karl, Stangl Verena, Ludwig Antje (2018) Very small superparamagnetic iron oxide nanoparticles: Long-term fate and metabolic processing in atherosclerotic mice. Nanomedicine Nanotechnol Biol Med 14:2575–2586.

110. Poller Wolfram C, Ramberger Evelyn, Boehm-Sturm Philipp, Mueller Susanne, Moeller Konstantin, Loewa Norbert, Wiekhorst Frank, Wagner Susanne, Taupitz Matthias, Schellenberger Eyk, Baumann Gert, Stangl Karl, Stangl Verena, Ludwig Antje (2016) Uptake of citrate-coated iron oxide nanoparticles into atherosclerotic lesions in mice occurs via accelerated transcytosis through plaque endothelial cells. Nano Res 9:3437–3452.

111. O'Halloran Thomas V, Culotta Valeria Cizewski (2000) Metallochaperones, an Intracellular Shuttle Service for Metal Ions. J Biol Chem 275:25057–25060.

112. Wiener E, Settles M, Weirich G, Schmidt C, Diederichs G (2011) The Influence of Collagen Network Integrity on the Accumulation of Gadolinium-Based MR Contrast Agents in Articular Cartilage. RöFo - Fortschritte Auf Dem Geb Röntgenstrahlen Bildgeb Verfahr 183:226–232.

113. Lindahl U, Hook Magnus (1978) Glycosaminoglycans and their binding to biological macromolecules. Annu Rev Biochem 47:385–417

114. Limuro Yuji, Yamamoto Masayuki, Kohno Hiroshi, Itakura Jun, Fuji Hideki, Matsumoto Yoshiro (1994) Blockade of liver macrophages by gadolinium chloride reduces lethality in endotoxemic rats—analysis of mechanisms of lethality in endotoxemia. J Leukoc Biol 55:723–728.

115. Weng Te-I, Chen Huang Jen, Lu Chen-Wen, Ho Yu-Chin, Wu Lia-Lun, Liu Shing-Hwa, Hsiao Jong-Kai (2018) Exposure of Macrophages to Low-Dose Gadolinium-Based Contrast Medium: Impact on Oxidative Stress and Cytokines Production. Contrast Media Mol Imaging 2018:3535769.

116. Reynolds Joanne L, Joannides Alexis J, Skepper Jeremy N, McNair Rosamund, Schurgers Leon J, Proutfoot Diane, Jahnen-Dechent Willi, Weissberg Peter L, Shanahan Catherine M (2004) Human Vascular Smooth Muscle Cells Undergo Vesicle-Mediated Calcification in Response to Changes in Extracellular Calcium and Phosphate Concentrations: A Potential Mechanism for Accelerated Vascular Calcification in ESRD. J Am Soc Nephrol 15:2857–2867.

117. Proudfoot Diane, Shanahan Catherine M (2001) Biology of Calcification in Vascular Cells: Intima versus Media. Herz 26:245–251.

118. Hirsch D, Azoury R, Sarig S, Kruth HS (1993) Colocalization of cholesterol and hydroxyapatite in human atherosclerotic lesions. Calcif Tissue Int 52:94–98.

119. Wang YH, Liu Y, Maye P, Rowe DW (2006) Examination of Mineralized Nodule Formation in Living Osteoblastic Cultures Using Fluorescent Dyes. Biotechnol Prog 22:1697–1701.

120. Bobryshev YV, Lord RSA, Warren BA (1995) Calcified deposit formation in intimal thickenings of the human aorta. Atherosclerosis 118:9–21.

121. Bobryshev YV (2005) Calcification of elastic fibers in human atherosclerotic plaque. Atherosclerosis 180:293–303.

122. Jacobi Angela, Ariza de Schellenberger Angela, Uca Yavuz Oguz, Herbig Maik, Guck Jochen, Sack Ingolf (2021) Real-Time Deformability Cytometry Detects Leukocyte Stiffening After Gadolinium-Based Contrast Agent Exposure. Investigative Radiology Publish Ahead of Print:

123. Tweedle MF, Wedeking P, Kumar K (1995) Biodistribution of radiolabeled, formulated gadopentetate, gadoteridol, gadoterate, and gadodiamide in mice and rats. Invest Radiol 30:372–380.

124. Di Gregorio Enza, Furlan Chiara, Atlante Sandra, Stefania Rachele, Gianolio Eliana, Aime Silvio (2020) Gadolinium Retention in Erythrocytes and Leukocytes From Human and Murine Blood Upon Treatment With Gadolinium-Based Contrast Agents for Magnetic Resonance Imaging. Investigative Radiology 55:30–37.

4. Statutory Declaration

“I, Yavuz O., Uca, by personally signing this document in lieu of an oath, hereby affirm that I prepared the submitted dissertation on the topic: Metal-based Contrast Agents for Magnetic Resonance Imaging: Distribution in Atherosclerotic Plaques Analyzed by Elemental Microscopy (Metallbasierte Kontrastmittel für die Magnetresonanztomographie: Untersuchungen zur deren Verteilung in Atherosklerotischen Plaques mittels Elementmikroskopie), independently and without the support of third parties, and that I used no other sources and aids than those stated.

All parts which are based on the publications or presentations of other authors, either in letter or in spirit, are specified as such in accordance with the citing guidelines. The sections on methodology (in particular regarding practical work, laboratory regulations, statistical processing) and results (in particular regarding figures, charts and tables) are exclusively my responsibility.

Furthermore, I declare that I have correctly specified all of the data, the analyses, and the conclusions generated from data obtained in collaboration with other persons, and that I have correctly identified my own contribution and the contributions of other persons (cf. declaration of contribution). I have correctly marked all texts or parts of texts that were generated in collaboration with other persons.

My contributions to any publications to this dissertation correspond to those stated in the below joint declaration made together with the supervisor. All publications created within the scope of the dissertation comply with the guidelines of the ICMJE (International Committee of Medical Journal Editors; www.icmje.org) on authorship. In addition, I declare that I complied with the regulations of Charité – Universitätsmedizin Berlin for ensuring good scientific practice.

I declare that I have not yet submitted this dissertation in identical or similar form to another Faculty.

The significance of this statutory declaration and the consequences of a false statutory declaration under criminal law (Sections 156, 161 of the German Criminal Code) are known to me.”

Date 03.03.2021 Signature

5. Declaration of own contribution to the top-journal publication for a PhD degree

Yavuz O. Uca contributed as **the sole first author** to the publication listed below:

Publication: Uca YO, Hallmann D, Hesse B, Seim C, Stolzenburg N, Pietsch H, Schnorr J, Taupitz M, Microdistribution of Magnetic Resonance Imaging Contrast Agents in Atherosclerotic Plaques Determined by LA-ICP-MS and SR-µXRF Imaging. Mol Imaging Biol, 2020

Contribution:

- **Theme, Idea, Concept:** (Uca, Schnorr, Taupitz) – The general framework of the dissertation was initially proposed by Taupitz and Schnorr. Uca formulated the idea thematically, and formulated the concept of the publication structurally.

- **Manuscript writing:** (Uca) was the **sole first author** as well as the **corresponding author**. Uca prepared all the figures and the tables, wrote the complete manuscript and the electronic supplementary material. Uca edited the manuscript with the feedback of the co-authors, and undertook the communication and revisions with the journal. Electronic supplementary material of the original publication was added to the dissertation file.

- **Development of the hypothesis:** (Uca, Taupitz) – The hypothesis was initially proposed by Taupitz et. al. Uca investigated the hypothesis by means of high-sensitivity and high spatial resolution imaging. Data interpretation, scientific discussions and conclusions are own contribution, which were supported by the feedback of co-authors.

- **Experimental work, data collection:** (Uca, Hallmann, Hesse) – Uca carried out the experimental work with the support of Hallman and Hesse.

- **Method development**: (Uca, Taupitz, Schnorr) – Methodology was formed by Uca, Taupitz and Schnorr. Uca developed the methods further with respect to observations made and scientific questions raised during the course of the research project.

- **Data/Image processing, evaluation and visualization:** (Uca, Hallmann, Hesse) – Uca performed data processing with the support of Hallmann and Hesse. Uca carried out data evaluation, statistical analysis, data visualization and presentation.

- **Research Funding and Grants**: (Taupitz, Schnorr)

_____

Signature, date and stamp of first supervising university professor / lecturer

_____

Signature of doctoral candidate

6. Original Publication

Uca YO, Hallmann D, Hesse B, Seim C, Stolzenburg N, Pietsch H, Schnorr J, Taupitz M, Microdistribution of Magnetic Resonance Imaging Contrast Agents in Atherosclerotic Plaques Determined by LA-ICP-MS and SR-µXRF Imaging. Mol Imaging Biol, 2020

https://doi.org/10.1007/s11307-020-01563-z

7. Journal Summary List

Journal Data Filtered By: **Selected JCR Year: 2018** Selected Editions: SCIE,SSCI
Selected Categories: **"RADIOLOGY, NUCLEAR MEDICINE and MEDICAL IMAGING"** Selected Category Scheme: WoS
Gesamtanzahl: 129 Journale

Rank	Full Journal Title	Total Cites	Journal Impact Factor	Eigenfactor Score
1	JACC-Cardiovascular Imaging	8,801	10.975	0.026160
2	MEDICAL IMAGE ANALYSIS	7,694	8.880	0.013370
3	IEEE TRANSACTIONS ON MEDICAL IMAGING	19,545	7.816	0.024990
4	RADIOLOGY	54,641	7.608	0.061300
5	JOURNAL OF NUCLEAR MEDICINE	27,551	7.354	0.037990
6	EUROPEAN JOURNAL OF NUCLEAR MEDICINE AND MOLECULAR IMAGING	15,406	7.182	0.024760
7	CLINICAL NUCLEAR MEDICINE	4,922	6.498	0.007680
8	INTERNATIONAL JOURNAL OF RADIATION ONCOLOGY BIOLOGY PHYSICS	45,833	6.203	0.046810
9	INVESTIGATIVE RADIOLOGY	6,563	6.091	0.011150
10	Circulation-Cardiovascular Imaging	5,456	5.813	0.018480
11	NEUROIMAGE	99,720	5.812	0.132720
12	ULTRASOUND IN OBSTETRICS & GYNECOLOGY	12,336	5.595	0.020140
13	European Heart Journal-Cardiovascular Imaging	5,498	5.260	0.021650
14	RADIOTHERAPY AND ONCOLOGY	17,873	5.252	0.027470
15	Photoacoustics	512	5.250	0.001330
16	JOURNAL OF CARDIOVASCULAR MAGNETIC RESONANCE	5,113	5.070	0.014020
17	ULTRASCHALL IN DER MEDIZIN	2,238	4.613	0.003700
18	HUMAN BRAIN MAPPING	22,040	4.554	0.043230
19	JOURNAL OF NUCLEAR CARDIOLOGY	3,711	4.112	0.004480
20	EUROPEAN RADIOLOGY	19,597	3.962	0.033870

Rank	Full Journal Title	Total Cites	Journal Impact Factor	Eigenfactor Score
21	RADIOGRAPHICS	11,768	3.923	0.009170
22	Biomedical Optics Express	9,547	3.910	0.021750
23	MAGNETIC RESONANCE IN MEDICINE	32,648	3.858	0.034990
24	SEMINARS IN NUCLEAR MEDICINE	2,245	3.798	0.002710
25	Journal of the American College of Radiology	4,191	3.785	0.009760
26	JOURNAL OF MAGNETIC RESONANCE IMAGING	17,147	3.732	0.027800
27	KOREAN JOURNAL OF RADIOLOGY	2,687	3.730	0.004800
28	INTERNATIONAL JOURNAL OF HYPERTHERMIA	3,552	3.589	0.004020
29	EJNMMI Physics	394	3.475	0.001350
30	NMR IN BIOMEDICINE	7,511	3.414	0.014790
31	MOLECULAR IMAGING AND BIOLOGY	2,543	3.341	0.005360
32	Journal of Cardiovascular Computed Tomography	1,711	3.316	0.004430
33	COMPUTERIZED MEDICAL IMAGING AND GRAPHICS	2,464	3.298	0.002990
34	AMERICAN JOURNAL OF NEURORADIOLOGY	23,231	3.256	0.028010
35	MEDICAL PHYSICS	26,715	3.177	0.030870
36	AMERICAN JOURNAL OF ROENTGENOLOGY	33,633	3.161	0.028540
37	CANCER IMAGING	1,406	3.153	0.002220
38	Quantitative Imaging in Medicine and Surgery	1,072	3.074	0.002420
39	PHYSICS IN MEDICINE AND BIOLOGY	27,458	3.030	0.031970
40	EJNMMI Research	1,408	3.000	0.004320
41	EUROPEAN JOURNAL OF RADIOLOGY	12,871	2.948	0.019480
42	Radiation Oncology	5,669	2.895	0.012980

MOLECULAR IMAGING AND BIOLOGY

Mol Imaging Biol (2020)
DOI: 10.1007/s11307-020-01563-z

WMIS World Molecular Imaging Society
esmi European Society for Molecular Imaging

RESEARCH ARTICLE

Microdistribution of Magnetic Resonance Imaging Contrast Agents in Atherosclerotic Plaques Determined by LA-ICP-MS and SR-μXRF Imaging

Yavuz Oguz Uca,[1] David Hallmann,[2] Bernhard Hesse,[3,4] Christian Seim,[3,5] Nicola Stolzenburg,[1] Hubertus Pietsch,[2] Jörg Schnorr,[1] Matthias Taupitz[1]

[1]*Charité - Universitätsmedizin Berlin, corporate member of Freie Universität Berlin, Humboldt-Universität zu Berlin, and Berlin Institute of Health, Charitéplatz 1, 10117, Berlin, Germany*
[2]*MR and CT Contrast Media Research, Bayer AG, Berlin, Germany*
[3]*Xploraytion GmbH, Berlin, Germany*
[4]*European Synchrotron Radiation Facility (ESRF), Grenoble, France*
[5]*Technische Universität Berlin, Berlin, Germany*

Abstract

Purpose: Contrast-enhanced magnetic resonance imaging (MRI) has the potential to replace angiographic evaluation of atherosclerosis. While studies have investigated contrast agent (CA) uptake in atherosclerotic plaques, exact CA spatial distribution on a microscale is elusive. The purpose of this study was to investigate the microdistribution of gadolinium (Gd)- and iron (Fe) oxide-based CA in atherosclerotic plaques of New Zealand White rabbits.

Procedures: The study was performed as a *post hoc* analysis of archived tissue specimens obtained in a previous *in vivo* MRI study conducted to investigate signal changes induced by very small superparamagnetic iron oxide nanoparticles (VSOP) and Gd-BOPTA. For analytical discrimination from endogenous Fe, VSOP were doped with europium (Eu) resulting in Eu-VSOP. Formalin-fixed arterial specimens were cut into 5-μm serial sections and analyzed by immunohistochemistry (IHC: Movat's pentachrome, von Kossa, and Alcian blue (pH 1.0) staining, anti-smooth muscle cell actin (anti-SMA), and anti-rabbit macrophage (anti-RAM-11) immunostaining) and elemental microscopy with laser ablation inductively coupled plasma mass spectrometry (LA-ICP-MS) and synchrotron radiation μX-ray fluorescence (SR-μXRF) spectroscopy. Elemental distribution maps of Fe, Eu, Gd, sulfur (S), phosphorus (P), and calcium (Ca) were investigated.

Results: IHC characterized atherosclerotic plaque pathomorphology. Elemental microscopy showed S distribution to match the anatomy of arterial vessel wall layers, while P distribution corresponded well with cellular areas. LA-ICP-MS revealed Gd and Fe with a limit of detection of ~ 0.1 nmol/g and ~ 100 nmol/g, respectively. Eu-positive signal identified VSOP presence in the vessel wall and allowed the comparison of Eu-VSOP and endogenous Fe distribution in tissue sections. Extracellular matrix material correlated with Eu signal intensity, Fe concentration, and

Correspondence to: Yavuz Uca; *e-mail:* yavuz-oguz.uca@charite.de

Published online: 07 December 2020

maximum Gd concentration. Eu-VSOP were confined to endothelium in early lesions but accumulated in cellular areas in advanced plaques. Gd distribution was homogeneous in healthy arteries but inhomogeneous in early and advanced plaques. SR-μXRF scans at 0.5 μm resolution revealed Gd hotspots with increased P and Ca concentrations at the intimomedial interface, and a size distribution ranging from a few micrometers to submicrometers.
Conclusions: Eu-VSOP and Gd have distinct spatial distributions in atherosclerotic plaques. While Eu-VSOP distribution is more cell-associated and might be used to monitor atherosclerotic plaque progression, Gd distribution indicates arterial calcification and might help in characterizing plaque vulnerability.

Keywords: Atherosclerosis, MRI, Gadolinium, Iron oxide nanoparticles, Elemental microscopy, LA-ICP-MS, SXRFS, Extracellular matrix, Arterial calcification

Introduction

Atherosclerosis is the major promoter of cardiovascular disease with clinical manifestations including myocardial infarction, ischemic stroke, and sudden death [1]. In clinical routine, arterial stenosis or occlusion is diagnosed by X-ray angiography, computed tomography (CT) angiography (CTA), magnetic resonance imaging (MRI) angiography (MRA), or color-coded sonography (CCS). However, discrimination between stable and vulnerable atherosclerotic plaques is not reliably possible. Smaller plaques, which are not detected by these imaging modalities, can be subject to inflammation-driven complications that might result in fissures or erosions with the risk of thrombotic vessel wall occlusion [2].

Imaging methods including MRI, CT, positron emission tomography (PET), catheter-based virtual histology intravascular ultrasound (VH-IVUS), optical coherence tomography (OCT), and near-infrared spectroscopy (NIRS) are currently being investigated regarding their value for characterizing morphological changes leading to vulnerable plaque [3–7]. Among these methods, contrast-enhanced MRI allows noninvasive angiographic examination and assessment of local plaque composition [8]. Dynamic MRI acquisition after intravenous (IV) injection of contrast agents (CA) offers quantitative characterization of inflammatory processes during plaque progression. Several types of CA have been investigated for these purposes: (I) iron oxide nanoparticles (IONP), which are currently available only for experimental use, and (II) clinically available low-molecular-weight gadolinium (Gd)-based chelates (GBCA).

IONP are extensively used in MR imaging of experimental atherosclerosis particularly for detection of angiogenesis, inflammation, and apoptosis [9, 10]. IONP can be conjugated to antibodies or peptides to serve for targeted visualization of endothelial activity or myocardial infarction [11, 12]. After IV injection, IONP are rapidly cleared by the reticuloendothelial system due to their relatively large size. This provides a unique strategy for contrast-enhanced MRI, since phagocytosis results in concentration of the nanoparticles, which becomes detectable as decreased signal intensity typically 24 h after IV injection [13, 14]. Studies investigating very small superparamagnetic iron oxide nanoparticles (VSOP) with a hydrodynamic diameter of 7 nm, longer blood half-life, and faster vascular distribution due to their citrate surface coating have demonstrated even earlier uptake (< 2 h) into the atherosclerotic plaques, which correlated with the accumulation of extracellular matrix (ECM) [15, 16].

GBCA are known as nonspecific agents that result in increased MRI signal intensity through pronounced perfusion and vascular permeability. Although GBCA were developed to distribute within the vascular and extracellular space, and to be eliminated as intact molecules *via* the kidneys, studies have demonstrated Gd deposition predominantly around vascularized areas of the skin, brain, liver, and kidney [17, 18]. Systemic metal deposition was proposed, and colocalization of elements including phosphorus (P) or calcium (Ca) has suggested transchelation of Gd by physiological anions [19–21]. Although Gd deposition in the heart and aorta has also been reported, quantitative research in atherosclerotic plaques remains inadequate [19].

Discrimination between stable and vulnerable atherosclerotic plaques by contrast-enhanced MRI entails better understanding of IONP or GBCA interactions with plaque ECM components. Thus, elucidating microdistribution of CA in atherosclerotic plaques at different stages of disease progression by an experimental workflow with improved tissue detection ability offers a sophisticated basis. In this regard, mass spectrometry and X-ray fluorescence (XRF) analysis have emerged as two cutting-edge elemental microscopy techniques offering the lowest limit of detection (LOD) for reliable quantification of elements in tissue specimens and imaging characterization at the highest spatial resolution, respectively [22, 23].

In this study, we aimed to investigate the microdistribution of Eu-VSOP and Gd-BOPTA (gadobenate dimeglumine) in atherosclerotic plaques of New Zealand White (NZW) rabbits using immunohistochemistry (IHC) and elemental microscopy by laser ablation inductively coupled plasma mass spectrometry (LA-ICP-MS), and synchrotron radiation μXRF (SR-μXRF) spectroscopy.

Materials and Methods

Animal Procedures

The study was conducted in accordance with the requirements of directive 2010/63/EU and the German Animal Protection Act and approved by the local animal protection committee of the Landesamt für Gesundheit und Soziales (LAGeSo, Berlin State Office for Health and Social Affairs, Germany). Experimental conditions were constant at all times (see electronic supplementary material for induction of atherosclerosis). Twelve male NZW rabbits were IV injected with VSOP at a dose of 0.05 mmol Fe/kg body weight. VSOP were synthesized at the Charité Department of Radiology according to the protocol described by de Schellenberger et al. and had the following properties: 0.5 M Fe concentration with 13 % citric acid (weight/weight total Fe), 3 g/l sodium glycerophosphate, 2 g/l N-methylglucamine, and 60 g/l mannitol [24]. Synthesis was adapted to yield the final pharmaceutical formulation of the investigational drug VSOP-C184 used in clinical trials [25]. For unambiguous analytical discrimination from endogenous Fe, VSOP were doped with europium (Eu) by substituting ferric ions in a 5 % weight ratio of Eu3+ to Fe3+ resulting in Eu-VSOP, which has no influence on the magnetic properties of the particles [26]. At 1 h after Eu-VSOP injection, 10 rabbits were IV injected with Gd-BOPTA (Bracco Imaging Deutschland GmbH, Konstanz, Germany) at a dose of 0.1 mmol/kg, since Gd-BOPTA was often preferred for vascular MRI. The rabbits were sacrificed 2 h after the initial CA administration. The vascular system was perfused with electrolyte solution and the aortic arch was removed and processed by formalin fixation at 4 °C overnight and embedded in paraffin. Atherosclerosis-free control specimens (Eu-VSOP-negative and Gd-positive controls were Vasovist and elastin-specific CA (BMS753951) administered at a dose of 0.2 mmol/kg) were kindly provided by Marcus Makowski from our institution and processed under the same conditions [27].

Immunohistochemistry

The paraffin blocks were cut into 5-µm serial sections using an automated microtome, which were mounted on SuperFrost Ultra Plus microscope slides (VWR International, Geldenaaksebaan, Belgium) for IHC and LA-ICP-MS, or on ultralene foil for SR-µXRF analysis. Movat's pentachrome, von Kossa, and Alcian blue (pH 1.0) histologic staining, anti-smooth muscle cell (SMC) actin (anti-SMA), and anti-rabbit macrophage (anti-RAM-11) immunostaining procedures were carried out on adjacent sections as described elsewhere [16]. Qualitative and score-based semiquantitative assessment of plaque pathomorphology was done by independent observers recording pathologic features defined by the American Heart Association (AHA) (electronic supplementary material, Table 1) [28]. Digital high-resolution scans of the histologic specimens were obtained at the Zentrale Biomaterialbank der Charité (ZeBanC).

Laser Ablation Inductively Coupled Plasma Mass Spectrometry

LA-ICP-MS analysis was performed on the sections adjacent to IHC sections. For that, an ICP-MS (Agilent 7900, Waldbronn, Germany) was coupled to a laser ablation system (NWR 213; New Wave Research, California, USA). Prior to analysis, sections were deparaffinized. Laser ablation was performed in continuous-line ablation mode with a circular laser spot size of 20 µm at a scanning speed of 100 µm s^{-1} and 200 ms acquisition time with daily-optimized output energies of 1.5 J cm^{-1}. The method has been described elsewhere [29]. Ablated tissue was transported into the ICP-MS imager with helium gas at a flow of 0.9 L/min. Matrix-matched laboratory standards of well-defined element concentrations were spiked onto gelatin to quantify Gd and Fe (see also electronic supplementary material, Fig. S3). Fe concentration was determined by analysis of the isotope at mass 57 due to strong interference of $^{40}Ar^{16}O$ with the most abundant isotope at mass 56 [30]. Gd and Eu signals were determined by analysis at mass 158 and 153, respectively. Eu signal was only recorded in terms of counts per second (CPS) due to unavailability of standards. Generation of 2D distribution maps, image processing, and data evaluation were performed using MassImager, a free software developed by Robin Schmidt [31].

Synchrotron X-Ray Fluorescence Spectroscopy

SR-µXRF investigations on the sections adjacent to those used in LA-ICP-MS analysis were done at the ID21 beamline at the European Synchrotron Radiation Facility in Grenoble, France [32]. Experiments were performed using the in-vacuum scanning X-ray spectroscopy setup, in which X-rays were generated by undulators with an optimized gap size for 7.3 keV. The setup is explained in detail elsewhere [33]. The X-ray beam was focused down to ~0.6 × 0.8 $µm^2$ (vertical × horizontal) using a fixed-curvature Kirkpatrick-Baez mirror system. Flux was ~5×10^{10} photons/s (~180 mA SR current in multibunch mode). Acquisition time per pixel was 100 ms. Pixel size for collecting the XRF maps was set to 30 µm, 10 µm, 1–2 µm, or 0.5 µm depending on the size of the region of interest (ROI). Scans were acquired in continuous mode. Distribution maps of Fe, Gd, sulfur (S), P, and Ca were generated. XRF normalization, spectral deconvolution, and quantification were done using the PyMCA software (see also electronic supplementary material, Fig. S4) [34]. Cellular uptake of Gd was investigated by analyzing the P distribution as a marker of cell membrane, ATP, or nucleic acids. P distribution maps at 0.5 µm

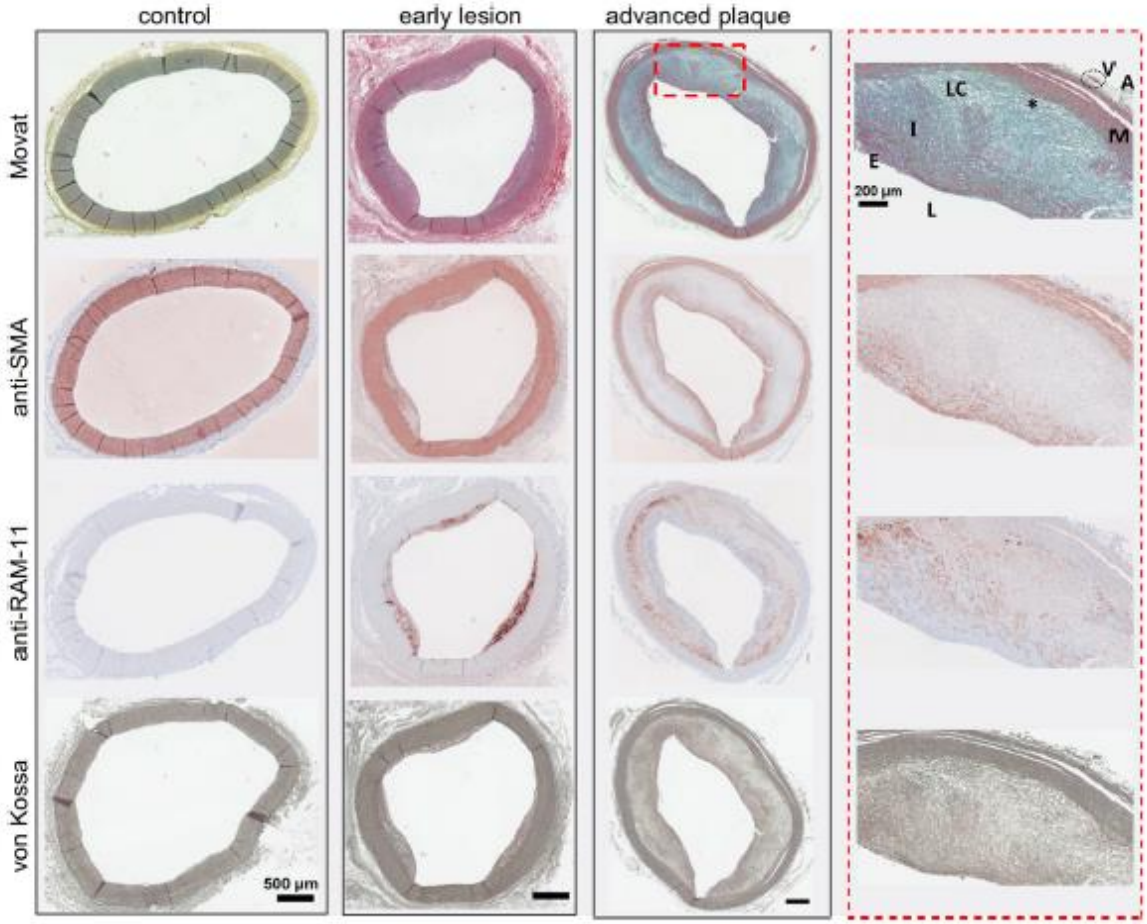

Fig. 1. Atherosclerotic plaque characterization by immunohistochemistry (IHC). Advanced plaque region of interest (ROI) (× 10 magnification) is provided for comparison. Movat's staining reveals cells by red staining that are also depicted by anti-smooth muscle cell (SMC) actin (anti-SMA) and anti-rabbit macrophage (anti-RAM-11) immunostaining. Contractile SMCs in the media and synthetic SMCs migrating into the intima are distinguished by their spindle-like and circular shapes, respectively. Lipid pools are nonstained circular, cleft-, or vacuole-like shapes at the intimomedial areas associated with increased macrophage colocalization, indicating foam cell or lipid cores. Lipid pools are surrounded by light blue-stained glycosaminoglycans (GAG). von Kossa staining identifies calcifications in the intima, especially along the intimomedial interface of advanced plaques. Scale bars, 500 µm; ROI, 200 µm; *L*, lumen; *E*, endothelium; *I*, intima; *LC*, lipid core; asterisk, intimomedial interface; *M*, media; *A*, adventitia; *V*, vasa vasorum.

resolution were segmented into two compartments by applying a 25% threshold on the maximum of the P K-line fluorescence signal and comparing elemental concentrations in P-poor (< 25% P-Threshold) or P-rich (> 25% P-Threshold) areas. Corresponding spectral deconvolution displaying colocalizing elements was normalized by the number of pixel of each region, thus giving an averaged spectrum for each region. The amplitude of the peak corresponding to the respective element was scaled by the amount of atoms being probed by the X-ray beam. Size distribution analysis of Gd hotspots was done using the ImageJ software.

Results

IHC performed on adjacent sections of arterial specimens obtained from 14 rabbits revealed various degrees of atherosclerotic plaque formation. These were categorized into early lesion and advanced plaque using the pathologic plaque features defined by the AHA (Fig. 1, control: $n = 2$, early lesion: $n = 3$, advanced plaque: $n = 9$, see electronic supplementary material Table 1). Movat's staining revealed the individual arterial vessel wall layers (adventitia, media, intima, and endothelium). Medial and endothelial regions were the major cellular areas, identified by red staining, which was also depicted by SMA and RAM-11 immunostaining. Contractile SMCs in the media and synthetic SMCs migrating into the intima were distinguishable by their spindle-like and circular shapes, respectively. Large lipid pools were seen as nonstaining circular, cleft-, or vacuole-like shapes mostly at the intimomedial interface associated with increased macrophage colocalization, indicating foam cell or lipid core formation. These were often surrounded by light blue-stained glycosaminoglycan (GAG) networks. Synthetic SMCs and stretches of yellow/green-stained collagen fibrils were observed covering the lipid pools. von

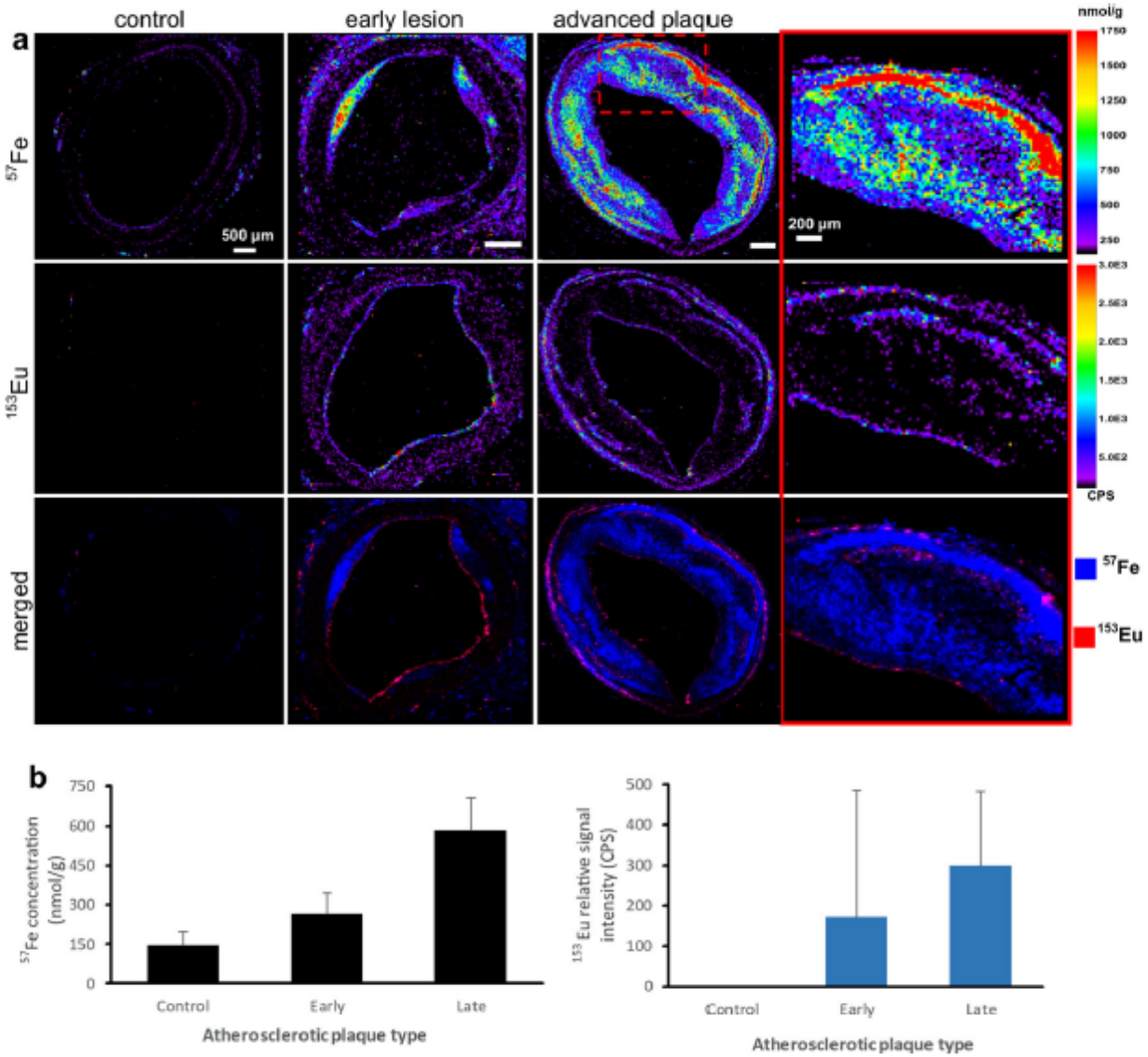

Fig. 2. Europium (Eu)-doped very small superparamagnetic iron (Fe) oxide nanoparticle (Eu-VSOP) distribution in atherosclerotic plaques. **a** Laser ablation inductively coupled plasma mass spectrometry (LA-ICP-MS) elemental maps of $^{57}Fe^{1+}$ and $^{153}Eu^{1+}$ distribution. Advanced plaque ROI is provided for comparison. Eu-positive signal (recorded in counts per second, CPS) distinguishes Eu-VSOP distribution from that of endogenous Fe. No Eu signal is detected in controls; weaker Eu signal is detected in the media and the intima of early lesions. Eu signal intensity and Fe concentrations increase in advanced plaques. High Eu signal is confined to endothelium or to the intimomedial interface. Scale bars, 500 µm, ROI, 200 µm. **b** Graphs of Fe concentration and Eu signal intensity in atherosclerotic plaques. Fe concentrations: 146.17 nmol/g (± 52.58 nmol/g) in healthy arteries, 264.89 nmol/g (± 79.23 nmol/g) in early lesions, and 583.20 nmol/g (± 122.46 nmol/g) in advanced plaques.

Kossa staining revealed intimal calcifications, especially along the intimomedial interface of advanced plaques (see also electronic supplementary material, Fig. S1).

Metal and nonmetal images obtained by elemental microscopy matched the pathomorphologic features identified by IHC with S distribution highlighting the anatomy of the arterial vessel wall layers, while P distribution corresponded well with cellular areas (Fig. 6). LA-ICP-MS revealed Gd or Fe distribution at 20-µm resolution (*x-y* direction) with a LOD of ~0.1 nmol/g for Gd, and ~100 nmol/g for Fe. No Eu signal was detected in controls (Fig. 2). Eu-positive signal identified the VSOP presence in the vessel wall, and by acting as a surrogate marker, it allowed the comparison of Eu-VSOP and endogenous Fe distribution in tissue sections. Weaker Eu signal was detected in the media and the intima of early lesions. Eu signal intensity and Fe concentrations were higher in larger plaques compared to smaller ones. High Eu signal was confined to endothelium or the intimomedial interface. Fe concentrations were 146.17 nmol/g (± 52.58 nmol/g) in healthy arteries, 264.89 nmol/g (± 79.23 nmol/g) in early lesions, and 583.20 nmol/g (± 122.46 nmol/g) in advanced plaques.

In the control group (Eu-VSOP-negative, Gd-positive), Gd was detected (Fig. 3). In healthy arteries, Gd distribution was global and homogeneous. In early lesions, Gd was distributed inhomogeneously and concentrations were higher in the subendothelial space. Advanced plaques were

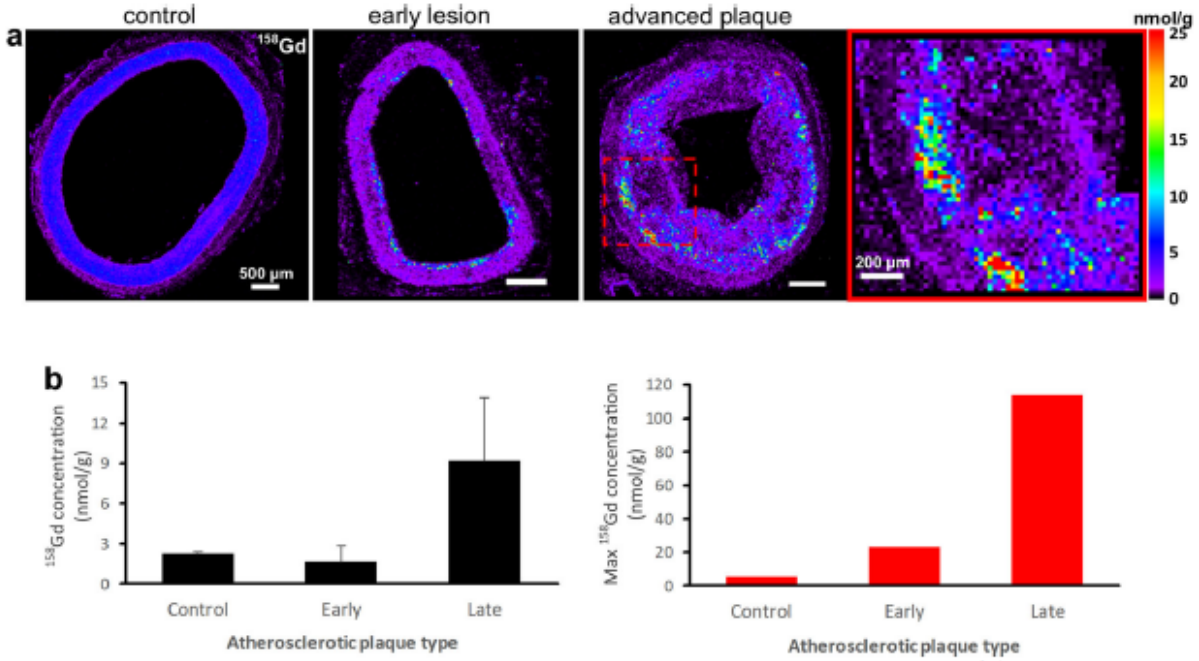

Fig. 3. Gadolinium (Gd) distribution in atherosclerotic plaques. **a** LA-ICP-MS elemental map of ^{158}Gd distribution. Advanced plaque ROI is provided for comparison. Gd is also detected in the control group (Eu-VSOP-negative, Gd-positive). In healthy arteries, Gd distribution is global and homogenous. In early lesions, Gd concentrations are higher in the subendothelial space. Advanced plaques are characterized by high focal Gd content at the intimomedial interface. Scale bars, 500 µm; ROI, 200 µm. **b** Graphs of Gd and maximum Gd concentration in atherosclerotic plaques. Gd concentrations: 2.22 nmol/g (± 0.14 nmol/g), 1.63 nmol/g (± 1.19 nmol/g), and 9.23 nmol/g (± 4.64 nmol/g), with maximum concentrations of 5.30 nmol/g, 22.85 nmol/g, and 113.66 nmol/g in healthy arteries, early, and advanced plaques, respectively.

characterized by high focal Gd content at the intimomedial interface. Gd concentrations were 2.22 nmol/g (± 0.14 nmol/g), 1.63 nmol/g (± 1.19 nmol/g), and 9.23 nmol/g (± 4.64 nmol/g), with maximum concentrations of 5.30 nmol/g, 22.85 nmol/g, and 113.66 nmol/g in healthy arteries, early, and advanced plaques, respectively.

SR-µXRF analysis at 30-µm-step width detected Gd in 4 samples—one early lesion and 3 advanced plaques. Predefined ROIs within these specimens were further investigated for their Gd content at higher resolution down to 0.5 µm, which displayed increasing Gd concentrations (Fig. 4). Higher-resolution scans revealed increasing local Gd, P, and Ca concentrations in progressing plaques (Figs. 4 and 5). SR-µXRF analysis at 10-µm- and 2-µm-step width and RGB overlay of P, S, and Fe maps revealed distinct Fe distribution around cell- or collagen-rich areas in the intima (Fig. 6). In comparison, RGB overlay of Gd, S, and Fe maps in addition to P, S, and Gd maps revealed Gd distribution within the deeper areas of the intima, especially along the intimomedial interface at increasing concentrations colocalized with P and Ca. Finally, analysis of possible cellular uptake of Gd (see the "Materials and Methods" section) yielded Gd, P, and Ca concentrations of ~0.1 mM, 62 mM, and 87 mM, respectively, in areas below the threshold (Fig. 7, electronic supplementary material, Fig. S5). In areas above the threshold, which indicates elemental hotspots, these concentrations were ~2.5 mM, 779 mM, and 789 mM, respectively. Size distribution analysis revealed Gd-rich hotspots ranging from a few micrometers to submicrometers, which corroborated with von Kossa-stained calcified deposits.

Discussion

The aim of this study was to investigate the microdistribution of Gd- and iron oxide-based CA in the atherosclerotic plaques of NZW rabbits after IV injection of Eu-VSOP and Gd-BOPTA. VSOP are increasingly being investigated in MR imaging of experimental atherosclerosis owing to their early uptake (< 2 h) into atherosclerotic plaques that correlates with accumulation of the ECM rather than phagocytosis [15, 16]. ECM accumulation is a marker of atherosclerotic plaque progression; therefore, correlations of ECM material with Fe concentration, Eu signal intensity as a surrogate marker of VSOP, and Gd concentration were investigated [35]. Eu-doping of the iron oxide cores of the nanoparticles enabled their detection by the LA-ICP-MS analysis and distinguished their distribution from that of endogenous Fe [26]. Overall, our results show correlations between ECM material and Fe concentration or Eu signal intensity.

Published data suggest that VSOP enter atherosclerotic plaques through the endothelium or macrophage phagocytosis [36]. In endothelial cells, uptake was shown to be mediated by endosomal pathway [37]. These findings are supported by our investigations, which demonstrate Eu-VSOP mostly along the endothelium, superficially in the subendothelial space and at the boundaries of the adventitia,

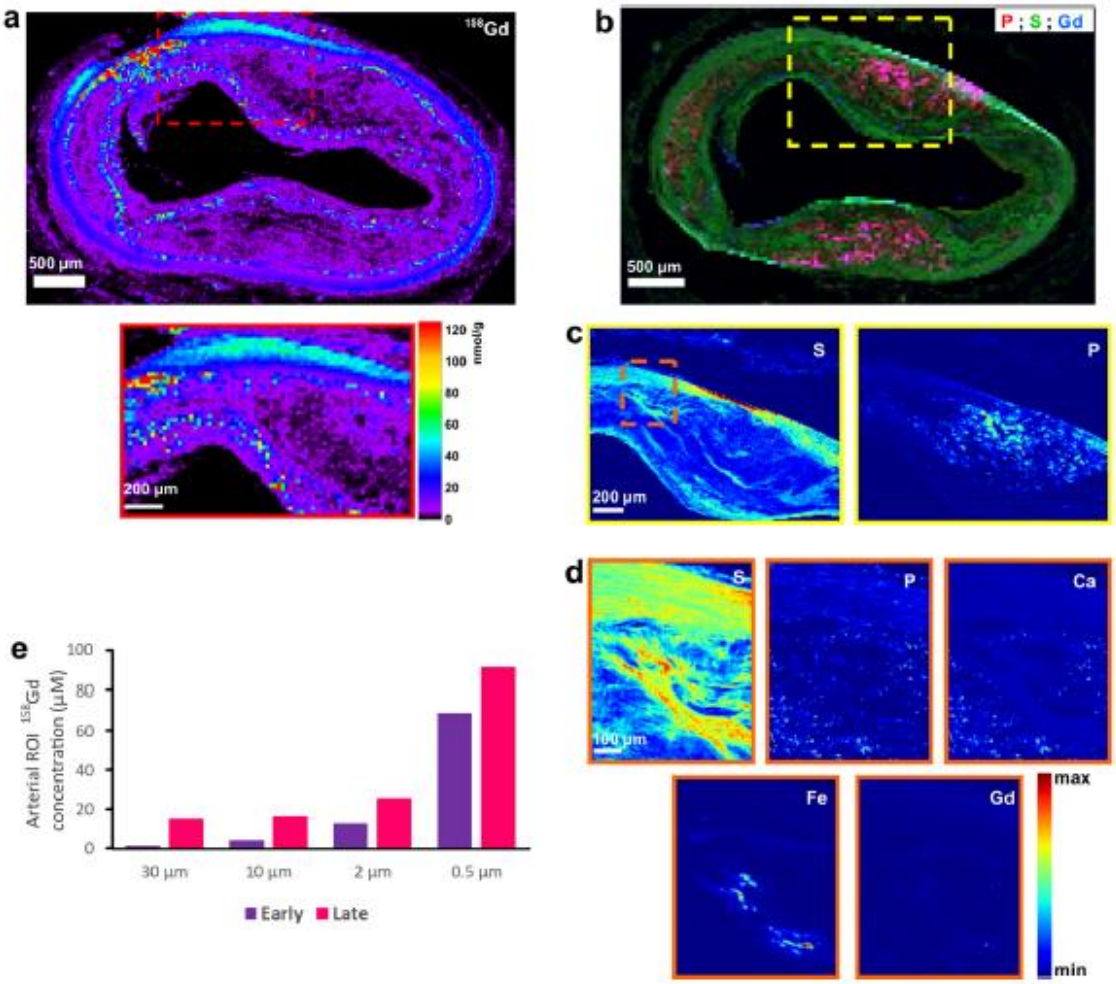

Fig. 4. Spatially resolved Gd distribution and elemental hotpots in atherosclerotic plaques. **a** LA-ICP-MS elemental map of ^{158}Gd distribution. Advanced plaque ROI is provided for comparison. Scale bars, 500 µm; ROI, 200 µm. **b–d** Synchrotron radiation µX-ray fluorescence (SR-µXRF) analysis at increasing resolution. **b** RGB overlay of phosphorus (P), sulfur (S), and Gd distribution at 30-µm resolution. **c** ROI elemental maps of S and P at 10-µm resolution reveal arterial vessel wall anatomy and cellular zones. **d** ROI elemental maps of S, P, calcium (Ca), Fe, and Gd at 2-µm resolution. Scale bars: b1, 500 µm; b2, 200 µm; b3, 50 µm. **e** SR-µXRF analysis in both early lesions and advanced plaques reveals increasing ROI Gd concentrations with increasing spatial resolution.

media, and intima (Fig. 2). Although Eu detection remained beyond the sensitivity of SR-µXRF, RGB overlays of P, S, and Fe maps highlighted Fe distribution in cell- or collagen-rich areas (Fig. 6). Cells respond to changes in Fe concentration by interactions involving Fe transport, Fe-S clustering or storage proteins, and highly sulfated GAGs [38]. IONP can be metabolized to soluble Fe, which might be stored as ferritin or released into an inflammatory environment [39]. Increased vasa vasorum activity results in the formation of fragile microvessels that might enhance nanoparticle uptake into the plaque ECM (Fig. 1, electronic supplementary material, Fig. S2) [40].

Gd concentration, unlike that of Fe, did not correlate with increased ECM material. Remarkably though, compared to healthy arteries, maximum Gd concentrations were 4 and 21 times higher in early and advanced plaques, respectively. This indicates focal Gd hotspots. Advanced plaques were characterized by a large number of such hotspots in deeper regions of the intima corresponding to the intimomedial interface, which hosts large lipid pools and macrophages (Figs. 1 and 3). In ROIs including such areas, SR-µXRF analysis at ~0.5-µm resolution confirmed Gd content exceeding mM concentrations with high P and Ca colocalization (Fig. 5). These results are in line with studies suggesting insoluble complex formation [20, 21]. An earlier study suggests that Gd uptake into atherosclerotic plaques occurs through binding and complexation with serum albumin and breakdown of Gd-chelates at the endothelium or vasa vasorum [41]. The authors of this study postulate ECM accumulation of Gd through interactions with collagen, proteoglycans, and tenascin [41]. Another study identified the integrity of the collagen network in cartilage to be a determinant of gadopentetate dimeglumine (Magnevist) accumulation [42]. Our results are consistent with these findings in that dense stretches of collagen fibrils resulted in boundary formation around lipid-rich zones (Fig. 6, electronic supplementary material, Fig. S1). This might lead to selective Gd

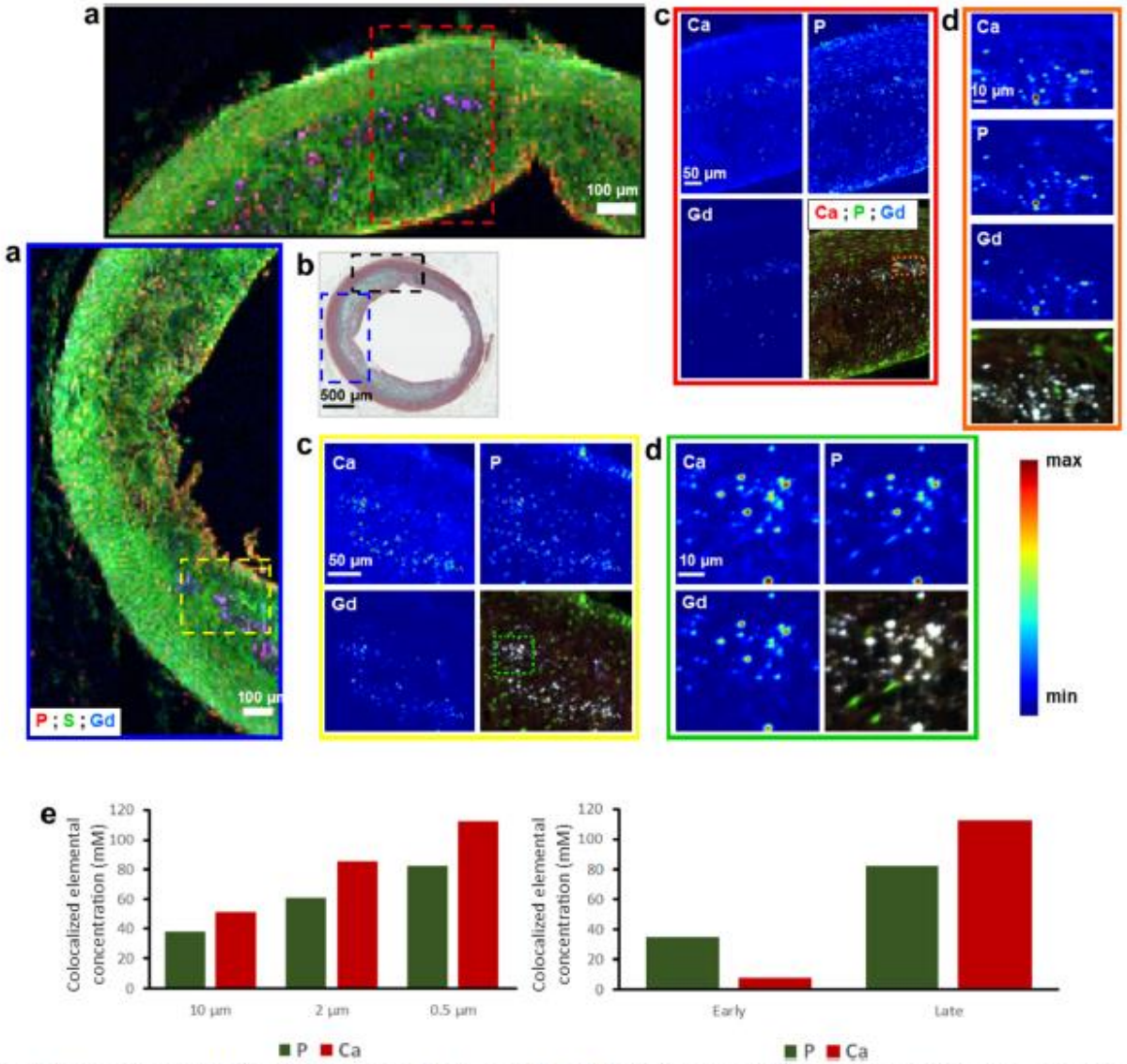

Fig. 5. Spatially resolved Gd hotpots and colocalization of P and Ca in atherosclerotic plaques. SR-µXRF analysis results of 2 ROIs in an advanced plaque are provided for comparison. **a** RGB overlay P, S, and Gd distribution at 10-µm resolution. Scale bars, 100 µm. **b** Movat's staining micrograph is provided for an overview. **c** Elemental maps and RGB overlay of Ca, P, and Gd distribution at 2-µm resolution. Scale bars, 50 µm. **d** Elemental maps and RGB overlay of Ca, P, and Gd distribution at 0.5-µm resolution. Scale bars, 10 µm. **e** SR-µXRF analysis of Gd hotspots reveals higher P and Ca concentrations in progressing plaques (*right*), and concentrations further increase with increasing spatial resolution (*left*).

deposition along the lipid pool-rich intimomedial interface or Gd concentration gradients, possibly through interactions with GAGs. GAGs are upregulated during plaque progression [43]. Their highly negatively charged side chains contribute to complex formation through establishing electrostatic bridges or performing higher level of interactions especially with positive amino-acid residues of proteins including low density lipoprotein (LDL), platelet factor-4 (PF4), or fibroblast growth factor-2 (FGF-2) [44]. This ability makes them excellent candidates for ligand competition reactions, especially through facilitation of highly abundant divalent or trivalent cations, which stabilize these complexes [45]. Although Gd-BOPTA is negatively charged, it is likely to undergo partial or complete chelate dissociation in metabolically active inflammatory sites of the atherosclerotic ECM. Notably, the MRI signal-enhancing effect of Gd was reported to increase dramatically after GBCA incubation including Gd-BOPTA in heparin, which is a highly sulfated GAG type [21].

Finally, although GBCA were originally developed to distribute extracellularly after IV administration, it has been speculated that reactive cellular responses may occur [46]. Inhibition of phagocytosis and macrophage apoptosis upon Gd exposure have been reported [47, 48]. The threshold we applied on the fluorescence signal detected for the P distribution at 0.5-µm resolution analyzed by SR-µXRF corroborates a cellular response since high P distribution marks cell membrane, ATP, or nucleic acids. Increased Gd, P, and Ca concentrations in areas above the threshold confirm Gd hotspots and further support complexation with P and Ca. The size distribution of these

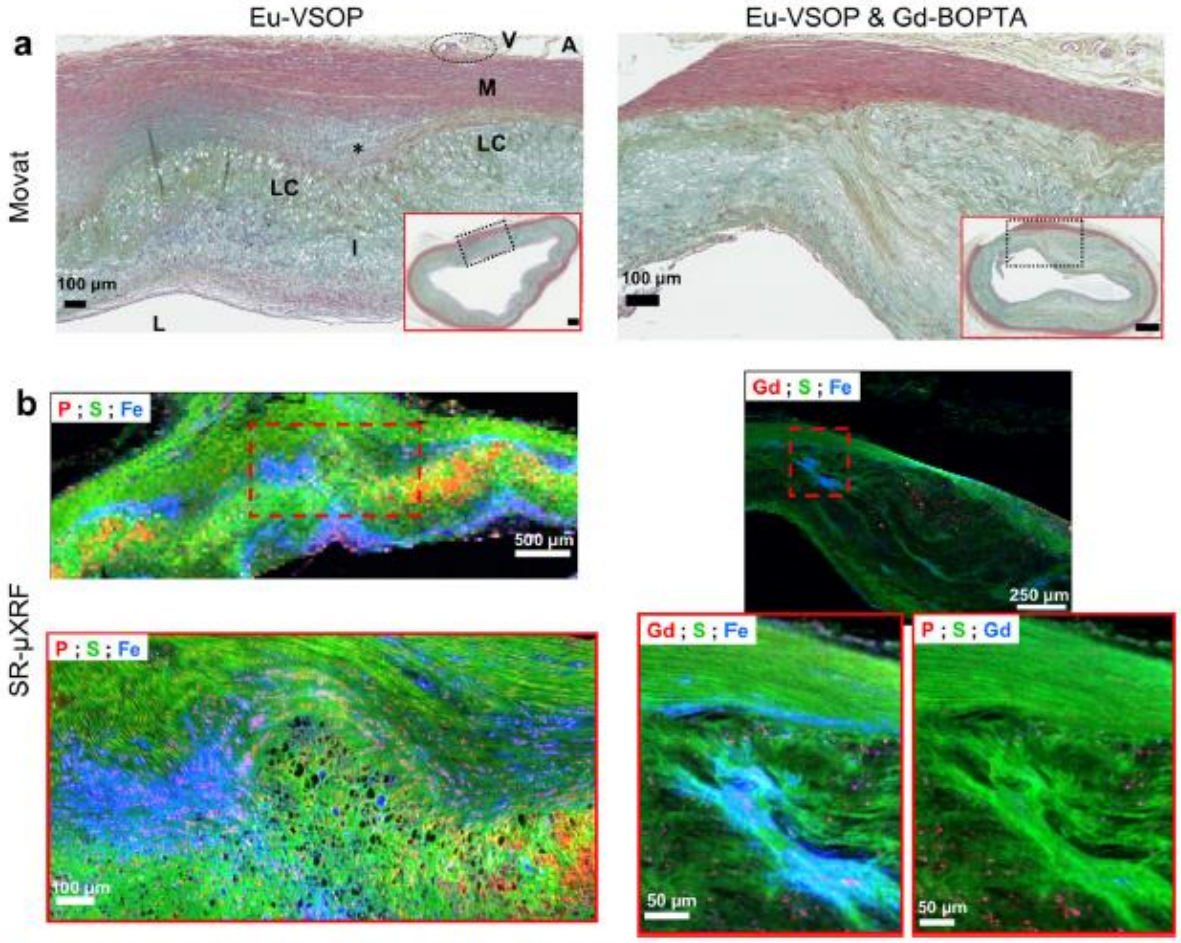

Fig. 6. Comparative microdistribution of Fe and Gd in atherosclerotic plaques. Rabbits were intravenously injected with either Eu-VSOP alone (*left*) or Eu-VSOP and Gd-BOPTA (*right*). **a** Microscopic characterization of Movat's stained advanced plaque pathomorphology. (ROIs, × 10 magnification). Synthetic SMCs and dense stretches of yellow/green-stained collagen fibrils are seen covering the lipid pools. Scale bars, 500 µm; ROI, 100 µm. **b** SR-µXRF analysis at 10-µm and 2-µm resolution (ROIs are indicated by red dashed lines). RGB overlay of P, S, and Fe maps demonstrates distinct Fe distribution in cell- or collagen-rich areas in the intima or at the boundary between the media and intima (*left*; scale bars, 500 µm; ROI, 100 µm). RGB overlay of Gd, S, and Fe maps in addition to P, S, and Gd maps revealed Gd distribution within the deeper areas of the intima, especially along the intimomedial interface at highly increasing concentrations colocalized with P and Ca, distinguishing Gd distribution from that of Eu-VSOP (*right*; scale bars, 250 µm; ROI, 50 µm). *L*, lumen; *I*, intima; *LC*, lipid core; asterisk, intimomedial interface; *M*, media; ***A***, adventitia; ***V***, vasa vasorum.

hotspots ranging from a few micrometers to submicrometers indicates Gd involvement in arterial calcification, presumably through uptake by cells that undergo calcified apoptosis or extracellular mineralization (Fig. 7, electronic supplementary material, Fig. S5) [49]. Arterial calcification is an active and highly regulated process of atherogenesis. It is similar to bone formation, occurs parallel to arterial lipid build-up, and becomes a key characteristic of advanced plaques [50]. We detected such calcifying regions in advanced plaque sections, especially in microzones along the intimomedial interface colocalizing with Gd hotspots (Figs. 1 and 7).

Our study has several limitations including sample processing and the small sample size. Investigation of a larger sample set in this study would have been excessively demanding and not feasible for elemental microscopy during our granted beam time at the European Synchrotron Radiation Facility. Sample processing by means of tissue fixation and paraffin embedding is a standard method in IHC analysis. Paraffin infiltration facilitates uniform slicing and reproducibility of serial sectioning, although it might also result in capture of elements. We performed deparaffinization before LA-ICP-MS analysis; however, ethanol-washing steps during this process might have altered the measured elemental concentrations we measured, particularly for elements involved in transient interactions.

Conclusion

This is the first study comparing the microdistribution of Gd- and iron oxide-based MR contrast agents in atherosclerotic plaques. We performed IHC and correlative elemental microscopy by LA-ICP-MS and SR-µXRF, and achieved a

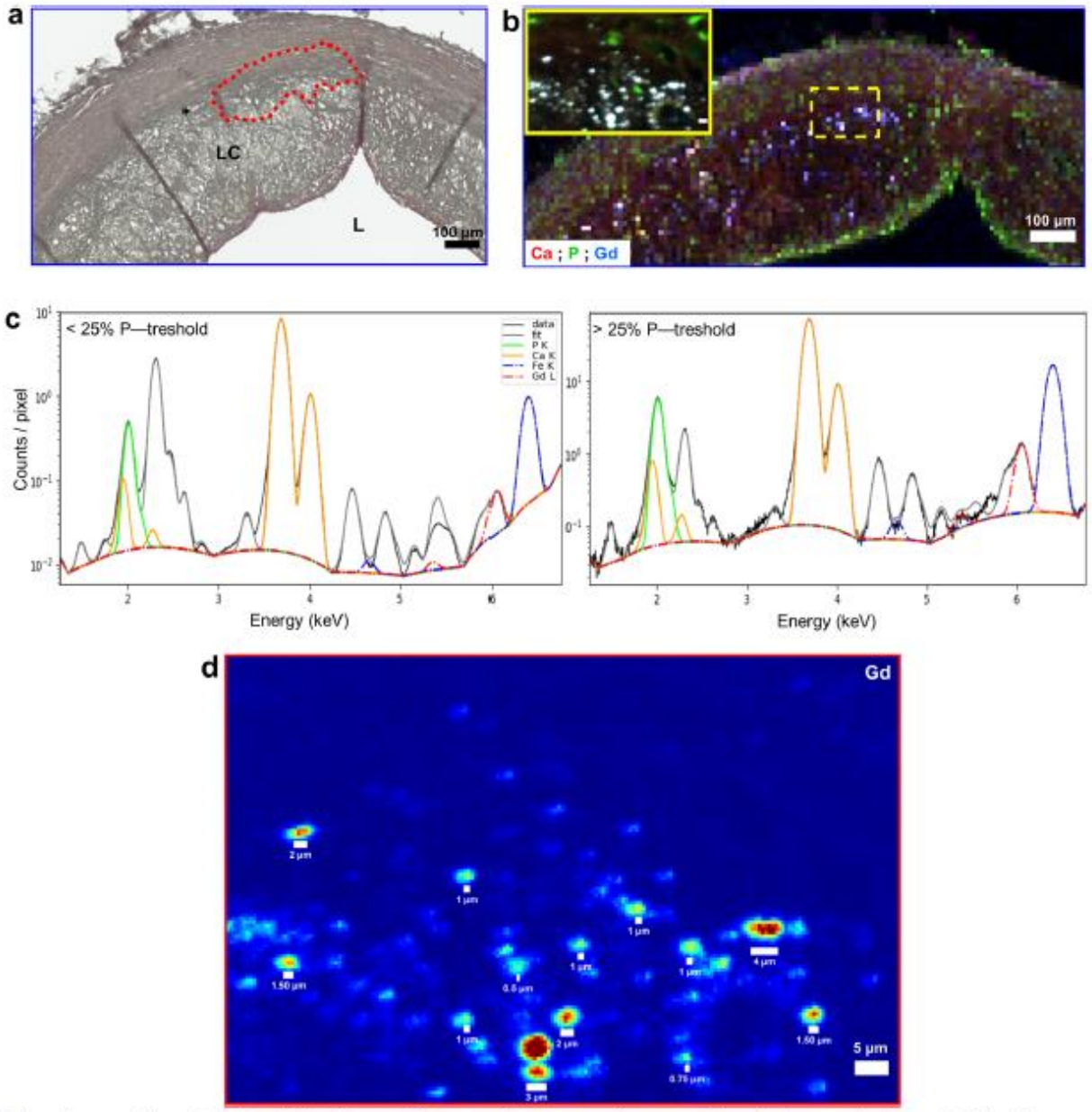

Fig. 7. Gd involvement in arterial calcification. **a** Micrograph of a von Kossa-stained advanced plaque ROI (× 15 magnification) reveals arterial calcifications, which are enriched at the intimomedial interface (asterisk, also indicated by the dashed red lines). Scale bar, 100 µm; *L*, lumen; *LC*, lipid core. **b** SR-µXRF analysis and RGB overlay of Ca, P, and Gd distribution at 10-µm and 0.5-µm resolution (ROIs are marked by yellow dashed lines). Scale bars, 100 µm; ROI, 5 µm. **c** Cellular uptake of Gd is investigated by analyzing the P distribution as a marker of cell membrane, ATP, or nucleic acids. P distribution maps at 0.5-µm resolution are segmented into two compartments by applying a 25 % threshold on the maximum of the P K-line fluorescence signal and comparing elemental concentrations in P-poor (< 25 % P-Threshold) or P-rich (> 25 % P-Threshold) areas. Corresponding spectral deconvolution displaying colocalizing elements are normalized by the number of pixel of each region, thus giving an averaged spectrum for each region. The amplitude of the peak corresponding to the respective element is scaled by the amount of atoms being probed by the X-ray beam. In contrast to P-poor areas with < 1 mM, 62 mM, and 87 mM of Gd, P and Ca, respectively, P-rich areas contained > 2 mM, 779 mM, and 789 mM of Gd, P and Ca, respectively. Since P-rich compartments mark the cells or indicate close proximity to the cells, Gd could have been taken up by the cells, presumably by those that undergo calcified apoptosis, or may be involved in extracellular mineralization through complexation with P and Ca. **d** Size distribution analysis shows Gd-rich hotspots ranging from a few micrometers to submicrometers, which corroborates with von Kossa-stained calcified deposits, and indicates Gd involvement in arterial calcification.

limit of detection at ~0.1 nmol/g and a spatial resolution at 0.5 µm. Overall, these methods allowed differentiation of atherosclerotic plaque tissue distributions of Eu-VSOP and Gd, which are determined by the microstructural ECM composition. We found arterial vessel wall Fe concentration and Eu signal intensity to increase with atherosclerotic plaque progression, suggesting that Eu-VSOP might be used to monitor plaque progression by experimental MRI

investigations. Furthermore, we found that the intimomedial interface is a crucial microenvironment for Gd-rich elemental hotspots. Colocalization of increased Ca and P and the size distribution of Gd hotspots ranging from a few micrometers to submicrometers indicate arterial calcification, which might help in characterizing morphological changes underlying plaque vulnerability, and in turn pave the way for MRI signal intensity-based discrimination of stable plaques from vulnerable plaques.

Supplementary Information. The online version contains supplementary material available at https://doi.org/10.1007/s11307-020-01563-z.

Acknowledgements. Open Access funding enabled and organized by Projekt DEAL. We acknowledge excellent cooperation with the European Synchrotron Radiation Facility (ESRF), which allocated beamline ID21 beamtime (proposal number: MD-1163), and Zentrale Biomaterialbank der Charité (ZeBanC). We thank Janni Breinl for her contribution in the earlier MRI study. We also thank Dr. Antje Ludwig, Dr. Judith Bergs, Prof. Dr. Tobias Schäffter, and Prof. Dr. Ingolf Sack for their valuable support, Rafet Güven for graphical artwork, and Bettina Herwig for language editing.

Funding. This work was supported by Deutsche Forschungsgemeinschaft (German Research Foundation, DFG), Grant/Award Number: GRK 2260, BIOQIC, and SFB 1340, Matrix in Vision.

Compliance with Ethical Standards

Conflict of Interest

The authors declare that they have no conflict of interest.

References

1. Benjamin EJ, Blaha MJ, Chiuve SE, Cushman M, Das SR, Deo R, de Ferranti SD, Floyd J, Fornage M, Gillespie C, Isasi CR, Jiménez MC, Jordan LC, Judd SE, Lackland D, Lichtman JH, Lisabeth L, Liu S, Longenecker CT, Mackey RH, Matsushita K, Mozaffarian D, Mussolino ME, Nasir K, Neumar RW, Palaniappan L, Pandey DK, Thiagarajan RR, Reeves MJ, Ritchey M, Rodriguez CJ, Roth GA, Rosamond WD, Sasson C, Towfighi A, Tsao CW, Turner MB, Virani SS, Voeks JH, Willey JZ, Wilkins JT, Wu JH, Alger HM, Wong SS, Muntner P, American Heart Association Statistics Committee and Stroke Statistics Subcommittee (2017) Heart Disease and Stroke Statistics-2017 update: a report from the American Heart Association. Circulation 135:e146–e603
2. Davies MJ (1996) Stability and instability: two faces of coronary atherosclerosis: the Paul Dudley White Lecture 1995. Circulation 94:2013–2020
3. Voros S, Rinehart S, Qian Z, Joshi P, Vazquez G, Fischer C, Belur P, Hulten E, Villines TC (2011) Coronary atherosclerosis imaging by coronary CT angiography: current status, correlation with intravascular interrogation and meta-analysis. JACC Cardiovasc Imaging 4:537–548
4. Skagen K, Johnsrud K, Evensen K, Scott H, Krohg-Sørensen K, Reier-Nilsen F, Revheim ME, Fjeld JG, Skjelland M, Russell D (2015) Carotid plaque inflammation assessed with ^{18}F-FDG PET/CT is higher in symptomatic compared with asymptomatic patients. Int J Stroke 10:730–736
5. Kilic ID, Caiazzo G, Fabris E, Serdoz R, Abou-Sherif S, Madden S, Moreno PR, Goldstein J, di Mario C (2015) Near-infrared spectroscopy-intravascular ultrasound: scientific basis and clinical applications. Eur Heart J Cardiovasc Imaging 16:1299–1306
6. Tearney GJ, Regar E, Akasaka T, Adriaenssens T, Barlis P, Bezerra HG, Bouma B, Bruining N, Cho JM, Chowdhary S, Costa MA, de Silva R, Dijkstra J, di Mario C, Dudeck D, Falk E, Feldman MD, Fitzgerald P, Garcia H, Gonzalo N, Granada JF, Guagliumi G, Holm NR, Honda Y, Ikeno F, Kawasaki M, Kochman J, Koltowski L, Kubo T, Kume T, Kyono H, Lam CCS, Lamouche G, Lee DP, Leon MB, Maehara A, Manfrini O, Mintz GS, Mizuno K, Morel MA, Nadkarni S, Okura H, Otake H, Pietrasik A, Prati F, Räber L, Radu MD, Rieber J, Riga M, Rollins A, Rosenberg M, Sirbu V, Serruys PWJC, Shimada K, Shinke T, Shite J, Siegel E, Sonada S, Suter M, Takarada S, Tanaka A, Terashima M, Troels T, Uemura S, Ughi GJ, van Beusekom HMM, van der Steen AFW, van Es GA, van Soest G, Virmani R, Waxman S, Weissman NJ, Weisz G (2012) Consensus standards for acquisition, measurement, and reporting of intravascular optical coherence tomography studies: a report from the International Working Group for Intravascular Optical Coherence Tomography Standardization and Validation. J Am Coll Cardiol 59:1058–1072
7. Garcia-Garcia HM, Mintz GS, Lerman A et al (2009) Tissue characterisation using intravascular radiofrequency data analysis: recommendations for acquisition, analysis, interpretation and reporting. Eurointervention J Eur Collab Work Group. Interv Cardiol Eur Soc Cardiol 5:177–189
8. Corti R, Fuster V (2011) Imaging of atherosclerosis: magnetic resonance imaging. Eur Heart J 32:1709–1719
9. Sosnovik DE, Nahrendorf M, Weissleder R (2007) Molecular magnetic resonance imaging in cardiovascular medicine. Circulation 115:2076–2086
10. Majmudar MD, Nahrendorf M (2012) Cardiovascular molecular imaging: the road ahead. J Nucl Med 53:673–676
11. Michalska M, Machtoub L, Manthey HD, Bauer E, Herold V, Krohne G, Lykowsky G, Hildenbrand M, Kampf T, Jakob P, Zernecke A, Bauer WR (2012) Visualization of vascular inflammation in the atherosclerotic mouse by ultrasmall superparamagnetic iron oxide vascular cell adhesion molecule-1–specific nanoparticles. Arterioscler Thromb Vasc Biol 32:2350–2357
12. Weissleder R, Lee AS, Khaw BA, Shen T, Brady TJ (1992) Antimyosin-labeled monocrystalline iron oxide allows detection of myocardial infarct: MR antibody imaging. Radiology 182:381–385
13. Kolodgie FD, Petrov A, Virmani R, Narula N, Verjans JW, Weber DK, Hartung D, Steinmetz N, Vanderheyden JL, Vannan MA, Gold HK, Reutelingsperger CPM, Hofstra L, Narula J (2003) Targeting of apoptotic macrophages and experimental atheroma with radiolabeled Annexin V: a technique with potential for noninvasive imaging of vulnerable plaque. Circulation 108:3134–3139
14. Sadat U, Usman A, Gillard JH (2017) Imaging pathobiology of carotid atherosclerosis with ultrasmall superparamagnetic particles of iron oxide: an update. Curr Opin Cardiol 32:437–440
15. Ludwig A, Poller WC, Westphal K, Minkwitz S, Lättig-Tünnemann G, Metzkow S, Stangl K, Baumann G, Taupitz M, Wagner S, Schnorr J, Stangl V (2013) Rapid binding of electrostatically stabilized iron oxide nanoparticles to THP-1 monocytic cells via interaction with glycosaminoglycans. Basic Res Cardiol 108:328
16. Wagner S, Schnorr J, Ludwig A, Stangl V, Ebert M, Hamm B, Taupitz M (2013) Contrast-enhanced MR imaging of atherosclerosis using citrate-coated superparamagnetic iron oxide nanoparticles: calcifying microvesicles as imaging target for plaque characterization. Int J Nanomedicine 8:767–779
17. Grobner T (2006) Gadolinium – a specific trigger for the development of nephrogenic fibrosing dermopathy and nephrogenic systemic fibrosis? Nephrol Dial Transplant 21:1104–1108
18. Fingerhut S, Niehoff AC, Sperling M, Jeibmann A, Paulus W, Niederstadt T, Allkemper T, Heindel W, Holling M, Karst U (2018) Spatially resolved quantification of gadolinium deposited in the brain

of a patient treated with gadolinium-based contrast agents. J Trace Elem Med Biol 45:125–130
19. Swaminathan S, High WA, Ranville J, Horn TD, Hiatt K, Thomas M, Brown HH, Shah SV (2008) Cardiac and vascular metal deposition with high mortality in nephrogenic systemic fibrosis. Kidney Int 73:1413–1418
20. Laurent S, Vander EL, Henoumont C et al (2010) How to measure the transmetallation of a gadolinium complex. Contrast Media Mol Imaging 5:305–308
21. Taupitz M, Stolzenburg N, Ebert M, Schnorr J, Hauptmann R, Kratz H, Hamm B, Wagner S (2013) Gadolinium-containing magnetic resonance contrast media: investigation on the possible transchelation of Gd 3+ to the glycosaminoglycan heparin: GdCM, Glycosaminoglycans and Transchelation. Contrast Media Mol Imaging 8:108–116
22. Ortega R, Devès G, Carmona A (2009) Bio-metals imaging and speciation in cells using proton and synchrotron radiation X-ray microspectroscopy. J R Soc Interface 6:S649–S658
23. Becker JS, Matusch A, Wu B (2014) Bioimaging mass spectrometry of trace elements – recent advance and applications of LA-ICP-MS: a review. Anal Chim Acta 835:1–18
24. de Schellenberger AA, Hauptmann R, Millward JM, Schellenberger E, Kobayashi Y, Taupitz M, Infante-Duarte C, Schnorr J, Wagner S (2017) Synthesis of europium-doped VSOP, customized enhancer solution and improved microscopy fluorescence methodology for unambiguous histological detection. J Nanobiotechnol 15:71
25. Taupitz M, Wagner S, Schnorr J et al (2004) Phase I clinical evaluation of citrate-coated monocrystalline very small superparamagnetic iron oxide particles as a new contrast medium for magnetic resonance imaging. Investig Radiol 39:394–405
26. Kobayashi Y, Hauptmann R, Kratz H, Ebert M, Wagner S, Taupitz M (2017) Europium doping of superparamagnetic iron oxide nanoparticles enables their detection by fluorescence microscopy and for quantitative analytics. Technol Health Care 25:457–470
27. Makowski MR, Wiethoff AJ, Blume U, Cuello F, Warley A, Jansen CHP, Nagel E, Razavi R, Onthank DC, Cesati RR, Marber MS, Schaeffter T, Smith A, Robinson SP, Botnar RM (2011) Assessment of atherosclerotic plaque burden with an elastin-specific magnetic resonance contrast agent. Nat Med 17:383–388
28. Virmani R, Kolodgie FD, Burke AP, Farb A, Schwartz SM (2000) Lessons from sudden coronary death: a comprehensive morphological classification scheme for atherosclerotic lesions. Arterioscler Thromb Vasc Biol 20:1262–1275
29. Lohrke J, Frisk AL, Frenzel T, Schöckel L, Rosenbruch M, Jost G, Lenhard DC, Sieber MA, Nischwitz V, Küppers A, Pietsch H (2017) Histology and gadolinium distribution in the rodent brain after the administration of cumulative high doses of linear and macrocyclic gadolinium-based contrast agents. Investig Radiol 52:324–333
30. Scharlach C, Müller L, Wagner S, Kobayashi Y, Kratz H, Ebert M, Jakubowski N, Schellenberger E (2016) LA-ICP-MS allows quantitative microscopy of europium-doped Iron oxide nanoparticles and is a possible alternative to ambiguous Prussian blue iron staining. J Biomed Nanotechnol 12:1001–1010
31. Radbruch A, Richter H, Fingerhut S, Martin LF, Xia A, Henze N, Paulus W, Sperling M, Karst U, Jeibmann A (2019) Gadolinium deposition in the brain in a large animal model: comparison of linear and macrocyclic gadolinium-based contrast agents. Investig Radiol 54:531–536
32. Cotte M, Pouyet E, Salomé M, Rivard C, de Nolf W, Castillo-Michel H, Fabris T, Monico L, Janssens K, Wang T, Sciau P, Verger L, Cormier L, Dargaud O, Brun E, Bugnazet D, Fayard B, Hesse B, Pradas del Real AE, Veronesi G, Langlois J, Balcar N, Vandenberghe Y, Solé VA, Kieffer J, Barrett R, Cohen C, Cornu C, Baker R, Gagliardini E, Papillon E, Susini J (2017) The ID21 X-ray and infrared microscopy beamline at the ESRF: status and recent applications to artistic materials. J Anal At Spectrom 32:477–493
33. Wang S, Hesse B, Roman M, Stier D, Castillo-Michel H, Cotte M, Suuronen JP, Lagrange A, Radbruch H, Paul F, Taupitz M, Schellenberger E, Sack I, Infante-Duarte C (2019) Increased retention of gadolinium in the inflamed brain after repeated administration of gadopentetate dimeglumine: a proof-of-concept study in mice combining ICP-MS and micro– and nano–SR-XRF. Investig Radiol 54:617–626
34. Veronesi G, Deniaud A, Gallon T, Jouneau PH, Villanova J, Delangle P, Carrière M, Kieffer I, Charbonnier P, Mintz E, Michaud-Soret I (2016) Visualization, quantification and coordination of Ag+ ions released from silver nanoparticles in hepatocytes. Nanoscale 8:17012–17021
35. Katsuda S, Kaji T (2003) Atherosclerosis and extracellular matrix. J Atheroscler Thromb 10:267–274
36. Poller WC, Pieber M, Boehm-Sturm P, Ramberger E, Karampelas V, Möller K, Schleicher M, Wiekhorst F, Löwa N, Wagner S, Schnorr J, Taupitz M, Stangl K, Stangl V, Ludwig A (2018) Very small superparamagnetic iron oxide nanoparticles: long-term fate and metabolic processing in atherosclerotic mice. Nanomed Nanotechnol Biol Med 14:2575–2586
37. Poller WC, Ramberger E, Boehm-Sturm P, Mueller S, Möller K, Löwa N, Wiekhorst F, Wagner S, Taupitz M, Schellenberger E, Baumann G, Stangl K, Stangl V, Ludwig A (2016) Uptake of citrate-coated iron oxide nanoparticles into atherosclerotic lesions in mice occurs via accelerated transcytosis through plaque endothelial cells. Nano Res 9:3437–3452
38. O'Halloran TV, Culotta VC (2000) Metallochaperones, an intracellular shuttle service for metal ions. J Biol Chem 275:25057–25060
39. Briley-Saebo K, Bjørnerud A, Grant D et al (2004) Hepatic cellular distribution and degradation of iron oxide nanoparticles following single intravenous injection in rats: implications for magnetic resonance imaging. Cell Tissue Res 316:315–323
40. Kwon HM, Sangiorgi G, Ritman EL, McKenna C, Holmes DR Jr, Schwartz RS, Lerman A (1998) Enhanced coronary vasa vasorum neovascularization in experimental hypercholesterolemia. J Clin Invest 101:1551–1556
41. Meding J, Urich M, Licha K, Reinhardt M, Misselwitz B, Fayad ZA, Weinmann HJ (2007) Magnetic resonance imaging of atherosclerosis by targeting extracellular matrix deposition with Gadofluorine M. Contrast Media Mol Imaging 2:120–129
42. Wiener E, Settles M, Weirich G, Schmidt C, Diederichs G (2011) The influence of collagen network integrity on the accumulation of gadolinium-based MR contrast agents in articular cartilage. RöFo - Fortschritte Auf Dem Geb Röntgenstrahlen Bildgeb Verfahr 183:226–232
43. Karangelis ED, Kanakis IP, Asimakopoulou A et al (2010) Glycosaminoglycans as key molecules in atherosclerosis: the role of versican and hyaluronan
44. Uca YO, Taupitz M (2020) Glycosaminoglycans as novel targets for in vivo contrast-enhanced magnetic resonance imaging of atherosclerosis. J Cardiol Cardiovasc Med 5:9
45. Lindahl U, Hook M (1978) Glycosaminoglycans and their binding to biological macromolecules. Annu Rev Biochem 47:385–417
46. McDonald RJ, McDonald JS, Kallmes DF et al (2015) Intracranial gadolinium deposition after contrast-enhanced MR imaging. Radiology 275:772–782
47. Iimuro Y, Yamamoto M, Kohno H, Itakura J, Fujii H, Matsumoto Y (1994) Blockade of liver macrophages by gadolinium chloride reduces lethality in endotoxemic rats—analysis of mechanisms of lethality in endotoxemia. J Leukoc Biol 55:723–728
48. Weng T-I, Chen HJ, Lu C-W et al (2018) Exposure of macrophages to low-dose gadolinium-based contrast medium: impact on oxidative stress and cytokines production. Contrast Media Mol Imaging 2018:3535769
49. Reynolds JL, Joannides AJ, Skepper JN, McNair R, Schurgers LJ, Proudfoot D, Jahnen-Dechent W, Weissberg PL, Shanahan CM (2004) Human vascular smooth muscle cells undergo vesicle-mediated calcification in response to changes in extracellular calcium and phosphate concentrations: a potential mechanism for accelerated vascular calcification in ESRD. J Am Soc Nephrol 15:2857–2867
50. Proudfoot D, Shanahan CM (2001) Biology of calcification in vascular cells: intima versus media. Herz 26:245–251

8. Curriculum Vitae

For data protection reasons, the curriculum vitae was not published in the electronic version of my work.

For data protection reasons, the curriculum vitae was not published in the electronic version of my work.

9. Complete List of Publications

- Uca YO, Hallmann D, Hesse B, Seim C, Stolzenburg N, Pietsch H, Schnorr J, Taupitz M, Microdistribution of Magnetic Resonance Imaging Contrast Agents in Atherosclerotic Plaques Determined by LA-ICP-MS and SR-µXRF Imaging. Mol Imaging Biol, 2020
    - **Impact factor (2019): 3.270**
- Jacobi A, de Schellenberger AA, Uca YO, Herbik M, Guck J, Sack I, Real-Time Deformability Cytometry Detects Leukocyte Stiffening After Gadolinium-Based Contrast Agent Exposure, Investigative Radiology, 2021
    - **Impact factor (2018): 6.091**
- Schrank F, Warmuth C, Görner S, Meyer T, Tzschätzsch H, Guo J, Uca YO, Elgeti T, Braun J, Sack I, Real-time MR elastography for viscoelasticity quantification in skeletal muscle during dynamic exercises. Magn Reson Med, 2020
    - **Impact factor (2019): 3.635**
- Uca YO, Taupitz M, Glycosaminoglycans as Novel Targets for in vivo Contrast- Enhanced Magnetic Resonance Imaging of Atherosclerosis. J Cardiol Cardiovasc Med, 2020

10. Acknowledgments

I would like to express my gratitude to all people who have provided assistance during my dissertation study. First, I kindly thank my supervisor Prof. Matthias Taupitz for his support in pursuing this academic expedition at the Charité - Universitätsmedizin Berlin. I am thankful to Dr. Jörg Schnorr, my colleagues and the members of the Experimental Radiology Research Group for valuable discussions. I would like to express my special thanks to Dr. Antje Ludwig, who not only agreed to be my second supervisor, but also guided me well in constructing my dissertation.

I would like to acknowledge excellent cooperation with Bayer AG MR & CT Contrast Media Research, Berlin, the European Synchrotron Radiation Facility (ESRF), Zentrale Biomaterialbank der Charité (ZeBanC), Innovation in Radiology (InnoRa) and iPATH.Berlin – Core Unit Immunopathology for Experimental Models, Berlin, Germany. I am also grateful to David Hallmann, Dr. Hubertus Pietsch, Dr. Bernhard Hesse, Dr. Anja Kühl and Dr. Tobias Haase for the fruitful scientific interactions and their contribution to my research. I also appreciate the assistance of Rafet Güven for his graphical artwork.

This doctoral project would not have been possible if it were not for several key individuals. My deepest appreciation and thanks go to the Biophysical Quantitative Imaging Towards Clinical Diagnosis (BIOQIC) Graduate Program directors, Prof. Ingolf Sack and Prof. Tobias Schäffter for their availability, guidance and encouragement throughout this challenging but thriving scientific journey. I am grateful to them as they, by believing in me in the first place, continuously helped me push my own boundaries, from which I will benefit for the rest of my life. My deepest appreciation also goes to Dr. Judith Bergs, the coordinator of BIOQIC, who always offered her time for discussions.

Finally, I would like to express my warm appreciation to all the people who have been supportive throughout my time at the Charité and in Berlin.